NTNU

Norwegian University of
Science and Technology

Numerical Study of Mass Transfer Limitations in a Bioreactor Operated in the Heterogeneous Flow Regime

Ida Kristine Kure

Chemical Engineering and Biotechnology
Submission date: June 2017
Supervisor: Hugo Atle Jakobsen, IKP
Co-supervisor: Jannike Solsvik, IKP

Norwegian University of Science and Technology
Department of Chemical Engineering

Abstract

With the increased focus on detaining a more environmental friendly industry, biological processes have been given more attention over the last years. Such a biological process is single cell protein (SCP) production, which can use bacteria to utilize methane or methanol in the production of protein.

In SCP production, the methanotroph bacteria *Methylococcus capsulatus*, with its high protein content of approximately 70%, is a well suited bacteria for the process. With the bacteria being an aerobic bacteria, the mass transfer of oxygen to the cells is crucial. Methanotroph bacteria utilize single-carbon compounds, typically methane, as their sole carbon and energy source. It is therefore necessary with sufficient mass transfer of methane and oxygen in order to obtain a large bio-protein production.

Previous literature have stated that the SCP process is limited by mass transfer. The objectives of this work were to model SCP process operated in a vertical three phase (slurry) bubble column reactor. Emphasis was placed on evaluating the mass transfer limitations and the sensitivity to choice of correlation for the mass transfer coefficient. Additionally, a model of a single bubble rising in a tube was derived. The purpose was to obtain a model that can be used as a basis for choosing the best mass transfer coefficients for SCP production based on experimental data.

The reactor simulation results showed that with an average bubble diameter of 2 mm and with an initial biomass fraction of 3 wt%, the bio-protein production was limited by mass transfer. Reducing the diameter with a factor of 5, resulted in the process being limited by the kinetics. It was found that the mass transferred was affected by the choice of mass transfer coefficient.

In order to provide precise representations of the bio-protein production in SCP production, it should be prioritized to find an accurate correlation for the mass transfer coefficient. Design of bio-reactors should have the aim of keeping the bubble size low in the reactor, as this will result in a higher mass transfer.

Sammendrag

Med et stadig økende fokus på en mer miljøvennlig industri, gis biologiske prosesser stadig mer og mer oppmerksomhet. En slik biologisk prosess er encellet protein (SCP) produksjon, der man kan bruke bakterier til å nyttegjøre seg av metan eller metanol.

I SCP produksjon er den metanotrofe bakterien *Methylococcus capsulatus*, med dens høye proteininnhold på omlag 70%, en vellegnet bakterie. Bakterien er en aerob bakterie, og massoverføring av oksygen til cellen er dermed kritisk. Metanotrofe bakterier benytter seg av enkelt-karbon komponenter, typisk metan, som deres eneste karbon- og energikilde. Det er derfor nødvendig med tilstrekkelig masseoverføring av metan og oksygen, for å oppnå en stor proteinproduksjon.

I litteraturen har det blitt hevdet at SCP prosessen er begrenset av masseoverføring. I denne oppgaven er det blitt laget en modell for SCP produksjon operert i en vertikal trefase boblekolonnereaktor. Det ble lagt vekt på evaluering av masseoverføringsbegrensninger og sensitivitet til valg av masseoverføringskoeffisient. I tillegg ble en modell for en enkelt boble stigende i en kolonne utledet. Hensikten med dette var å kunne lage en modell som kan brukes som basis når den mest nøyaktige masseoverføringskoeffisienten i SCP produksjon skal bestemmes ved hjelp av eksperimentelle data.

Resultatene fra reaktorsimuleringene viste at med en gjennomsnitlig boblestørrelse på 2 mm, og en initiell massefraksjon av biomasse på 3 vektprosent, var biomasseproduksjonen begrenset av masseoverføringen. Ved å redusere boblestørrelsen med en faktor på fem, ble prosessen kinetikkbegrenset. Det ble funnet at masseoverføring var sterkt påvirket av valg av masseoverføringskoeffisient.

For å kunne gi presise representasjoner av biomasseproduksjonen i SCP produksjon, bør det prioriteres å finne en nøyaktig korrelasjon for masseoverføringskoeffisienten. Design av bioreaktoren bør ha som formål å holde boblestørrelsen nede i reaktoren, ettersom dette vil resultere i en høyere masseoverføring.

This Master's thesis was written in the spring of 2017. It concludes the 5 year Master's program in Chemical Engineering and Biotechnology at the Norwegian University of Science and Technology, leading to the degree of M.Sc. in Chemical Engineering. My final year at NTNU was spent as a part of the research group in Environmental Engineering and Reactor Technology within the Department of Chemical Engineering. The work performed in this thesis is a continuation of the specialization project carried out in the fall of 2016.

I would like to thank my supervisor, Professor Hugo Jakobsen for your suport throughout this last year. Your knowledge, enthusiasm and humor has truly been an inspiration when writing my master thesis.

A special thanks to Mathias for support and proofreading my master thesis. In addition I would like to thank my greatest friend, Cathrine, for being a good friend, also in times when I wanted to destroy MATLAB.

Declaration of Compliance

I declare that this is an independent work according to the exam regulations of the Norwegian University of Science and Technology (NTNU).

Trondheim, June 19, 2017

Ida Kristine Kure

Contents

Abstract i

Sammendrag iii

Table of Contents vii

List of Figures ix

1 Introduction 1

2 Theory 5
2.1 Transport Mechanism 5
2.1.1 Mass Transfer Models 9
2.1.2 Mass Transfer Coefficient 14
2.2 Kinetics 21

3 Mathematical Model 25
3.1 Pressure and Velocity 27
3.2 Species Mass Balances 29
3.3 Temperature Equations 33
3.4 Boundary Conditions 35
3.5 Solution Method 36
3.5.1 Implementation 41

4 Results Single Cell Protein 43
4.1 Optimization of the inlet values 49
4.1.1 Inlet Values of Methane and Oxygen 49
4.1.2 Superficial Gas Velocity 53
4.1.3 Superficial Liquid Velocity 57
4.1.4 Inlet Values Biomass 61
4.1.5 Reduced Bubble Size 65
4.2 Mass Transfer Coefficient 69
4.3 Conclusion SCP 82

5 Modeling of a Single Bubble 83

5.1 Mathematical Model . . . 85
5.1.1 Pressure . . . 86
5.1.2 Total Mass . . . 87
5.1.3 Species Mass Balance . . . 88
5.1.4 Momentum Balance . . . 89
5.1.5 Bubble Diameter . . . 90
5.1.6 Implementation . . . 90

6 Results Single Bubble 93
6.1 Oxygen and Nitrogen . . . 96
6.1.1 Constant and Varying Volume . . . 102
6.2 Methane and Nitrogen . . . 106
6.3 Carbon dioxide and Nitrogen . . . 107
6.4 Nitrogen Bubble in Carbon dioxide Saturated Water . . . 108
6.5 Various Mass Transfer Coefficients . . . 113
6.6 Conclusion Single Bubble . . . 120

7 Suggested Improvements 121

A Appendix 127
A.1 Contact Time and Turbulent Dissipation Energy . . . 127
A.2 SCP Production . . . 132
A.3 Additional Figures Single Bubble . . . 136
A.4 Henry's Law on Mass Basis . . . 165
A.5 Mass Flux . . . 167
A.6 Constants SCP . . . 169
A.7 Constants Single Bubble . . . 171
A.8 Leibniz Rule and Gauss Theorem for a Volume Integral . . . 173
A.9 Modeling Equations Single Bubble . . . 173
A.9.1 Total Mass . . . 173
A.9.2 Species Mass Balance . . . 176
A.9.3 Momentum Balance . . . 177
A.9.4 Bubble Diameter . . . 179

List of Figures

1.0.1 Process diagram for the BioProtein process located at Tjeldbergodden, Norway. The diagram includes all steps from the reactor to the final protein is taken from Arild Johannessen [1].. 3

2.1.1 Vertical bubble column containing bacteria and salt and mineral containing water. The methane and oxygen gas is fed in the bottom of the column, and divided into bubbles by a sparger. Ammonia is introduced in a liquid stream in the bottom. The biomass, carbon dioxide and water produced is taken out in the top. Note that the bacteria is much smaller than indicated in the figure. 6

2.1.2 Specific oxygen uptake rate as a function of the dissolved oxygen concentration. Above the critical oxygen concentration the cell function optimally, and below the specific value the cell is limited by the oxygen concentration. The figure is taken from Doran [12]. 8

2.1.3 Oxygen transfer from a gas bubble to a cell. All the steps from the gas bubble to the bacteria is shown. The steps all contribute with a resistance in the mass transfer. An individual cell and a cell clump is shown to illustrate possibility of different cells. The figure is taken from Doran [12]. . . . 9

2.1.4 Two-film theory, where the pressure stays constant on the gas side, drops over the gas film, the concentration over the liquid film decrease, and the concentration in the liquid is constant due to the assumption of perfect mix. The figure is based on the figure in the book by Jakobsen [22]. 11

2.1.5 Principle of surface renewal, where an element in the bulk transport to near the gas-liquid interface. Mass transfer takes place, and the element transport out in the well mixed region. The figure is based on the figure in the book by Jakobsen [22]. 13

2.1.6 Steady drag coefficient and terminal velocity varying with the bubble diameter for clean, partly contaminated, and contaminated systems. 17

2.1.7 Mass transfer coefficient as a function of bubble size for clean systems. Mass transfer coefficients are shown with lines and experimental measurements are shown with points. 18
2.1.8 Mass transfer coefficient as a function of bubble size for partly contaminated and contaminated systems. Lines indicate models and points indicate measurements. 19
2.2.1 Change in cell concentration in a batch culture as a function of time. Cell growth stages are shown in the figure, which are taken from Doran [12]. 21

4.0.1 Change in gas densities for methane, oxygen, and carbon dioxide over the reactor length with the initial values based on the values by Taweel et al. [42] and Larsen [24]. 43
4.0.2 Change in liquid density of the components over the reactor length with the initial values based on the values by Taweel et al. [42] and Larsen [24]. 44
4.0.3 Reaction rate of biomass with the initial values based on the values by Taweel et al. [42] and Larsen [24]. 46
4.0.4 Gas pressure and velocity along the reactor length with the initial values based on the values by Taweel et al. [42] and Larsen [24]. 47
4.0.5 Temperature of the gas- and liquid phase in the reactor with the initial values based on the values by Taweel et al. [42] and Larsen [24]. 48
4.1.1 Gas densities for methane, oxygen and carbon dioxide with varying inlet methane fractions, $w_{CH_4} = 0.07$, $w_{CH_4} = 0.23$, $w_{CH_4} = 0.30$ 49
4.1.2 Component liquid densities with varying inlet methane fractions, $w_{CH_4} = 0.07$, $w_{CH_4} = 0.23$, $w_{CH_4} = 0.30$. 50
4.1.3 Reaction rate of biomass with varying inlet methane fractions, $w_{CH_4} = 0.07$, $w_{CH_4} = 0.23$, $w_{CH_4} = 0.30$. 51
4.1.4 Component gas densities with varying superficial gas velocity, $v_g = 0.04$, $v_g = 0.07$, $v_g = 0.1$.. 53
4.1.5 Component liquid density with varying superficial gas velocity, $v_g = 0.04$, $v_g = 0.07$, $v_g = 0.1$. 54
4.1.6 Reaction rate of biomass with varying superficial gas velocity, $v_g = 0.04$, $v_g = 0.07$, $v_g = 0.1$.. 55
4.1.7 Component gas densities over the tube with varying liquid velocity, $v_l = 0.4$, $v_l = 0.6$, $v_l = 0.7$ 57

4.1.8 Component liquid densities with varying liquid velocity, v_l = 0.4, v_l = 0.6, v_l = 0.7 58
4.1.9 Reaction rate of biomass with varying liquid velocity, v_l = 0.4, v_l = 0.6, v_l = 0.7 59
4.1.10 Component gas densities with various inlet biomass, w_X = 0.02, w_X = 0.04, w_X = 0.1 61
4.1.11 Liquid component densities with various inlet biomass, w_X = 0.02, w_X = 0.04, w_X = 0.1 62
4.1.12 Reaction rate of biomass with various inlet biomass, w_X = 0.02, w_X = 0.04, w_X = 0.1 63
4.1.13 Component gas densities with different average bubble diameter, $d_b = 2$, $d_b = 2/5$, $d_b = 2\dot{5}$. 65
4.1.14 Change in liquid densities with different average bubble diameter, $d_b = 2$, $d_b = 2/5$, $d_b = 2\dot{5}$ 66
4.1.15 Change in reaction rate of biomass with different average bubble diameter, $d_b = 2$, $d_b = 2/5$, $d_b = 2\dot{5}$ 67
4.2.1 Gas density for the components for a clean system with use of different mass transfer coefficients. 69
4.2.2 Liquid density of the components for a clean system with use of different mass transfer coefficients. 70
4.2.3 Reaction rate of biomass for a clean system with use of different mass transfer coefficients. 71
4.2.4 Component gas densities in gas phase for a partly contaminated system with use of different mass transfer coefficients. 73
4.2.5 Liquid component densities for a partly contaminated system with use of different mass transfer coefficients. 74
4.2.6 Reaction rate of biomass for a partly contaminated system with use of different mass transfer coefficients. 75
4.2.7 Component gas densities with different correlations for the mass transfer coefficient for a contaminated system. 76
4.2.8 Component liquid densities with different correlations for the mass transfer coefficient for a contaminated system. 77
4.2.9 Reaction rate of biomass with use of different mass transfer coefficients for a contaminated system.. 78

5.0.1 Single gas bubble rising in a vertical tube containing water. The water types used will vary from being clean, partly contaminated and contaminated 84

6.0.1 Oxygen and nitrogen gas densities with use of the correct and incorrect bubble area. The profiles with the correct bubble area are denoted as CH_4,system,new, where system = clean, partly contaminated and contaminated. The profiles with the incorrect bubble area are denoted as CH_4,system,old, where system = clean, partly contaminated and contaminated. . . 94
6.0.2 Bubble diameter and terminal velocities with use of correct and incorrect bubble area. The profiles with the correct bubble area are denoted as clean,new, partly contaminated,new and contaminated,new. The profiles with the incorrect bubble area are denoted as clean,old, partly contaminated,old and contaminated,old.. 95
6.1.1 Change in gas velocity and bubble size over the tube for a bubble containing initially 21% oxygen and 79% nitrogen.. . 96
6.1.2 Component gas densities for a bubble containing initially 21% oxygen and 79% nitrogen. 98
6.1.3 Mass transfer coefficients for a bubble containing initially 21% oxygen and 79% nitrogen. 100
6.1.4 Mass transfer coefficients with use of the correlation by Brauer [7].. 101
6.1.5 Component gas densities for a bubble containing initially 21% oxygen and 79% nitrogen, for both constant and varying bubble volume.. 103
6.1.6 Bubble velocity and diameter for a bubble containing initially 21% oxygen and 79% nitrogen, for both constant and varying bubble volume. 104
6.1.7 Mass transfer coefficients for a bubble containing initially 21% oxygen and 79% nitrogen, for both constant and varying bubble volume.. 105
6.4.1 Component gas densities for a bubble containing initially 100% nitrogen rising in a tube with carbon saturated water. . 109
6.4.2 Component gas densities for a bubble containing initially 100% nitrogen rising in a tube with carbon saturated water. . 110

6.4.3 Bubble diameter and velocity profiles for a bubble containing initially 100% nitrogen rising in a tube with carbon saturated water. 111
6.4.4 Mass transfer coefficients for carbon dioxide and nitrogen initially 100% nitrogen rising in a tube with carbon saturated water. 112
6.5.1 Mass transfer coefficients for oxygen and nitrogen for a clean system. 114
6.5.2 Mass transfer coefficients for oxygen and nitrogen for a partly contaminated system. 116
6.5.3 Mass transfer coefficients for oxygen and nitrogen for a contaminated system. 118

A.2.1 Mass fractions of the components in gas phase with the initial values based on the values by Taweel et al. [42] and Larsen [24]. 132
A.2.2 Mass fractions of the components in liquid phase with the initial values based on the values by Taweel et al. [42] and Larsen [24]. 133
A.2.3 Change in gas density of the components with varying mass transfer coefficient for turbulent flow. 134
A.2.4 Change in liquid density of the components with varying mass transfer coefficient for turbulent flow 135
A.2.5 Reaction rate of biomass with varying mass transfer coefficient for turbulent flow 136
A.3.1 Mass fractions for a bubble containing initially 21% oxygen and 79% nitrogen, for constant and varing volume. 137
A.3.2 Pressure and volume change over the column for a bubble containing initially 21% oxygen and 79% nitrogen, for constant and varing volume.. 138
A.3.3 Component densities in gas phase with use of correlation by Brauer [7] for the mass transfer coefficient. The same coefficient is used on all the systems. 139
A.3.4 Component gas densities for a bubble containing initially 40% methane and 60% nitrogen for varying water systems. . . . 140
A.3.5 Mass fractions for a bubble containing initially 40% methane and 60% nitrogen for varying water systems. 141

A.3.6 Change in the bubble diameter and velocity for a bubble containing initially 40% methane and 60% nitrogen for varying water systems. 142
A.3.7 Change in bubble volume and gas pressure over the column for a bubble containing initially 40% methane and 60% nitrogen for varying water systems.. 143
A.3.8 Mass fractions for a bubble containing initially 10% carbon dioxide and 90% nitrogen for varying water systems.. 144
A.3.9 Component gas densities for a bubble containing initially 10% carbon dioxide and 90% nitrogen for varying water systems. . 145
A.3.10 Mass fractions for a bubble containing initially 10% carbon dioxide and 90% nitrogen for varying water systems.. 146
A.3.11 Mass fractions for a bubble containing initially 10% carbon dioxide and 90% nitrogen for varying water systems.. 147
A.3.12 Mass fractions in gas phase with use of the same mass transfer coefficient for all systems. 148
A.3.13 Change in volume and pressure with use of the same mass transfer coefficient for all systems. 149
A.3.14 Velocity and bubble diameter with use of the same mass transfer coefficient for all systems. 150
A.3.15 Mass transfer coefficient for oxygen and nitrogen with use of the same mass transfer coefficient for all systems.. 151
A.3.16 Mass fractions in the gas phase for bubble containing initially 100% nitrogen, rising a carbon dixoxide saturated water. . . 152
A.3.17 Pressure and volume profiles for bubble containing initially 100% nitrogen, rising a carbon dixoxide saturated water. . . 153
A.3.18 Mass fractions of the gas phase with use of different mass transfer coefficients for a clean system.. 154
A.3.19 Component gas density with use of different mass transfer coefficients for a clean system.. 155
A.3.20 Change in velocity in bubble size with use of different mass transfer coefficients for a clean system.. 156
A.3.21 Volume and pressure profiles with use of different mass transfer coefficients for a clean system. 157
A.3.22 Mass fractions of the gas phase with use of different mass transfer coefficients for a partly contaminated system. . . . 158
A.3.23 Component gas density with use of different mass transfer coefficients for a partly contaminated system. 159

A.3.24 Change in velocity in bubble size with use of different mass transfer coefficients for a partly contaminated system. . . . 160
A.3.25 Volume and pressure profiles with use of different mass transfer coefficients for a partly contaminated system. 161
A.3.26 Mass fractions of the gas phase with use of different mass transfer coefficients for a contaminated system. 162
A.3.27 Component gas density with use of different mass transfer coefficients for a contaminated system.. 163
A.3.28 Change in velocity in bubble size with use of different mass transfer coefficients for a contaminated system. 164
A.3.29 Volume and pressure profiles with use of different mass transfer coefficients for a contaminated system. 165

Notation List

Latin Symbol	Unit	Description
a	$m^2\ m^{-3}$	Gas-liquid contact area
$c_{p,i,G}$	$J\ K^{-1}\ kg^{-1}$	Specific heat capacity of component i in gas phase
$c_{p,i,L}$	$J\ K^{-1}\ kg^{-1}$	Specific heat capacity of component i in liquid phase
C_D	-	Drag coefficient
$C_{p,G}$	$J\ K^{-1}\ kg^{-1}$	Gas heat capacity
$C_{p,L}$	$J\ K^{-1}\ kg^{-1}$	Liquid heat capacity
$C^*_{i,L}$	$mol\ m^{-3}$	Equilibrium concentration of component i in the liquid phase
$C_{i,L}$	$mol\ m^{-3}$	Concentration of component i in the liquid phase
C_{crit}	$mol\ m^{-3}$	Critical oxygen concentration
C_P	$mol\ m^{-3}$	Product concentration
C_S	$mol\ m^{-3}$	Limiting substrate concentration
C_{Se}	$mol\ m^{-3}$	Concentration of growth-enhancing substrate
C_X	$mol\ m^{-3}$	Biomass concentration
d_b	m	Bubble diameter
d_c	m	Column diameter
$d_{b,in}$	m	Inlet bubble diameter
d_{b0}	m	Smallest diameter of the larger bubbles
d_c	m	Column diameter
d_{vs}	m	Sauter mean diameter of a gas bubble
D	s^{-1}	Dilution rate
$D^{eff}_{z,G}$	$m^2\ s^{-1}$	Effective axial dispersion coefficient in gas phase
$D^{eff}_{z,L}$	$m^2\ s^{-1}$	Effective axial dispersion coefficient in liquid phase
D_L	$m^2\ s^{-2}$	Diffusion coefficient in continuous phase
E_o	-	Eötvös number
f	-	Darcy friction factor
F_B	N	Buoyancy force
F_D	N	Drag force

Latin Symbol	Unit	Description
g	m s^{-2}	Acceleration due to gravity
h_{cool}	W m^{-2} K^{-1}	Heat transfer coefficient cooling medium
h_L	W m^{-2} K^{-1}	Heat transfer coefficient liquid
ΔH_{rx}	J $mol_{O_2}^{-1}$	Heat of reaction
k_d	s^{-1}	Specific cell death constant
k_L	m s^{-1}	Mass transfer coefficient
$k_{\bar{L}}$	m s^{-1}	Mass transfer coefficient
k_L^{eff}	W m^{-1} s^{-1}	Effective thermal conductivity in liquid phase
k_G^{eff}	W m^{-1} s^{-1}	Effective thermal conductivity in gas phase
k_{steel}	W m^{-1} s^{-1}	Thermal conductivity of the wall material
K_I	mol m^{-3}	Inhibition constant
K_O	mol m^{-3}	Oxygen constant
K_S	mol m^{-3}	Substrate constant
K_{CH4}	mol m^{-3}	Methane constant
$K_{S,1}$	mol m^{-3}	Methanol affinity constant
$K_{S,2}$	mol m^{-3}	Oxygen affinity constant
l_G	m	Thickness of gas film
l_L	m	Thickness of liquid film
m_i	kg	Mass of component i
m_S	s^{-1}	Maintenance coefficient
$\bar{M}$	kg mol^{-1}	Average molar mass
M_i	kg mol^{-1}	Molar mass of component i
M_X	kg mol^{-1}	Molar mass of biomass
n_i	mol	Moles of component i
N_i	mol s^{-1} m^{-3}	Mass flux
N_{Sc}	$-$	Schmidt number
$p_{i,G}$	Pa	Partial pressure in gas phase
p_T	Pa	Total pressure
$p_{l,out}$	Pa	Outlet liquid pressure
q_p	s^{-1}	Specific rate of product formation
q_r	s^{-1}	Specific rate of substrate uptake
r_d	h^{-1}	Cell death rate
r_S	mol $s^{-1}m^{-3}$	Volumetric rate of substrate uptake
r_X	mol $s^{-1}m^{-3}$	Volumetric rate of biomass production
R	m^3Pa $K^{-1}mol^{-1}$	Universal gas constant
R_i	kg $s^{-1}m^{-3}$	Reaction rate of component i

Latin Symbol	Unit	Description
Re	$-$	Reynolds number
Re_b	$-$	Bubble Reynolds number
t_w	m	Thickness of the wall
T_G	K	Temperature in gas phase
$T_{in,G}$	K	Inlet temperature in gas phase
T_L	K	Temperature in liquid phase
$T_{in,L}$	K	Inlet temperature in liquid phase
T_w	K	Temperature cooling medium
U	W m^{-2} K^{-1}	Overall heat transfer coefficient
$v^S_{in,G}$	m^3 m^{-3} s^{-1}	Inlet superficial gas velocity
$v^S_{in,L}$	m^3 m^{-3} s^{-1}	Inlet superficial liquid velocity
v^S_G	m^3 m^{-3} s^{-1}	Superficial gas velocity
v^S_L	m^3 m^{-3} s^{-1}	Superficial liquid velocity
v_s	m s^{-1}	Bubble-liquid relative velocity
v_t	m s^{-1}	Terminal velocity
$\underline{v}_I$	msˆ-1	Velocity at the interface
$\underline{v}_I$	msˆ-1	Bubble velocity
V	m^3	Volume
V_l	m^3	Liquid volume
$V_{g,in}$	m^3	Inlet volume gas
w_in	msˆ-1	Inlet gas velocity
w_g	msˆ-1	gas velocity
w_l	msˆ-1	Liquid velocity
w_r	msˆ-1	Relative gas velocity
$y_{i,G}$	mol_i mol^{-1}_{tot}	Mole fraction in gas phase
Y_{iX}	$mol_i mol^{-1}_X$	Theoretical yield coefficient of component i per biomass
Y_{PS}	$mol_P mol^{-1}_S$	Theoretical yield of product per substrate
Y_{XS}	$mol_X mol^{-1}_S$	Theoretical yield of biomass per substrate

Greek Symbol	Unit	Description
ε_G	$-$	Gas hold-up
ε_L	$-$	Liquid hold-up
λ_L	W m^{-1} K^{-1}	Thermal conductivity of water
μ	s^{-1}	Specific growth rate
μ_c	Pa s	Continuous phase viscosity
μ_{max}	s^{-1}	Maximum specific growth rate
μ_S	s^{-1}	Specific growth rate of methanol
μ_O	s^{-1}	Specific growth rate of oxygen
$w_{i,G}$	kg$_i$ kg$_{tot}^{-1}$	Mass fraction of component i in gas phase
$w_{i,L}$	kg$_i$ kg$_{tot}^{-1}$	Mass fraction of component i in liquid phase
$w_{X,L}$	kg$_X$ kg$_{tot}^{-1}$	Mass fraction of biomass in liquid phase
τ	s	Residence time
ρ_b	kg m^{-3}	Bubble density
ρ_d	kg m^{-3}	Density dispersed phase
ρ_G	kg m^{-3}	Density in the gas phase
$\rho_{in,G}$	kg m^{-3}	Inlet density in the gas phase
ρ_L	kg m^{-3}	Density in the liquid phase
$\rho_{in,L}$	kg m^{-3}	Inlet density in the liquid phase
$\rho_{i,L}$	kg m^{-3}	Density of component i in the liquid phase
$\rho_{i,L}^*$	kg m^{-3}	Equilibrium density of component i in the liquid phase
$\Delta\rho$	kg m^{-3}	Difference between the liquid- and gaseous phase densities
σ	Nm	Surface tension

Chapter 1

Introduction

With the increase in human population, the food and resource demands in the world increases, which again is a large contributing factor to environmental degradation. Examples of such degradation is the removal of rainforest for use for agricultural purposes and overfishing.

In 2015 it was estimated that 143 billion cubic meters of natural gas was flared globally [2]. The burning of natural gas at oil production sites, is approximated to annually emit 350 million tons of CO_2 to the atmosphere [2]. The burning of fossil fuels is a very large contributor to global warming. Finding ways to utilize some of this natural gas would be beneficial.

In some cases, an alternative to flaring natural gas is biological conversion with use of methanotroph bacteria. Methanotrophs are bacteria which can utilize single-carbon as their carbon and energy source under aerobic conditions. Aerobic conditions means environments with access to oxygen. Such a bacteria, in the group of methanotroph bacteria, is *Methylococcus capsulatus*. With methane being the main component in natural gas, this is a more harmless way of converting the natural gas.

A bio-process where bacteria is used in the conversion of methane, is in single cell protein (SCP) production. In SCP production methanotroph bacteria can be used to utilize methane to produce bio-protein. Methanotroph bacteria are well suited for SCP production with its high protein content of 70%. Under growth conditions the bacteria, referred to as cells, will start to replicate, resulting in an increase in the cell volume and in the end a cell division. The bacteria experience the fastest growth at optimal growth conditions. Optimal growth conditions means an environment with optimal temperature, pH, and with unlimited access to nutrients. The cell division process can be divided into different stages. First, a growth stage where the volume is doubled, then the cell reach an intermediate stage where the cell functions are replicated, before the cell finally is divided into two identical daughter cells. The process where a cell divides into new cells is called cell growth, and the division is better known as binary fission [11].

Due to too high amino acid contents and limiting EU-regulations, the bio-protein is not approved for use in food for human beings. With increased interest in the bio-process, it is hope that the development of the process will lead to development of bacterial strains suitable for human consumption.

With its high protein content, SCP can serve as a good alternative to soy protein and fish meal for use in animal feeds, for aquaculture and livestock. This will lead to less strain on the environment, in addition to resulting in less waste of natural gas. Companies that have been working on this specific process are Norferm, now owned by Calysta, and Unibio. Unibio is a company collaborating with the Technical University of Denmark (DTU) and The University of Trinidad and Tobago. At both universities pilot plants are installed, and both universities have published papers on the modeling of the process. In the Unibio pilot plant, a patented U-loop reactor is used. Static mixers are placed in the vertical legs of the reactor to increase the gas-liquid mass transfer. The U-loop is equipped with heat exchangers for heat removal of the heat produced in the process. In 2016, Unibio opened its commercial plant.

Norferm operated the first industrialized plant of its kind for production of SCP at Tjeldbergodden in Norway. The process plant at Tjeldbergodden is illustrated in Figure 1.0.1 to show an example of a plant used for SCP production.

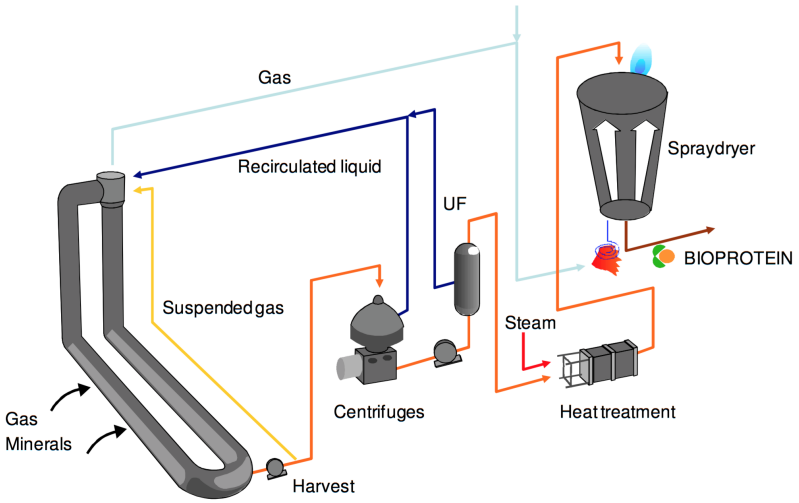

Figure 1.0.1: Process diagram for the BioProtein process located at Tjeldbergodden, Norway. The diagram includes all steps from the reactor to the final protein is taken from Arild Johannessen [1].

Bacteria, referred to as biomass, and water from the reactor is sent to a centrifuge, where the biomass concentration is increased, Figure 1.0.1. The salt and mineral containing water, known as fermentation broth, is recycled back to the reactor and the biomass is sent to ultra filtration. Here the biomass concentration is further increased. The biomass is sent to heat treatment before the last step where it is dried to powder. In the Norferm process the reactor was constructed with both a vertical and a horizontal part. To enhance the mass transfer static mixers were placed inside the tube. The methane and oxygen were introduced several places along the reactor, in order to avoid critical methane-oxygen ratios, which could potentially result in explosions.

In the current literature it is stated that SCP production is limited by mass transfer. There are only a few sources that have modeled the process with use of a U-loop reactor, Olsen et al. [29], Wu et al. [47], Prado-Rubio et al. [30] and Taweel et al. [42], and it is therefore of interest to derive a model that evaluates the validity of the stated mass transfer limitations. In this work a U-loop reactor will be modeled for SCP production, where it is assumed that modeling only one leg of the reactor is sufficient. The objectives of the work is to model

SCP production with a focus on investigating the mass transfer limitations, and sensitivities in the choice of mass transfer coefficient. Additionally, optimal operating parameters will be evaluated. It is of interest to derive a model for a single bubble rising in a column, to investigate the mass transfer on a smaller scale. The model of a single bubble can be used as a basis for improving the mass transfer representation in SCP production. Based on the findings from the reactor simulations, recommendations for further improvements will be given.

Chapter 2

Theory

In this chapter transport mechanisms for mass transfer and the kinetics used in SCP production will be presented.

2.1 Transport Mechanism

Aerobic cells are organisms that depend on oxygen in order to survive and grow. The rate of oxygen consumption by the bacteria determined how fast the oxygen needs to be transferred to the cells. The mass flux is therefore of great importance both for the production of biomass and for the existence of the cells.

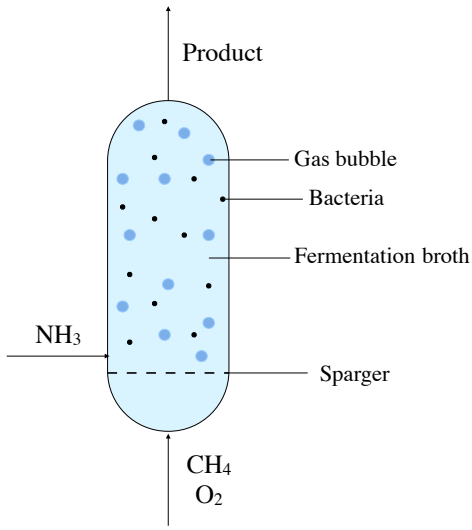

Figure 2.1.1: Vertical bubble column containing bacteria and salt and mineral containing water. The methane and oxygen gas is fed in the bottom of the column, and divided into bubbles by a sparger. Ammonia is introduced in a liquid stream in the bottom. The biomass, carbon dioxide and water produced is taken out in the top. Note that the bacteria is much smaller than indicated in the figure.

The reactor is modeled as a three-phase (slurry) vertical bubble column and is shown in Figure 2.1.1. Initially the column contains bacteria and a fermentation broth. The fermentation broth (liquid solution) consist of water and a salt-mineral solution, where the salt and minerals are added to facilitate the bacterial growth. The bacteria occupies $2-3\%$ of the reactor volume. In SCP production possible reactants are pure methane ($\geqslant 99\%$), purified or oxygen-enriched air and liquid ammonia. In the bottom of the reactor, methane and oxygen gas is inserted as bubbles by a sparger. Depending on desired initial bubble size, the sparger can be adjusted. Ammonia is inserted in the bottom as a liquid stream and is assumed to stay in liquid phase throughout the column. The gas dissolves

in the liquid phase (fermentation broth) and the molecules are transported into the bacteria through the cell walls, where they are utilized by the bacteria. The reactor is operated continuously and the biomass, carbon dioxide and water, is taken out in the top of the column. It should be noted that the bacteria are much smaller than what the figure indicates.

In this work the stoichiometric reaction from the study of Taweel et al. [42] is used:

$$CH_4 + 0.104NH_3 + 1.45O_2 \rightarrow 0.52CH_{1.8}O_{0.6}N_{0.2} + 0.48CO_2 + 1.69H_2O \quad (2.1.1)$$

Bacteria Oxygen Demand

In order to provide optimal growth conditions for the cells the oxygen concentration in the solution must be over a critical concentration, C_{crit}. The oxygen available for the cells depends on the solubility of oxygen in the solution, which dependens on the pressure and the temperature. At ambient pressure and temperature the solubility of oxygen in water is < 10 ppm. In other words, the cells consume the oxygen very fast and the oxygen needs to be introduced continuously.

The specific oxygen uptake rate is the rate of oxygen consumption per cell [12]. In Figure 2.1.2 the specific oxygen uptake rate is shown as a function of the dissolved oxygen concentration in the liquid.

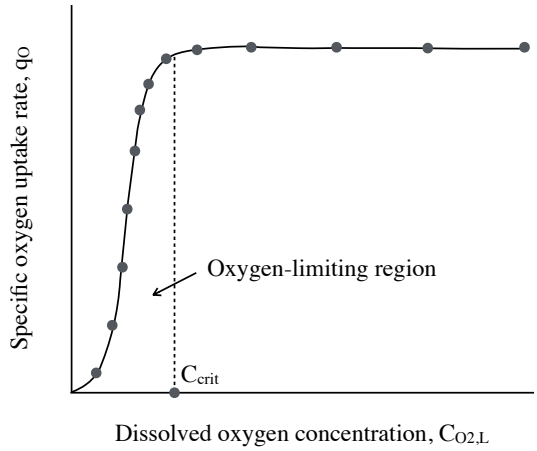

Figure 2.1.2: Specific oxygen uptake rate as a function of the dissolved oxygen concentration. Above the critical oxygen concentration the cell function optimally, and below the specific value the cell is limited by the oxygen concentration. The figure is taken from Doran [12].

From Figure 2.1.2 it can be seen that when the dissolved oxygen in the liquid is higher than the critical oxygen concentration, C_{crit}, the oxygen uptake rate for a cell is at a constant maximum. This means that the cell metabolism is optimal. Below this critical concentration, the specific oxygen uptake rate is close to linearly dependent on the dissolved oxygen concentration. A reduced specific oxygen uptake can result in the bacteria either going into sleep, producing undesired products, or ultimately dying. The numerical value of the critical oxygen concentration depends on the organism. There are several factors that can affect the oxygen demand. The most important ones are cell species, growth phase of the culture, and the carbon source (substrate) present [12].

2.1.1 Mass Transfer Models

When modeling gas-liquid mass transfer, choosing a suitable correlation for the mass transfer coefficient can be very challenging. The mass transfer coefficient expresses how fast a component is moving over an interphase. Figure 2.1.3 shows the transport mechanism of a compound from a gas bubble to a cell.

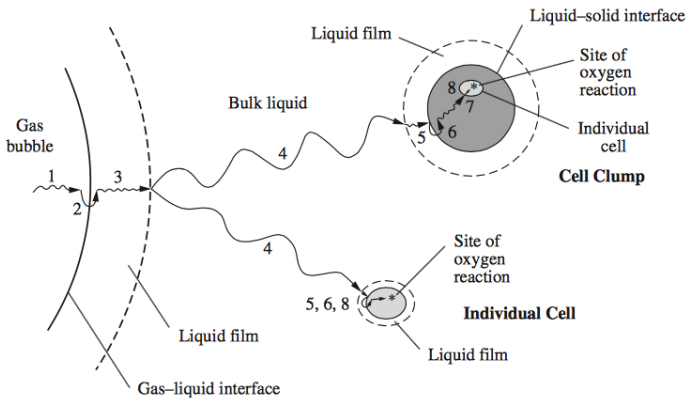

Figure 2.1.3: Oxygen transfer from a gas bubble to a cell. All the steps from the gas bubble to the bacteria is shown. The steps all contribute with a resistance in the mass transfer. An individual cell and a cell clump is shown to illustrate possibility of different cells. The figure is taken from Doran [12].

In Figure 2.1.3 a stagnant liquid film surrounds the gas bubble and the cell. On the gas side of the gas-liquid interface there exists a gas film. This film is not included in Figure 2.1.3 as the diffusion and thus mixing in the gas phase is usually much faster than in the liquid, resulting in the gas inside the bubble being perfectly mixed and the thickness of the gas film, l_G, approaches zero, $l_G \to 0$.

In the transport of an oxygen molecule all steps marked $(1-8)$ in Figure 2.1.3 will represent a resistance. As described above the diffusion over the gas film, (step 1) in Figure 2.1.3, is neglected as the diffusion and thus mixing is much faster than in liquid. The transport over the gas-liquid interface (step 2) is negligible due to the interphase being much thinner than the liquid film. If

the solution is assumed to be well mixed the concentration gradients in the liquid bulk are negligible (step 4). Oxygen has a low solubility in aqueous solutions. The main resistance in the transfer is considered to be the liquid film surrounding the gas bubble [12] (step 3). The liquid film surrounding the bacteria (step 5) also contributes with a resistance. However, as the bacteria are smaller than the bubbles, they have a higher contact area per volume, and the resistance is negligible compared to that of the bubbles. The resistance over the interface and the intracellular diffusion (step 6 and 8) are also neglected. In figure 2.1.3 an individual cell and a cell clump are shown. If the cell density is high the cells can flocculate, which means they form large clumps of cells. The flocculation might give a significant intra-particle resistance (step 7) and the additional resistance needs to be taken into consideration. For a well mixed solution the frequency of cell clumps is reduced [12].

Based on the assumption of the liquid side stagnant film surrounding the gas bubble to be the main resistance to mass transfer, the following standard relation is used to express the mass flux of a component:

$$N_k = k_{L,k} a(\rho^*_{l,k} - \rho_{l,k}) \tag{2.1.2}$$

where N_k is the mass flux for component k, $k_{L,k}$ is the liquid side mass transfer coefficient, a is the gas-liquid contact area, $\rho^*_{l,k}$ is the liquid density of component k in equilibrium with the gas phase at the interface, and $\rho_{l,k}$ is the bulk liquid density of component k. The derivation of equation (2.1.2) is given in Appendix A.5

To ensure that the reader have the different mass transfer models fresh in mind, the models used as basis for the mass transfer coefficients in this project will be briefly outlined.

Film Theory

In the film theory, which is the simplest model for interfacial mass transfer, it is assumed that there exists a thin stagnant film on both sides of the interface. A schematic view of the film theory is shown in Figure 2.1.4. The figure is based on the figure of film theory in the book by Jakobsen [22]. The concentration differences occur over the gas and liquid film, l_G and l_L respectively, shown in Figure 2.1.4. The bulk is assumed to be perfectly mixed. The flux is assumed to be caused by molecular diffusion in the direction normal to the interface [22]. At the gas-liquid interface there exist a hypothetical equilibrium, thus the flux across the film can be given as a steady diffusion flux.

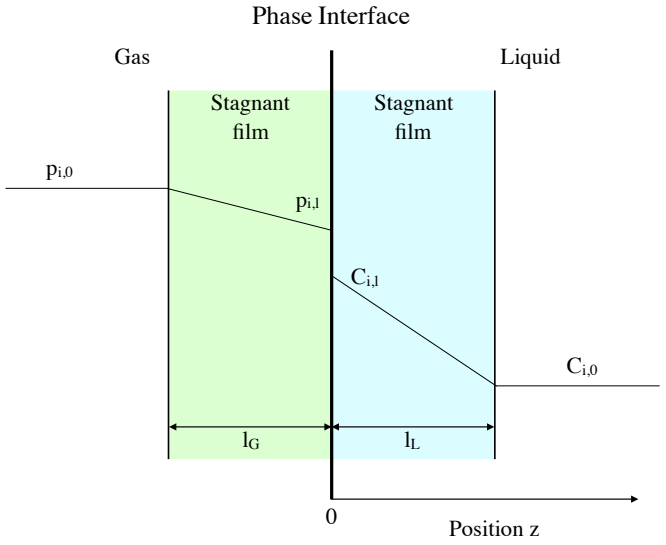

Figure 2.1.4: Two-film theory, where the pressure stays constant on the gas side, drops over the gas film, the concentration over the liquid film decrease, and the concentration in the liquid is constant due to the assumption of perfect mix. The figure is based on the figure in the book by Jakobsen [22].

Figure 2.1.4 shows that the partial pressure and concentrations are constant over the bulk phase due to perfect mixing, and the partial pressure and concentration drop occur over the films.

The film theory is in most cases an inaccurate description of real systems. However, it is a simple method for calculating the interfacial mass fluxes and is therefore a widely used method [22].

Penetration Theory and Surface Renewal

In the penetration theory formulated by Higbie [20], it is assumed that small fluid elements existing in the liquid surface are present close to the bubble surface for a period of time. The time the element stays close to the interface

is defined as the surface contact time, τ_c. This contact time between the fluid elements and the bubble surface is assumed to be the same for all the elements. After this exposure time the fluid element penetrates into the liquid bulk and is replaced by a new element [22]. Depending on the flow properties, laminar or turbulent, different correlations for the contact time are used. For small contact times there will be an unsteady diffusion. For large contact times the diffusion process will reach a steady state and the penetration theory predictions will then correspond to the limiting case in the film theory described previously [22].

An alternative and improved description of the gas-liquid mass transfer compared to the film theory, is the surface renewal theory. The penetration theory can be regarded as the original surface-renewal theory. The surface renewal theory is based on the elements, or eddies, being renewed due to the turbulent properties of the flow. In the surface renewal theory the elements stay close to the interface with varying time. The turbulent motions are characterized by eddies of different size. Mass exchange will occur between the fluid element present on the liquid side and the gas bulk due to unsteady diffusion processes [22]. A schematic view of an eddy present close to the interface, based on the figure of surface renewal in the book by Jakobsen [22], is shown in Figure 2.1.5.

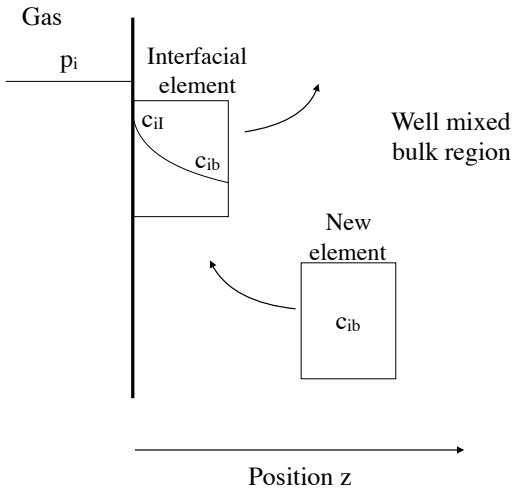

Figure 2.1.5: Principle of surface renewal, where an element in the bulk transport to near the gas-liquid interface. Mass transfer takes place, and the element transport out in the well mixed region. The figure is based on the figure in the book by Jakobsen [22].

In Figure 2.1.5 the element moves from the liquid bulk to near the surface of the gas bubble. A concentration gradient occurs across the interfacial element and mass will exchange between the two phases. After a time the element is replaced with a new element resulting in a change in the diffusion flux [22].

Boundary Layer Theory

Boundary layer theory is divided into laminar- or turbulent boundary layer theory. Boundary layer theory connects the momentum balance with the heat and mass transfer. In these theories the result is analytical solution, and could by this be regarded as more accurate representations than the film theory or the surface renewal theory [22].

2.1.2 Mass Transfer Coefficient

In order to increase the mass flux, it can be seen from equation (2.1.2) that either the mass transfer coefficient, the contact area must increase or the driving force must increase. To increase the contact area the bubble size can be reduced as small bubbles have a larger contact area per volume of gas than larger bubbles. In addition, small bubbles have a lower rising velocity, leaving the bubbles to stay in the solution for a longer period of time, resulting in more time for the gas components to move from the gas bubble to the liquid phase. Doran [12] states that it is desired to have bubbles not smaller than $2-3$ mm, as the bubbles will act as rigid spheres and the gas circulation inside the bubbles will be negligible. If this is assumed to imply no mixing the concentration in the gas-film will equilibrate very fast with that in the liquid and the driving force will approach zero. With no mixing inside the bubble, the rest of the gas components will be transported by molecular diffusion to the surface. This could be a slow process and could result in the oxygen not being fully utilized. Doran [12] further state that k_L will decrease with decreasing bubble size below 2 mm. To verify these statements experiments should be performed to investigate the transfer of gas components for bubbles < 2 mm.

There are several factors affecting the mass transfer coefficient, among them are the presence of surfactants. Surfactants are surface active components which will immobilize the interface. According to Olsen et al. [29], systems can be characterized as clean, partially contaminated or contaminated. Usually, only distilled water is considered as clean. If the concentration of contaminants in a solution is low the solution is considered to be partly contaminated [29]. If the system is partly contaminated, the large bubbles will be able to shed the surrounding layer of contaminants and large bubbles will behave as in a clean system, while the smaller bubbles will behave as in a contaminated one.

If the the coefficients dependent on the bubble size, the mass transfer coefficient will change over the tube. In the simulations of the SCP production, the bubbles are assumed to be homogeneous. In the second part of the thesis, where a single bubble rising in a tube is modeled, the variation in bubble size is taken into account. The mass transfer coefficients will then be a function of the time. In order to find a proper mass transfer coefficient several correlations given in table 2.1.1, will be investigated.

Table 2.1.1: Correlations for the mass transfer coefficients, where C denotes a clean system, PC denotes a partly contaminated sytem, Co a contaminated system, sb and lb means small and large bubbles, respectively, L denotes laminar flow, T is turbulent flow, and Sm and Lm are small- and large eddy model, respectively.

Source	Flow	State	Correlation	Based on model
Higbie [20]	L	C	$k_L = \frac{2}{\pi^{1/2}}(ReSc)^{1/2}\left(\frac{D_l}{d_b}\right)$	Penetration
Calderbank et al. [9]	L	C, sb	$k_L = 0.31\left(\frac{\Delta\rho\mu_l g}{\rho_l^2}\right)^{1/2} Sc^{-2/3}$	Empirical
Calderbank et al. [9]	L	C, lb	$k_L = 0.42\left(\frac{\Delta\rho\mu_l g}{\rho_l^2}\right)^{1/3} Sc^{-1/2}$	Empirical
Brauer [7]	L	C	$k_L = 2 + 0.015Re^{0.89}Sc^{0.7}\left(\frac{D_l}{d_b}\right)$	Boundary layer
Clift et al. [10]	L	PC	$k_L = \frac{2}{\pi^{1/2}}Re^{1/2}Sc^{1/2}\left(\frac{D_l}{d_b}\right)\left(1 - \frac{2.89}{(max(2.89,(Re^{1/2})))}\right)^{1/2}$	Penetration
Brauer [7]	L	PC	$k_L = 2 + 0.015Re^{0.89}Sc^{0.7}\left(\frac{D_l}{d_b}\right)$	Boundary layer
Bird et al. [3]	L	Co	$k_L = (4 + 1.21Re^{2/3}Sc^{2/3})^{1/2}\left(\frac{D_l}{d_b}\right)$	Boundary layer
Hughmark [21]	L	Co	$k_L = 2 + 0.95Re^{1/2}Sc^{1/3}\left(\frac{D_l}{d_b}\right)$	Boundary layer
Brauer [7]	L	Co	$k_L = 2 + 0.015Re^{0.89}Sc^{0.7}\left(\frac{D_l}{d_b}\right)$	Boundary layer
Fröessling [16]	L	Co	$k_L = 2 + 0.6Re^{1/2}Sc^{1/3}\left(\frac{D_l}{d_b}\right)$	Boundary layer
Rzehak [32]	T Sm		$k_L = 0.71\frac{(D_A\nu)^{1/2}}{d_c}\left(\frac{v_l d_c}{\nu}\right)^{0.69}$	Surface renewal, ϵ by wall friction
Rzehak [32]	T Lm		$k_L = 1.7\frac{(D_A\nu)^{1/2}}{d_c}\left(\frac{v_l d_c}{\nu}\right)^{0.46}$	Surface renewal, ϵ by wall friction

Additional theory on the contact time and the turbulent dissipation is given in appendix A.1, where the mass transfer coefficients suggested by Rzehak [32] have been derived from the correlation for mass transfer suggested by Higbie [20]. The mass transfer coefficients are derived when the turbulent dissipation energy is dominated by wall friction only.

As can be seen from Table 2.1.1 the equations are functions of the bubble Reynolds number, Re_b, which is a function of the terminal velocity, v_t, and the drag coefficient, C_D. There are different expressions for the drag coefficient depending on the system; clean, partly contaminated, or contaminated, thus there will be different correlations for the terminal velocity and the bubble Reynolds number. To solve these dependent equations fixed point iteration has

been used.

The bubble Reynolds number is given as:

$$Re_b = \frac{\rho_l d_b v_t}{\mu_l} \tag{2.1.3}$$

where μ_l is the dynamic viscosity of the liquid and the terminal velocity, v_t, will vary with type of system. The bubble Reynolds number is dependent on the system and can be denoted as Re_{clean}, $Re_{partial}$, or Re_{cont} for clean, partly contaminated, or contaminated systems, respectively.

On a general form the terminal velocity, which is the relative velocity between the bubble and the liquid, is given as:

$$v_t = \left(\frac{4}{3} \frac{g d_b}{C_D} \frac{\rho_l - \rho_b}{\rho_l} \right)^{1/2} \tag{2.1.4}$$

where C_D is the steady drag coefficient, given in table 2.1.2.

When a bubble starts to rise in a tube, the bubble rises with an unsteady velocity. This means that the sum of all the forces does not equate to zero in the momentum balance. After a while all the forces are balanced and the bubble reaches a steady velocity, the terminal velocity.

The drag coefficient, C_D, used in (2.1.4), is the steady drag coefficient which is based on the relative velocity being a steady velocity. The drag coefficient for clean, partly contaminated, and contaminated systems are given in table 2.1.2.

Table 2.1.2: Steady drag coefficient [29]

System	Steady Drag Coefficient
Clean	$C_D = \max\{\min[\frac{16}{\mathrm{Re}}(1+0.15\mathrm{Re}^{0.687}), \frac{48}{\mathrm{Re}}], \frac{8}{3}\frac{\mathrm{E_o}}{\mathrm{E_o}+4}\}$
Partly Contaminated	$C_D = \max\{\min[\frac{24}{\mathrm{Re}}(1+0.15\mathrm{Re}^{0.687}), \frac{72}{\mathrm{Re}}], \frac{8}{3}\frac{\mathrm{E_o}}{\mathrm{E_o}+4}\}$
Contaminated	$C_D = \max\{\frac{24}{\mathrm{Re}}(1+0.15\mathrm{Re}^{0.687}), \frac{8}{3}\frac{\mathrm{E_o}}{\mathrm{E_o}+4}\}$

Eötvös number, $\mathrm{E_o}$, in table 2.1.2 is given by equation 2.1.5:

$$E_\mathrm{o} = \frac{(\rho_l - \rho_b) g d_b^2}{\sigma} \tag{2.1.5}$$

where σ is the surface tension and ρ_b is the bubble density.

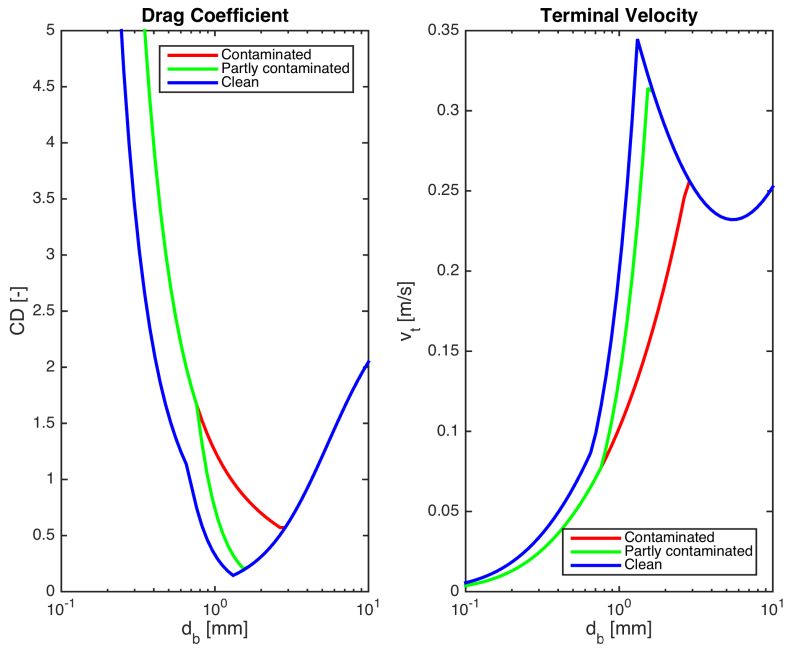

Figure 2.1.6: Steady drag coefficient and terminal velocity varying with the bubble diameter for clean, partly contaminated, and contaminated systems.

From Figure 2.1.6 it can be seen that for bubbles $< 2-3$ mm the drag coefficient and the terminal velocity will be affected by the presence of surfactants. The sharp shift is due to the bubbles shifting from being spherical to non-spherical.

As described above, the expression for the mass transfer coefficient will change with type of system, and for some correlations the coefficient will be a function of bubble size. To see the variation with bubble size the correlations given in table 2.1.1 have been plotted, shown Figure 2.1.7 and Figure 2.1.8. These plots are reproductions of the figures in the article by Olsen et al. [29]. Experimental data found in Heijnen et al. [19] and additional correlations have been added to the original figures by Olsen et al. [29]. The data taken from the article by Heijnen et al. [19] are extracted by using the *WebPlotDigitizer* which is an opensource program for working with plots and images [31].

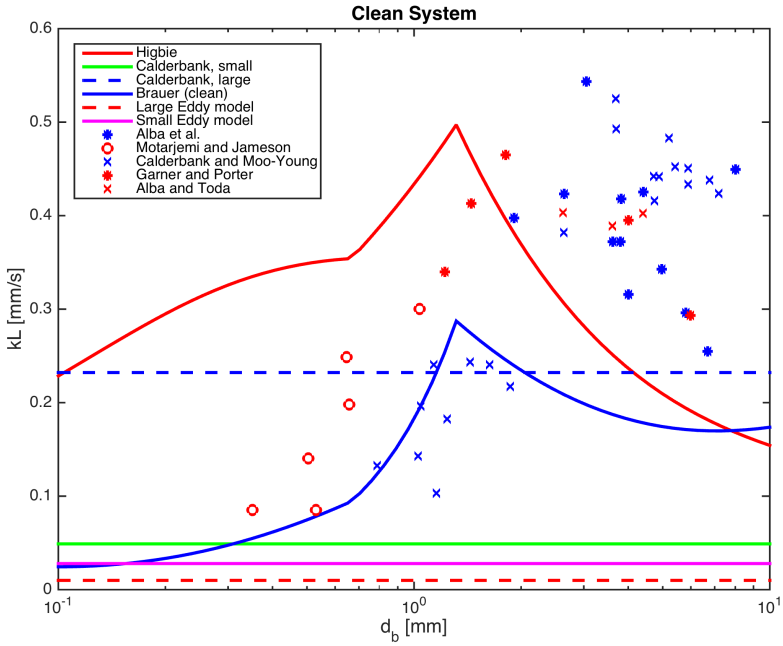

Figure 2.1.7: Mass transfer coefficient as a function of bubble size for clean systems. Mass transfer coefficients are shown with lines and experimental measurements are shown with points.

Figure 2.1.7 shows that for clean systems there are large variations in the measurement data. As are the variations for the different correlations. Comparing the experimental data and the correlations, it can be seen that the relation by Brauer [7] used on clean systems seems to fit the measurement data by Calderbank et al. [9] around bubble size $0.8 - 2.0$ mm relatively well. The correlations suggested by Calderbank et al. [9] for small and large bubbles are independent of the bubble size.

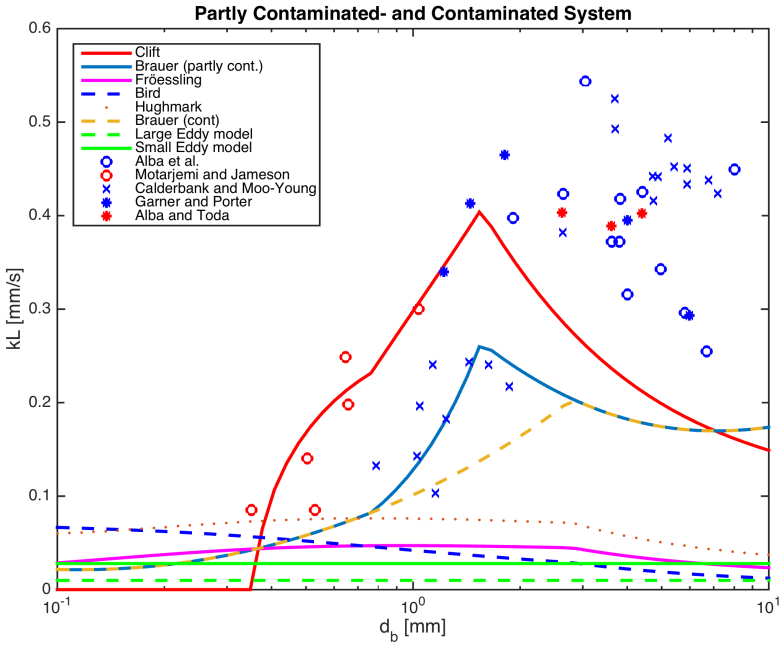

Figure 2.1.8: Mass transfer coefficient as a function of bubble size for partly contaminated and contaminated systems. Lines indicate models and points indicate measurements.

For partly contaminated- and contaminated systems Figure 2.1.8 shows that for several of the coefficients the variation with the bubble size is small. In particular the relations by Hughmark [21] and Fröessling [16] are approximately constant with varying bubble size. As can be seen from table 2.1.1 the mass transfer coefficients for small and large eddy-dominating surface renewal are independent of bubble size. Figure 2.1.8 shows that the coefficient suggested by Clift et al. [10] fits the measurement data by Motarjemi et al. [28] quite well as an average for the data for bubbles of size $0.5 - 1.0$ mm. The correlation by Brauer [7] for partly contaminated systems seems to fit the measurement data by Calderbank et al. [9] around $0.8 - 2.0$ mm. For a contaminated system, neither of the suggested relations seems to fit the experimental data. However, in the article by Olsen et al. [29] it was found that the correlation for mass transfer by

Hughmark [21] reproduced the experimental results obtained by Olsen et al. [29] very well. In the article the correlation by Hughmark [21] was recommended for a contaminated system.

By Figure 2.1.7 and 2.1.8, and from the recommendation for a contaminated system by Olsen et al. [29], the suggested correlations for the mass transfer coefficient are:

Table 2.1.3: Suggested mass transfer coefficients for a clean, partly contaminated and a contaminated system.

System	Mass Transfer Coefficient
Clean	Brauer [7]
Partly Contaminated	Clift et al. [10]
Contaminated	Hughmark [21]

2.2 Kinetics

The cell growth dynamics can be divided into different phases; lag-, acceleration-, growth-, decline-, stationary-, and death phase. In Figure 2.2.1 the stages of the cell growth in a batch culture are shown.

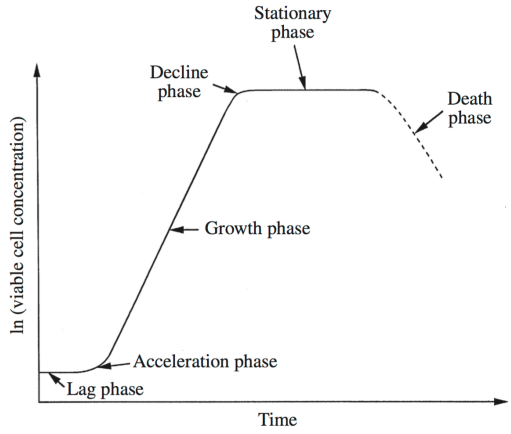

Figure 2.2.1: Change in cell concentration in a batch culture as a function of time. Cell growth stages are shown in the figure, which are taken from Doran [12].

When exposed to new environments, the cell population remains unchanged for a short time as they adapt to the new environment. In the growth phase the cells start to replicate at a constant rate. The kinetic expressions for cell growth in a continuous medium are applied in this phase. When the bacterial growth is inhibited by substrate limitations or other limiting growth conditions, the stationary phase or the death phase is reached. In the stationary phase the cells may replicate but growth is balanced by cell death. When cells die they can lyse and provide a source of nutrients to other cells. [26] This means that an empty carbon source does not necessarily result in a total stagnation in the cell growth. Even in the death phase there may be cells dividing but there is a net loss.

The rate of cell growth is regarded to be a first order reaction given by:

$$r_X = \mu C_X \tag{2.2.1}$$

where r_X is the volumetric rate of biomass, μ is the specific growth rate, and C_X is the concentration of biomass.

To express the specific growth rate, the Monod equation can be used:

$$\mu = \mu_{max} \frac{C_S}{K_S + C_S} \tag{2.2.2}$$

where μ_{max} is the maximum specific growth rate, K_S is the saturation constant for the substrate, and C_S is the substrate concentration. Equation (2.2.2) is an unstructured model where it has been assumed balanced growth. This means that the growth rate is independent of the biomass concentration. The growth phase in Figure 2.2.1 is considered to be balanced growth, and the Monod equation could be applied to this stage. For the other phases in Figure 2.2.1, models which takes into account the variations in biomass needs to be applied.

The saturation constant, K_S, in equation (2.2.2) is the concentration of substrate where the specific growth rate is half of its maximum value, i.e. where $\mu = \mu_{max}/2$. From the Monod equation it can be seen that when $K_S << C_S$, the specific growth rate will approach its maximum. As the substrate is consumed by the bacteria, the substrate concentration will approach the value of the affinity constant and the growth stagnates. The specific growth rate and the substrate saturation constants are said to be cell-substrate specific, meaning they are dependent on the specific cell and substrate.

In cell growth with several substrates present it is common that one of the substrates behave as the growth-limiting substrate. There are however cases when more than one substrate limit the growth and equation (3.2.11) needs to be extended. The extended Monod equation used in the SCP simulations is given by equation (2.2.3):

$$\mu = \mu_{max,1} \frac{C_{S,1} C_{S,2}}{(K_{S,1} + C_{S,1})(K_{S,2} + C_{S,2})} \tag{2.2.3}$$

where $\mu_{max,2} = 1$ as oxygen is assumed to reach 100% of its maximum value, $C_{S,1}$ and $K_{S,1}$ are the concentration and affinity constant for methane, and

$C_{S,2}$ and $K_{S,2}$ are the concentration and affinity constant for oxygen. In the extended Monod equation (2.2.3) the kinetics for both methane and oxygen have been included, and the subscripts $S,1$ and $S,2$ denotes methane and oxygen, respectively.

Substrate uptake

The substrate present is taken up by the cells. The substrate uptake rate can be given by:

$$r_S = \frac{r_X}{Y_{XS}} + m_S C_X \tag{2.2.4}$$

here Y_{XS} is the theoretical yield coefficient of biomass from substrate and m_S is the maintenance coefficient.

In SCP production the maintenance is neglected, i.e. m_S is neglected, equation 2.2.5 becomes:

$$r_S = \frac{r_X}{Y_{XS}} \tag{2.2.5}$$

Neglecting the maintenance means that it is assumed that all the energy goes to the production of the desired product.

Cell Death

The rate of cell death can be described by the first order reaction:

$$r_d = k_d C_X \tag{2.2.6}$$

where k_d is the specific death constant. When comparing k_d to the specific growth rate, μ, a common case is that $k_d << \mu$. The cell death is neglected in SCP production.

Chapter 3

Mathematical Model

In this chapter the model equations used in SCP production will be given. The solution method and the implementation of the equations will be presented.

In reactor simulations of SCP production in this work, a vertical bubble column is used. Figure 2.1.1 in section 2.1 shows a system with bubbles of equal size. In a real system the bubbles will be of different size along the tube due to coalescence and breakage. As a simplification the column is assumed to contain homogeneous bubbles, meaning bubbles of equal size. Even though this is a rough assumption it gives a good idea of how the parameters will change along the reactor tube.

The bubble column is modeled as a steady-state one-dimensional axial dispersion model, with a pseudo-homogeneous model description for the slurry phase. Mass and energy balances are formulated for the gas and the liquid (slurry) phase and are solved with the orthogonal collocation method. To describe the evolution of the gas velocity the continuity equation, conservation of mass, is solved with respect to the gas velocity. The gas is assumed to be ideal. It is assumed that axial pressure is dominated by static pressure of the liquid phase, and the gas pressure is assumed to be that of the liquid. The ammonia is assumed to stay in liquid phase throughout the reactor length. It is assumed that the substrate only contribute with energy to growth of the cells, and the maintenance has the therefore not been included in the model. The fermentation broth exhibit Newtonian fluid properties, meaning the viscosity of the fluid is independent of the shear stress and the velocity. The main convection as assumed to be in the axial direction, thus the r- and θ-coordinates are negligible. Maintenance requirements and cell death are neglected in the model.

The inlet values and the operating conditions used in the simulations are based on values from the patented U-loop technology by Larsen [24] and from the article by Taweel et al. [42]. The inlet operating conditions are given in table 5.1.1.

Table 3.0.1: Operating conditions in SCP simulations.

Parameter	Value	Unit
$p_{l,out}$	3	Pa
T_g, T_l	298	K
$T_w all$	316	K
v_g^s	0.05	ms^{-1}
v_l^s	0.40	ms^{-1}
ε_g	0.11	-
ε_l	0.89	-
z_{max}	12	m
d_c	0.2	m
d_b	0.002	m

The inlet mass fractions used in the simulations are given in table 3.0.2.

Table 3.0.2: Initial mass fractions for the components.

Component	$w_{i,g}$ $kg_i kg_{tot}^{-1}$	$w_{i,l}$ $kg_i kg_{tot}^{-1}$
CH_4	0.23	0.0000
O_2	0.77	0.0000
NH_3	0.00	0.0049
CO_2	0.00	0.0000
X	0.00	0.0300
H_2O	0.00	0.9651

3.1 Pressure and Velocity

Pressure

The pressure in the liquid phase can be expressed as:

$$\frac{dp_L}{dz} = -\varepsilon_L \rho_L g_z \tag{3.1.1}$$

where g_z is the acceleration due to gravity working in the opposite direction relative to the gas flow, and ε_l is the liquid hold-up.

Velocity

To describe the behavior of the gas velocity along the reactor length, the continuity equation is used:

$$\frac{\partial(\rho_G v_G^S)}{\partial z} = -\sum_k k_{L,i} a(\rho_{L,i}^* - \rho_{L,i}) \tag{3.1.2}$$

where v_G^s is the superficial gas velocity, ρ_G is the gas density, $k_{L,i}$ is the mass transfer coefficient of component i, $\rho_{L,i}^*$ is the gas liquid equilibrium density of component i at the interface, and ρ_L is the density in the liquid bulk. The negative mass flux is due to the gas leaving the bubble. The gas-liquid contact area a is given as:

$$a = \frac{6\varepsilon_G}{d_b} \tag{3.1.3}$$

where d_b is the gas-bubble diameter assumed to be $2.0 \cdot 10^{-3}$m.

Solving for the gas velocity, equation 3.1.2 becomes:

$$v_G^S \frac{\partial \rho_G}{\partial z} + \rho_G \frac{\partial v_G^S}{\partial z} = -\sum_i k_{L,i} a(\rho_{L,i}^* - \rho_{L,i}) \tag{3.1.4}$$

$$\tag{3.1.5}$$

The superficial velocities are given by the hold-up and the local velocity for the phase:

$$v_L^S = \varepsilon_L v_L \text{ and } v_G^S = \varepsilon_G v_G \tag{3.1.6}$$

where v_L and v_G are the local velocities.

The gas- and liquid hold-up are calculated from the superficial liquid- and gas velocities:

$$\varepsilon_L = \frac{v_L^S}{v_L^S + v_G^S} \ , \varepsilon_G = \frac{v_G^S}{v_L^S + v_G^S} \tag{3.1.7}$$

It should be noted that the equation used to solve the superficial gas velocity only depends on the gas density and mass flux, as the bubble size is assumed to be constant, and the the forces acting on the rising bubbles is not taken into account.

3.2 Species Mass Balances

Species mass balances are solved for methane, oxygen, ammonia, carbon dioxide, water, and biomass. The reaction occurs in the liquid phase and the reaction term is only included in the liquid phase.

Liquid (Slurry) Phase

The species mass balance in the liquid phase can be written as:

$$\frac{d}{dz}(v_L^S \rho_{i,L}) = \frac{d}{dz}\left(\varepsilon_L D_{z,L}^{\text{eff}} \frac{d\rho_{i,L}}{dz}\right) + k_L a(\rho_{i,L}^* - \rho_{i,L}) + \varepsilon_L R_i \tag{3.2.1}$$

where $D_{z,L}^{\text{eff}}$ is the effective axial dispersion coefficient in liquid phase and $\rho_{i,L}$ is the component density in liquid phase given by:

$$\rho_{i,L} = \rho_L w_{i,L} \tag{3.2.2}$$

where $w_{i,L}$ is the mass fraction of component i in the liquid phase. Rewriting Eq. 3.2.1, gives the following equation for the species mass balance in liquid phase:

$$v_L^S \rho_L \frac{dw_{i,L}}{dz} = \varepsilon_L D_{z,L}^{\text{eff}} \rho_L \frac{d^2 w_{i,L}}{dz^2} + k_L a(\rho_{i,L}^* - \rho_{i,L}) + \varepsilon_L R_i \tag{3.2.3}$$

To express the interfacial gas-liquid equilibrium, Henry's law is used:

$$\rho_{i,L}^* = \frac{w_{i,G} p_G \bar{M}_{w,G}}{H_i} \tag{3.2.4}$$

where $\bar{M}_{w,G}$ is the molar mass of the gas mixture, and H_i is Henry's constant for component i. The values used for Henry's constant and the mixture molar mass are given in Appendix A.6.2. The Henry's law on mass basis is derived in Appendix A.4.

When choosing the value for the effective axial dispersion coefficient, several sources have been investigated. Olsen et al. [29] suggested the effective dispersion coefficient to be $D_{eff} = 103.68$ m^2/h. Wu et al. [47] stated that the value suggested by Olsen et al. [29] was too large for SCP production. In this specific process, the liquid velocity is higher than the gas velocity and it is desired to

have an effective dispersion coefficient that holds for large liquid velocities. The relation for the effective dispersion coefficient by Swarnendu et al. [41] holds for processes with high liquid- and low gas velocity:

$$D_{z,L}^{\text{eff}} = 5.05 v_L^S d_c \left(\frac{f}{2}\right)^{0.5} \tag{3.2.5}$$

here d_c is the column diameter. f is the Darcy friction factor, which holds for Reynolds numbers $2100 < Re_c < 10^5$ and is given by [22]:

$$f = 0.3164 Re_c^{-1/4} \tag{3.2.6}$$

where Re_c is the column Reynolds number. The Darcy friction factor is assumed to hold for the Reynolds number in the SCP simulations being $1.33 \cdot 10^5$.

There are several correlations for the mass transfer coefficient in the literature and choosing a mass transfer coefficient, k_L, can be quite challenging. For the SCP simulations the correlation by Calderbank et al. [9] for large bubbles has been used:

$$k_L = 0.42 \left(\Delta\rho \mu_L \frac{g}{\rho_L^2}\right)^{2/3} N_{Sc}^{-2/3} \tag{3.2.7}$$

where $\Delta\rho = \rho_L - \rho_G$ is the difference in density between the slurry and the gas, and μ_L is the liquid viscosity. N_{Sc} is the Schmidt number given by:

$$N_{Sc} = \frac{\mu_l}{\rho_l D_l} \tag{3.2.8}$$

where D_l is the mass diffusivity. The molecular diffusivities are given in appendix A.6.2.

It should be noted that the correlation for the mass transfer coefficient proposed by Calderbank et al. [9] was found from experiments where clean water was used. As the fermentation broth in the SCP process contains salts and minerals, choosing a mass transfer coefficient based on a clean system could be misleading.

The reaction rate, R_i, which is a function of the biomass reaction rate, r_X, is expressed as:

$$R_i = -Y_{iX} M_i r_X \tag{3.2.9}$$

here Y_{iX} is the theoretical yield coefficient, meaning the stoichiometric coefficients, and the subscript iX indicates the yield of component i per biomass X produced. M_i is the molar mass of component i. The yield coefficients can be found in appendix A.6.2.

The biomass reaction rate on mass basis is given as:

$$r_X = \mu \frac{\rho_L w_{X,L}}{M_X} \tag{3.2.10}$$

The specific growth rate is given by the Monod equation described in section 2.2:

$$\mu = \mu_{\max,\mathrm{S}_1} \mu_{\max,\mathrm{S}_2} \frac{\rho_L w_{\mathrm{S}_1,L}/M_{\mathrm{S}_1}}{\mathrm{K}_{\mathrm{S}_1} + \rho_L w_{\mathrm{S}_1,L}/M_{\mathrm{S}_1}} \frac{\rho_L w_{\mathrm{S}_2,L}/M_{\mathrm{S}_2}}{\mathrm{K}_{\mathrm{S}_2} + \rho_L w_{\mathrm{S}_2,L}/M_{\mathrm{S}_2}} \tag{3.2.11}$$

The values for the affinity constants and the maximum specific growth rate used in the SCP simulations are given in table 3.2.1:

Table 3.2.1: Kinetic Parameters

Symbol	Value	Unit	Source
$\mu_{\max,\mathrm{S}_1}$	$1.03 \cdot 10^{-4}$	s^{-1}	Olsen et al. [29]
$\mathrm{K}_{\mathrm{S},1}$	$2.11 \cdot 10^{-8}$	$kg_{S,1}/kg_{tot}$	Taweel et al. [42]
$\mathrm{K}_{\mathrm{S},2}$	$6.46 \cdot 10^{-8}$	$kg_{S,2}/kg_{tot}$	Olsen et al. [29]

The affinity constant for O_2 found from Olsen et al. [29] was based on an experiment where methanol was used as substrate and with *Methylococcus capsulatus*. As the same bacteria is used in this work, it is assumed that the affinity constant from Olsen et al. [29] can be used.

Gas Phase

The species mass balance for the gas phase can be expressed by equation 3.2.12:

$$\frac{d}{dz}(v_G^S \rho_{i,G}) = \frac{d}{dz}\left(\varepsilon_G D_{z,G}^{eff} \frac{d\rho_{i,G}}{dz}\right) - k_L a(\rho_{i,L}^* - \rho_{i,L}) \tag{3.2.12}$$

where the component density in gas phase is given as:

$$\rho_{i,G} = \rho_G w_{i,G} \tag{3.2.13}$$

The total gas density, ρ_G, is calculated from the ideal gas law:

$$\rho_G = \frac{p_G}{RT}\bar{M}_{w,G} \tag{3.2.14}$$

here p_G is the total gas pressure and $\bar{M}_{w,G}$ is the molecular mass of the gas mixture. The effective axial dispersion coefficient in the gas phase is taken from Sehabiague et al. [34] to be:

$$D^{\text{eff}}_{z,G} = D^{eff}_{z,L}\left(1 - \frac{d_b^{2.5}}{d_{b0}^{2.5} + d_b^{2.5}}\right) \tag{3.2.15}$$

here $d_{b0}^{2.5}$ is the smallest diameter of the larger bubbles. With the assumption of homogenous gas-bubbles, $d_{b0}^{2.5} = d_b^{2.5}$.

Rewriting Eq. 3.2.12 gives:

$$\begin{aligned} v_G^S \rho_G \frac{\partial w_{i,G}}{\partial z} + w_{i,G}\frac{\partial(\rho_G v_G^S)}{\partial z} = {} & D^{\text{eff}}_{z,G}\varepsilon_G\rho_G\frac{\partial^2 w_{i,G}}{\partial z^2} \\ & + D^{\text{eff}}_{z,G}\varepsilon_G\frac{\partial \rho_G}{\partial z}\frac{\partial w_{i,G}}{\partial z} \\ & + D^{\text{eff}}_{z,G}\rho_G\frac{\partial \varepsilon_G}{\partial z}\frac{\partial w_{i,G}}{\partial z} \\ & - k_L a(\rho^*_{i,L} - \rho_{i,L}) \end{aligned} \tag{3.2.16}$$

The second term on left hand side can be replaced by the continuity equation 3.1.2. The component mass balance for the gas phase becomes:

$$\begin{aligned} v_G^S \rho_G \frac{\partial w_{i,G}}{\partial z} - \sum_i k_{L,i} a(\rho^*_{L,i} - \rho_{L,i}) = {} & D^{\text{eff}}_{z,G}\varepsilon_G\rho_G\frac{\partial^2 w_{i,G}}{\partial z^2} \\ & + D^{\text{eff}}_{z,G}\varepsilon_G\frac{\partial \rho_G}{\partial z}\frac{\partial w_{i,G}}{\partial z} \\ & + D^{\text{eff}}_{z,G}\rho_G\frac{\partial e_G}{\partial z}\frac{\partial w_{i,G}}{\partial z} \\ & - k_L a(\rho^*_{i,L} - \rho_{i,L}) \end{aligned} \tag{3.2.17}$$

3.3 Temperature Equations

With the reaction occurs in the liquid phase and the reaction being exothermic, heat will be transferred from the liquid to the gas phase and to the surroundings.

Liquid (Slurry) Phase

The temperature in the liquid phase can be given by equation 3.3.1:

$$\rho_L C_{p,L} v_L^S \frac{dT_L}{dz} = \frac{d}{dz}\left(\varepsilon_L k_L^{\text{eff}} \frac{dT_L}{dz}\right) - h_L a(T_L - T_G) \tag{3.3.1}$$

$$+\varepsilon_L \sum_r (-\Delta H_r) R_{r,L} \tag{3.3.2}$$

$$-\frac{4U}{d_c}(T_L - T_{\text{eff}})$$

where $C_{p,L}$ is the mixture heat capacity of the liquid, k_L^{eff} is the effective thermal conductivity, h_L is the convective heat transfer coefficient, T_L is the temperature in the liquid, T_G is the gas temperature, T_{wall} is the wall temperature, ΔH_r is the reaction heat, and U is the overall heat transfer coefficient. The negative heat flux form liquid to gas, and from liquid to the wall is due to the heat being transported out of the liquid phase. It is assumed that the wall temperature is constant due to cooling medium surrounding the reactor. The cooling medium is not included in the model. The mixture heat capacity of the liquid, $C_{p,L}$, is expressed as:

$$C_{p,L} = \sum_i c_{p,i,L} w_{i,L} \ , \ i = \text{H}_2\text{O}, \text{NH}_3, \text{X} \tag{3.3.3}$$

The specific heat capacities, $c_{p,i,L}$, are given in Appendix A.6.2.

The effective thermal conductivity, k_L^{eff} is given by:

$$k_L^{\text{eff}} = D_{z,L}^{\text{eff}} \rho_L C_{p,L} \tag{3.3.4}$$

The convective heat transfer coefficient from liquid to gas, h_L, is taken from Calderbank et al. [9]:

$$h_L = \rho_L \bar{k_L} C_{p,L} \left(\frac{\mu_L}{(\rho_L D_L)^{2/3}}\right) \left(\frac{C_{p,L}\mu_L}{\lambda_L}\right)^{-2/3} \tag{3.3.5}$$

where λ_L is the thermal conductivity of water and $\bar{k_L}$ is the average heat transfer coefficient given as:

$$\bar{k_L} = \sum_k k_{L,k} w_{k,L} \tag{3.3.6}$$

where $k_{L,k}$ is the mass transfer coefficient of component k.

The overall heat transfer coefficient, U, is given by:

$$\frac{1}{U} = \frac{1}{h_L} + \frac{t_w}{k_{\text{eff}}} + \frac{1}{h_{\text{eff}}} \tag{3.3.7}$$

where k_{steel} is the thermal conductivity of the wall material. The wall is assumed to be of stainless steel, and the thikness of the wall, $t_w = 1$ cm. h_{cool} is the heat transfer coefficient of the cooling medium surrounding the column, assumed to have a constant temperature of $T_{wall} = 43°\text{C}$. Doran [12] suggested that in aerobic reactions a good estimate is that consumption of one mole O_2 releases 460 kJ, i.e. $\Delta H_{rx} \approx -460$ kJ per mole O_2 consumed. This was also suggested by Villadsen [45] in the Norferm process and has been used in this work.

Gas Phase

The temperature in the gas phase is given by equation 3.3.8:

$$\rho_G C_{p,G} v_G^S \frac{dT_G}{dz} = \frac{d}{dz}\left(\varepsilon_G \lambda_{z,G}^{\text{eff}} \frac{dT_G}{dz}\right) + h_L a (T_L - T_G) \tag{3.3.8}$$

where $C_{P,G}$ is the mixture heat capacity in gas phase and $\lambda_{z,G}^{\text{eff}}$ is the effective thermal conductivity in gas phase. The positive heat flux is due to the heat being transferred from the liquid to the gas phase.

The effective thermal conductivity of the gas phase is given as:

$$\lambda_{eff,z,G} = D_{z,G}^{\text{eff}} \rho_G C_{P,G} \tag{3.3.9}$$

The heat capacity of the gas phase is calculated as:

$$C_{P,G} = \sum_i c_{p,i,G} w_{i,G} \ , \ i = \text{CH}_4, \text{O}_2, \text{CO}_2 \tag{3.3.10}$$

where the specific heat capacities for the gas components, $c_{p,i,g}$, are given in Appendix A.6.2.

Inserted for the effective thermal conductivity, the temperature balance for the gas phase can be written as:

$$\rho_G C_{p,G} v_G^S \frac{dT_G}{dz} = \varepsilon_G D_{z,G}\text{eff} \frac{d}{dz}\left(\rho_G C_{P,G} \frac{dT_G}{dz}\right) + h_L a(T_L - T_G) \qquad (3.3.11)$$

where the heat capacity and the density in the gas phase changes with temperature.

3.4 Boundary Conditions

To be able to solve the species mass balances and the temperature equations boundary conditions are needed. The equations are solved with the standard Danckwerts boundary conditions.

Species Mass and Temperature

At the inlet $z = 0$, the boundary conditions for for the species mass and temperature for the phase $k = [L, G]$ are given by equation 3.4.1 and 3.4.2, respectively:

$$\rho_k(0) v_k^S(0) \omega_{i,k}(0) - \varepsilon_k(0)\rho_k(0) D_{k,z}^{\text{eff}}(0) \frac{d\omega_{i,k}(0)}{dz} = v_{in,k}^S \rho_{in,k} \omega_{i,k,in} \qquad (3.4.1)$$

$$\rho_k(0) v_k^S(0) C_{p,k}(0) T_k(0) - \varepsilon_k(0) k_{k,z}^{\text{eff}}(0) \frac{dT_k(0)}{dz} = v_{in,k}^S \rho_{in,k} c_{p,k,in} T_{in,k} \qquad (3.4.2)$$

At the outlet, $z = L$, the boundary condition is given by:

$$\frac{d\omega_k(z = L)}{dz} = \frac{dT(z = L)}{dz} = 0 \qquad (3.4.3)$$

Pressure and Velocity

Initial conditions are required for the pressure and velocity. The initial condition for the pressure is given by:

$$p_l = p_{out} \text{ at } z = L \qquad (3.4.4)$$

where $p_{out} = 3$ bar is the outlet pressure and L is the length of the tube.

The initial condition for the gas velocity is given by:

$$v_g = v_{g,0} \text{ at } z = 0 \tag{3.4.5}$$

where $v_{g,0} = 0.05$ ms^{-1}.

3.5 Solution Method

The chosen solution method for the SCP reactor simulations is the orthogonal collocation method.

The following section is based on the theory presented in Solsvik et al. [35]. To solve the model equations the equations have been implemented in MATLAB and solved numerically by the orthogonal collocation method. The orthogonal collocation method is in the family of the weighted residual method and is a higher order solution method. The weighted residual methods give accurate solutions with little computational time. Orthogonal collocation is a spectral method.

The spectral method representation of the solution function is based on the entire domain, through a truncated series expansion. In order to solve the system of equations the domain needs to be discretized. The discretization includes choosing a set of nodal points, which are the points where the solutions are approximated. In the spectral method all the nodal points are considered when approximating a solution point. The nodal points are referred to as collocation points if they are taken as zeros of an orthogonal polynomial in the family of Jacobi polynomials. The Legendre polynomials have been chosen in this work. In this specific problem the boundary conditions are enforced as additional constraints as they are implemented on the strong form. Boundary points are chosen in both ends in addition to all the internal points. This node configuration is called the Gauss−Lobatto−Legendre configuration.

The solution function can be expressed by the following approximation:

$$f_{ex}(\xi) \approx f(\xi) = \sum_{j=0}^{P} \alpha_j \phi_j^P(\xi) \tag{3.5.1}$$

where $\phi_j^P(\xi)$ is the basis function of order P, α_j are the basis coefficients and ξ is the collocation point.

The basis functions are chosen to be the Lagrangian basis polynomials:

$$L_j^P(\xi) = \prod_{i=0, i\neq j}^{P} \frac{\xi - \xi_i}{\xi_j - \xi_i} \tag{3.5.2}$$

where L_j^P is the Lagrangian basis polynomial of order P.

The Lagrange polynomial has the following property:

$$L_j^P(\xi_i) = \begin{cases} 1 & \text{if } i = j \\ 0 & \text{if } i \neq j \end{cases} \tag{3.5.3}$$

For a one-dimensional problem, the solution function approximation can be expressed by the following taylor series expansion:

$$f_{ex}(\xi) \approx f(\xi) = \sum_{j=0}^{P} f_j L_j^P(\xi) \tag{3.5.4}$$

where the basis coefficients $\alpha_j = f_j$, which are solution function values at the collocation points.

In the weighted residual method the minimization of the inner product can be written in the following generalized way:

$$\int_\Omega R(\xi; f_0^P, f_1^P, ..., f_P^P)\omega_i(\xi)d\Omega = 0 \tag{3.5.5}$$

where R is the residual, ω_i are the weighting functions taken as the Dirac delta function, $w_i = \delta(\xi - \xi_i)$, in the orthogonal collocation method. The residual is defined as the error between the analytical and the numerical solution:

$$R = \sum_{j=0}^{P} f_j^P \mathscr{L} L_j^P(\xi) - g(\xi) \tag{3.5.6}$$

where $\mathscr{L}$ is a linear operator and $g(\xi)$ is the source vector.

The Dirac delta function has the following property:

$$\int_{\Omega} \delta(\xi - \xi_i) d\xi = \begin{cases} 1 & \text{if } \xi = \xi_i \\ 0 & \text{if } \xi \neq \xi_i \end{cases} \tag{3.5.7}$$

The differential equation is exactly satisfied when $\xi = \xi_i$.

This results in the inner product being simplyfied to the following expression:

$$[w_{\Omega,i}, R_{\Omega}] = \int_{\Omega} w_{\Omega,i} R_{\Omega} d\Omega \tag{3.5.8}$$

$$[\delta(\xi - \xi_i), R^P_{\Omega}(\xi; f_0, ..., f_j, ...f_P)] = \int_{\Omega} R^P_{\Omega}(\xi; f_0, ..., f_j, ...f_P)\delta(\xi - \xi_i) d\xi \tag{3.5.9}$$

$$= R^P_{\Omega}(\xi; f_0, ..., f_j, ...f_P)\Big|_{\xi=\xi_i} \tag{3.5.10}$$

$$= \sum_{j=0}^{P} f_j \mathscr{L} L^P_j(\xi_i) - g(\xi_i) \tag{3.5.11}$$

$$= 0 \tag{3.5.12}$$

The equation above may be presented on the form $\mathbf{Af = F}$, where $\mathbf{A}$ is a matrix, $\mathbf{f}$ is the solution vector, and $\mathbf{F}$ is the source vector.

$$[\mathbf{A}]_{ij} = \mathscr{L} L^P_j(\xi_i) = [\mathbf{L}]_{ij} \tag{3.5.13}$$

$$[\mathbf{F}]_i = g(\xi_i) \tag{3.5.14}$$

$$\mathbf{f} = [f_0, f_1, ..., f_P]^T \tag{3.5.15}$$

The species mass balance in gas phase for component k, equation (3.2.16), can

be expressed as:

$$v_G^S(z_i)\rho_G(z_i)\sum_j w_{k,g,j}\frac{\partial L_j(z_i)}{\partial z}+\sum_j w_{k,g,j}\sum_j \rho_{G,j}v_{G,j}^s\frac{\partial L_j(z_i)}{\partial z}= \tag{3.5.16}$$

$$D_{eff,g}\varepsilon_G(z_i)\rho_G(z_i)\sum_j w_{k,g,j}\frac{\partial L_j^2(z_i)}{\partial z}$$

$$+\varepsilon_G(z_i)D_{eff,g}\sum_j \rho_{G,j}\frac{\partial L_j(z_i)}{\partial z}\sum_j w_{k,g,j}\frac{\partial L_j(z_i)}{\partial z}$$

$$+\rho_G(z_i)D_{eff,g}\sum_j \varepsilon_j\frac{\partial L_j(z_i)}{\partial z}\sum w_{k,g,j}\frac{\partial L_j(z_i)}{\partial z}$$

$$-\frac{k_{L,k}(z_i)P(z_i)}{\bar{M}(z_i)H_k}\sum_j w_{k,g,j}+\sum_i k_{L,k}(i)a(i)\rho_l w_{k,l}$$

where i is the collocation point, j is the polynomial, and k is the component.

In MATLAB the algebraic equation system is placed in the following way:

$$\begin{bmatrix} A_{11} & A_{12} & A_{13} & \dots & A_{1n} \\ A_{21} & A_{22} & A_{23} & \dots & A_{2n} \\ \vdots & \vdots & \vdots & \ddots & \vdots \\ A_{n1} & A_{n2} & A_{n3} & \dots & A_{nn} \end{bmatrix} \begin{bmatrix} f_1 \\ f_2 \\ \vdots \\ f_n \end{bmatrix} = \begin{bmatrix} F_1 \\ F_2 \\ \vdots \\ F_n \end{bmatrix}$$

An example on how the parts of the gas species mass balance could be stored in the $\mathbf{A}-$matrix and the $\mathbf{F}$-vector is shown below.

$$\begin{aligned} A(i,j) = {} & v_G\rho_G\text{derz}(i,j)+\Gamma(i)\text{Lagz}(i,j) \\ & -\varepsilon_G(i)D_{eff,g}\rho_G(i)\text{der2z}(i,j) \\ & -\varepsilon_G(i)D_{eff,g}d\rho_G(i)\text{derz}(i,j) \\ & -\rho_G(i)D_{eff,g}d\varepsilon_G(i)\text{derz}(i,j) \\ & +\frac{k_L(i,k)a(i)P(i)\text{Lagz}(i,j)}{\bar{M}(i)H(k)} \end{aligned} \tag{3.5.17}$$

$$F(i)=\rho_l k_L(i,k)a(i)w_l(i,k) \tag{3.5.18}$$

where lagz(i,j) is the Lagrange polynomial, derz(i,j) and der2z(i,j) are the first derivative and the second derivative in z−direction, $d\rho_G = \sum_j \text{derz(i,j)}\rho_g$ and the solution vector **f** contains the mass fractions in gas phase, w_j. $\Gamma = -\sum_k k_{L,k}a\left(\frac{w_{k,g}p_G\bar{M}}{H_k} - \rho_l w_{k,l}\right)$. Here ρ_g and Γ is found from the previous iteration.

Equation (3.5.19) shows how the **A**−matrix should be multiplied with the **f**-vector:

$$\sum_j A_{ij}f_j = F \tag{3.5.19}$$

By equation (3.5.19) it can be seen that for every row, i, in the **A**−matrix, each column, j, should be multiplied with the corresponding row, j, in the solution vector. This will then give one value in the source vector for the given collocation point. I.e. for the first row, $i = 1$: $A_{11}f_1 + A_{12}f_2 + A_{13}f_3 + ... + A_{1n}f_n = F_1$

The solution vector is obtained by multiplying **F** with the inverted **A**-matrix, $f = FA^{-1}$, which in MATLAB is written on the form:

$$f = F\backslash A \tag{3.5.20}$$

The orthogonal collocation method is chosen due to its easy implementation and its sufficiently accurate results. However, a problem that may arise when using the orthogonal collocation method is the sensitivity to large values in the **A**-matrix. In this method the matrix should be central dominant, meaning the largest values ought to be on the diagonal of the matrix. If the equation includes large values for the derivatives, problems may arise as the derivatives fills the whole matrix and not only the diagonal. A central dominant matrix has a low condition number, which indicate that a perturbation in the input will give a small error in the output. For a ill-conditioned problem a perturbation in the input can lead to a large error in the output [43].

In addition to a well-conditioned matrix, the values in the **F**-vector should be smaller than, or with the same magnitude as the values on the diagonal of the **A**-matrix. For large values in the **F**-vector and small values on the diagonal of the **A**-matrix, important digits may be lost. By this the placement of the different parts of the equation solved should be done with great caution. When this is ensured, the orthogonal collocation method give solutions relatively easy.

3.5.1 Implementation

Due to the sensitivity of the **A**-matrix several options regarding the placement of the parts of the equations were tested.

Component Mass Balance

For the species mass balance in gas phase, the following was tested:

- The mass flux in the **F**-vector and all other parts in the **A**-matrix.
- A split component mass flux, where the gas phase part of the mass flux was placed in the **A**-matrix and the liquid part in the **F**-vector.
- For the total mass all the derivatives were written out.
- The total mass were expressed by the continuity and placed in **A**

In the gas phase there were some challenges in finding the most central dominant **A**-matrix. The most proper placement of the gas component balance was found to be the convection and the dispersion term in **A**, where the total mass was expressed by continuity. The component mass flux was divided into two parts, where the gas part was placed in **A** and the liquid part in **F**.

For the species mass balance in liquid phase, the placement of the equation was relatively easy compared to the gas phase, as the density in liquid phase is large and assumed constant, and results in larger values on the diagonal.

Placement of the terms in the liquid component balance:

- The convection and the dispersion term were placed in **A**.
- The mass flux was divided, where the liquid part was placed in **A** and the gas part in **F**.
- The reaction term was placed in the **F**-vector.

Due to small errors in the equations, the mass fractions are not summing to one. A solution to the problem one of the components in each phase is calculated by the other components.

In the gas phase the oxygen component was calculated as $1 - w_{CH_4} - w_{CO_2}$. This results in a small error in the oxygen-component. In the liquid phase the water-component is calculated from the other components. The mass fraction of

water is initially large, thus it is expected that the small error will have smaller effect on the water compound than for the oxygen in gas phase.

Temperature

The temperature equation for the liquid phase includes both heat transfer from the liquid to the gas and from the liquid to the surroundings. The advection- and conduction terms were placed in the **A**-matrix. Heat transfer from the liquid to gas was divided, where the liquid part was placed in **A** and the gas part was placed in **F**. The heat transfer from liquid to the walls, the term is included in **F**. In addition the reaction term is included in the **F**-vector.

For the gas phase the advective and conductive terms were placed in **A**. The heat transfer from the liquid to the gas was divided, where the gas part was included in **A** and the liquid part was placed in **F**.

In order to avoid fluctuations the solutions were under-relaxed by using a part of the new solution and a part of the previous solution.

Chapter 4

Results Single Cell Protein

In this section the results from the SCP bio-reactor simulations will be presented.

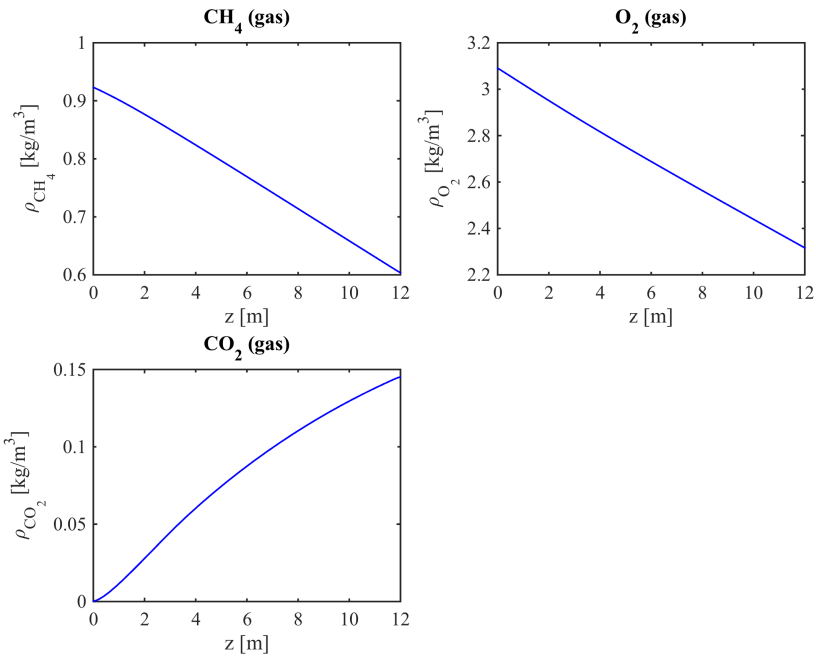

Figure 4.0.1: Change in gas densities for methane, oxygen, and carbon dioxide over the reactor length with the initial values based on the values by Taweel et al. [42] and Larsen [24].

When the gas bubbles rise in the tube it is expected that some of the reactants will dissolve in the water. The dissolved reactants will transfer to the bacteria,

the reaction will take place, and biomass, carbon dioxide and water is produced.

From Figure 4.0.1 it can be seen that the methane and oxygen densities in gas phase decrease as the gases dissolve. The methane and the oxygen densities in the gas phase does not approach zero over the reactor length. This is due to the mass transfer rate being too low for all the gas to dissolve. Due to a higher density of oxygen than methane, the driving force is larger. With oxygen having a higher solubility in water than methane, in addition to the larger driving force, result in more of the oxygen dissolving in the water.

The concentration of carbon dioxide is initially zero as can be seen from Figure 4.0.1. Over the reactor length the carbon dioxide gas density increases as the reaction occur in liquid phase and carbon dioxide transfers to the gas phase.

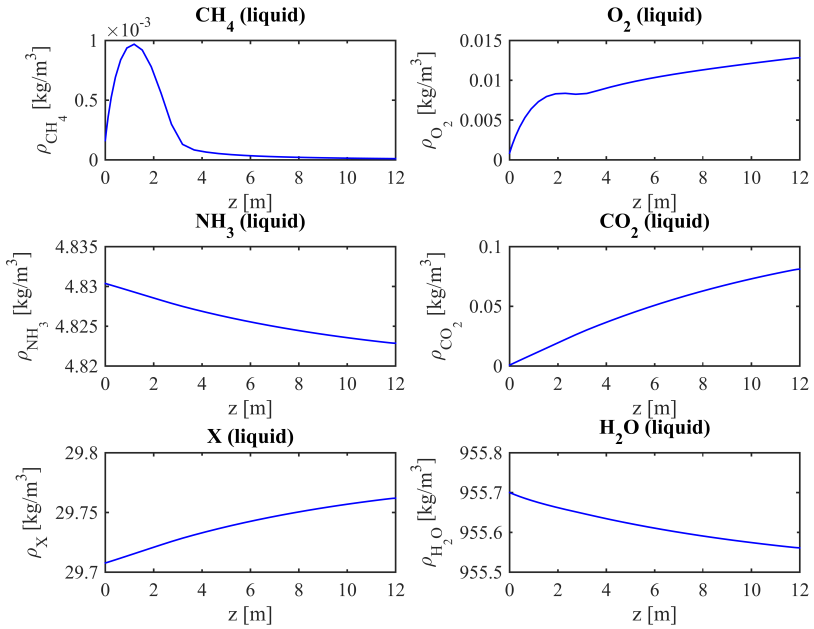

Figure 4.0.2: Change in liquid density of the components over the reactor length with the initial values based on the values by Taweel et al. [42] and Larsen [24].

From Figure 4.0.2 it can be seen that as the methane and oxygen dissolve in the liquid the concentration of the components increases. In the beginning of the column the methane concentration in liquid phase increases rapidly before it starts to decrease. The decrease is due to more methane being consumed than what dissolves. The ammonia concentration decreases as the reaction occurs. Regarding oxygen in liquid phase, more of the oxygen is dissolved in the liquid than what is consumed by the bacteria, and the concentration increases. From Figure 4.0.2 it can be seen that methane is the limiting component as the methane approaches zero in the top of the reactor, while the oxygen density increases. As the reaction take place, the concentration of biomass and carbon dioxide increases. Initially the liquid phase contains 3 wt% biomass, thus the biomass concentration is not zero initially. From Figure 4.0.2 the water is approximately constant over the column. The water component is calculated from the other components. When solving the equations small errors may arise. With the water being calculated as $1 - \sum_i w_{i,g}$, where $i \neq H_2O$, these small errors will be stored in the water mass fraction and result in an error in the component.

The mass fractions are given in appendix A.2.

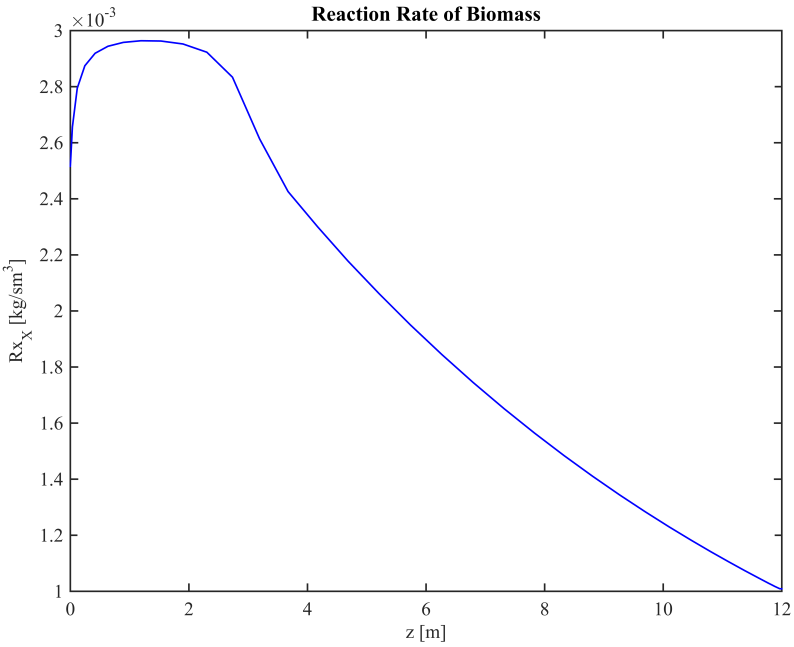

Figure 4.0.3: Reaction rate of biomass with the initial values based on the values by Taweel et al. [42] and Larsen [24].

As seen from Figure 4.0.3, at the reactor inlet, where the methane and oxygen densities are high, the reaction rate is at its highest. The reaction rate decreases with decreasing methane concentration along the reactor.

It is found that the biomass production is 2.45 kg/h. To increase the biomass production, methane could be fed into the reactor several places. In the process at Tjeldbergodden and in the U-loop operated by UniBio, the feed gas is introduced at several points along the column. Additional suggestions for how to introduce the feed gas is described in section 7

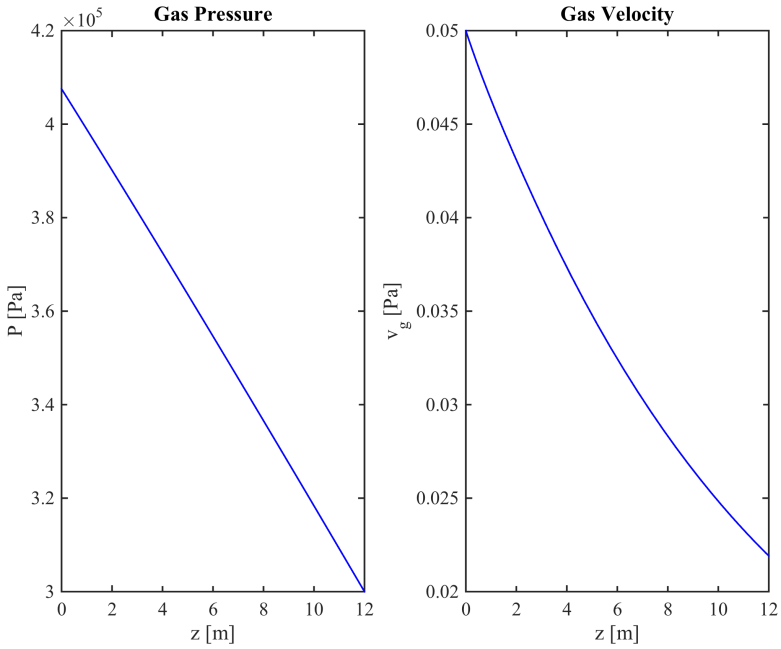

Figure 4.0.4: Gas pressure and velocity along the reactor length with the initial values based on the values by Taweel et al. [42] and Larsen [24].

The pressure decreases linearly with increasing height, as seen from Figure 4.0.4. With the gravitational force and the liquid density being assumed constant, in addition to the change in liquid hold-up being small, the pressure varies with the column height, seen from equation (3.1.1).

The gas velocity profile in Figure 4.0.4 shows that the superficial gas velocity decreases along the reactor. This is due to the change in gas density as the gas dissolves in the liquid. With the assumption of constant bubble size, the gas velocity decreases to over half of its initial value. This is a weakness in the model as the bubble size will change over the reactor length and thus affect the velocity.

In Figure 4.0.5 the gas and liquid temperatures are shown.

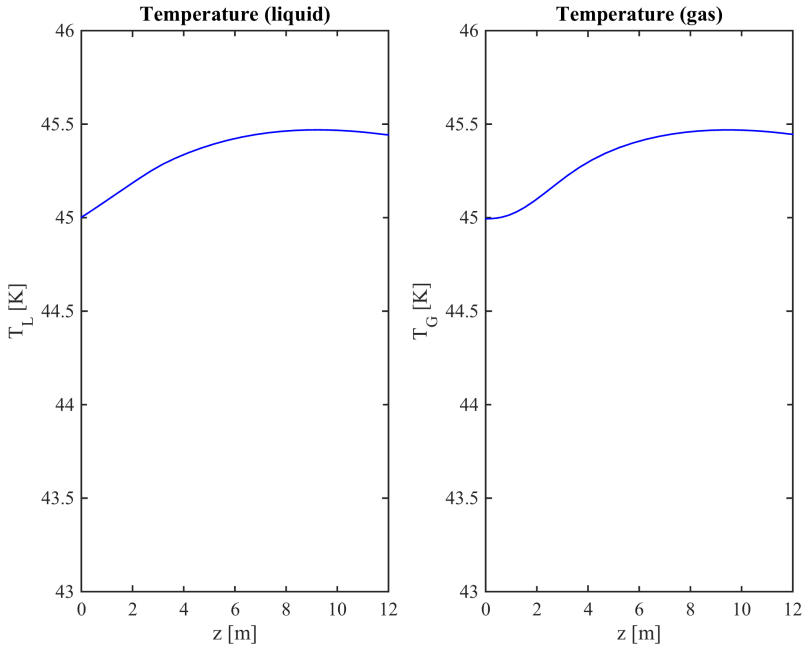

Figure 4.0.5: Temperature of the gas- and liquid phase in the reactor with the initial values based on the values by Taweel et al. [42] and Larsen [24].

As the heat exchange is efficient, the temperature is approximately constant for both the phases.

4.1 Optimization of the inlet values

To investigate the possibility for increased biomass production, the inlet value of methane and biomass, the superficial velocities and the bubble size have been adjusted.

4.1.1 Inlet Values of Methane and Oxygen

To investigate how the methane-oxygen ratios affects the reaction rate, the initial mass fractions of methane and oxygen have been adjusted. The profiles shown in this section is only a selection of the simulation results.

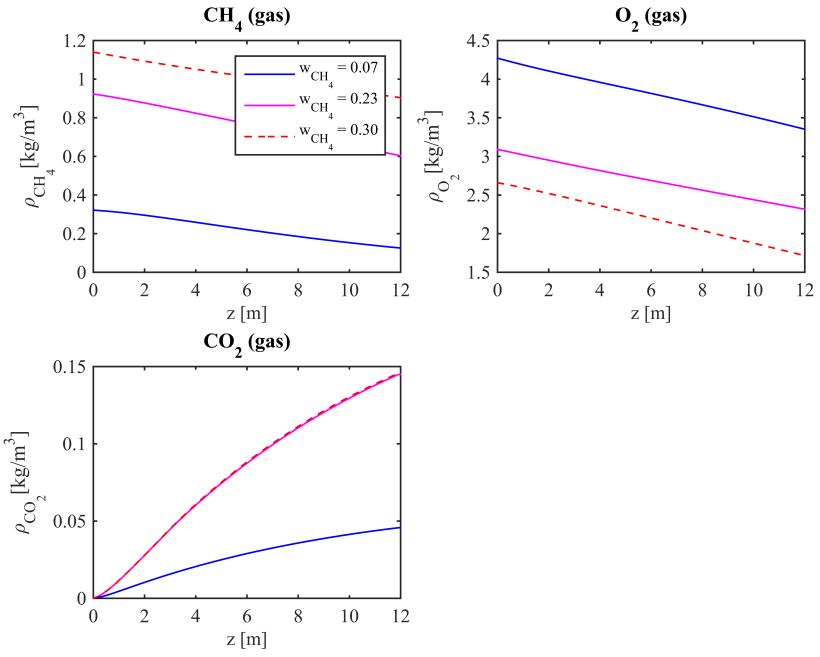

Figure 4.1.1: Gas densities for methane, oxygen and carbon dioxide with varying inlet methane fractions, $w_{CH_4} = 0.07$, $w_{CH_4} = 0.23$, $w_{CH_4} = 0.30$

A higher initial methane density results in the concentration differences between the gas and liquid phase being higher. This results in an increased driving force, seen from Figure 4.1.1. With more methane and oxygen transferred, more carbon dioxide is produced in the liquid and transferred to the gas phase. When increasing the mass fraction of methane from 0.23 to 0.30 the production of carbon dioxide does not increase, seen from Figure 4.1.1. To explain this trend it is necessary to investigate the liquid component densities, shown in Figure 4.1.2.

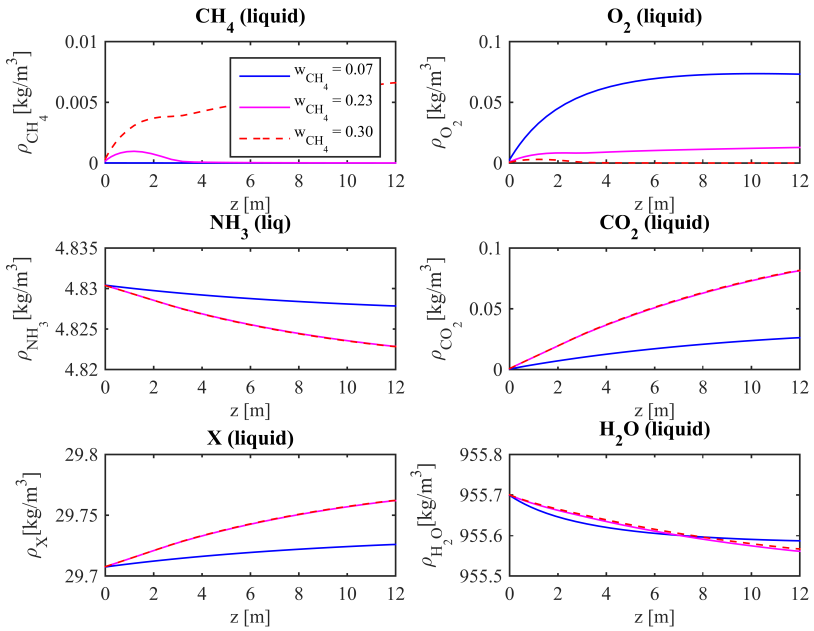

Figure 4.1.2: Component liquid densities with varying inlet methane fractions, $w_{CH_4} = 0.07$, $w_{CH_4} = 0.23$, $w_{CH_4} = 0.30$

Figure 4.1.2 shows that when increasing the inlet mass fraction of methane, the biomass density increases due to more available substrate. For $w_{CH_4} = 0.07$, there will be less substrate available and the biomass concentration is lowered. When $w_{CH_4} = 0.30$ the density of methane is increased such that

oxygen limits the reaction. This can be seen from the large increase in methane concentration and the low oxygen concentration in Figure 4.1.2. The biomass density is approximately the same when $w_{CH_4} = 0.23$ and $w_{CH_4} = 0.30$.

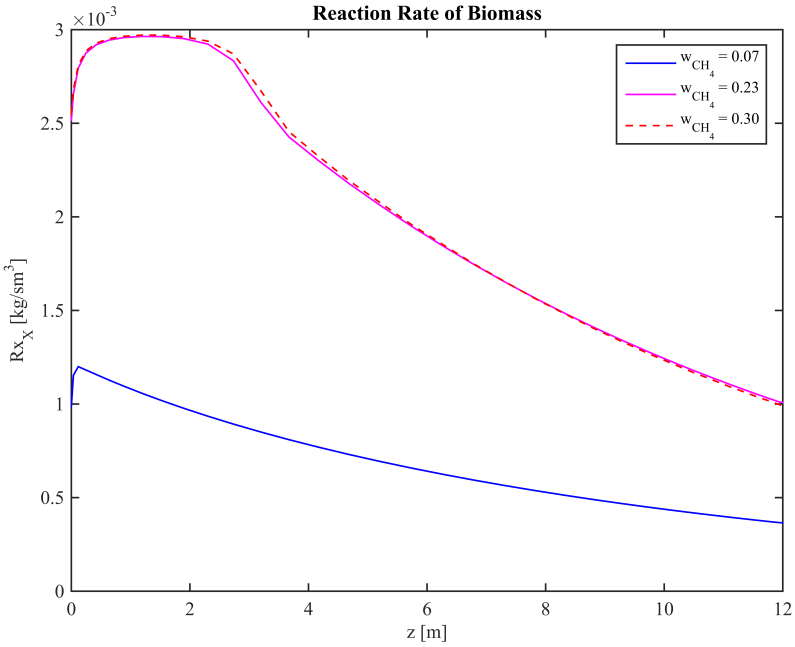

Figure 4.1.3: Reaction rate of biomass with varying inlet methane fractions, $w_{CH_4} = 0.07$, $w_{CH_4} = 0.23$, $w_{CH_4} = 0.30$

Figure 4.1.3 shows that in the beginning of the reactor, where the methane concentration is at its highest, the reaction rate is at its maximum. From 3.2.11 both the methane and oxygen densities are included in the reaction kinetics. This means that an optimal feed results in both the methane and oxygen being limiting substrates. In table 4.1.1 the biomass flow in the top of the reactor is listed for five methane inlet values, showing that the ideal inlet mass fraction is $w_{CH_4} = 0.26$.

Table 4.1.1: Bioproduction with five methane inlet values.

Parameter	Mass Fraction	$w_{L,X}$ [kg_X/h]
w_{g,CH_4}	0.07	0.82
w_{g,CH_4}	0.18	1.99
w_{g,CH_4}	0.23	2.45
w_{g,CH_4}	0.26	2.68
w_{g,CH_4}	0.30	2.46

4.1.2 Superficial Gas Velocity

A selection of the simulation results are showed in the profiles with varying superficial gas velocity.

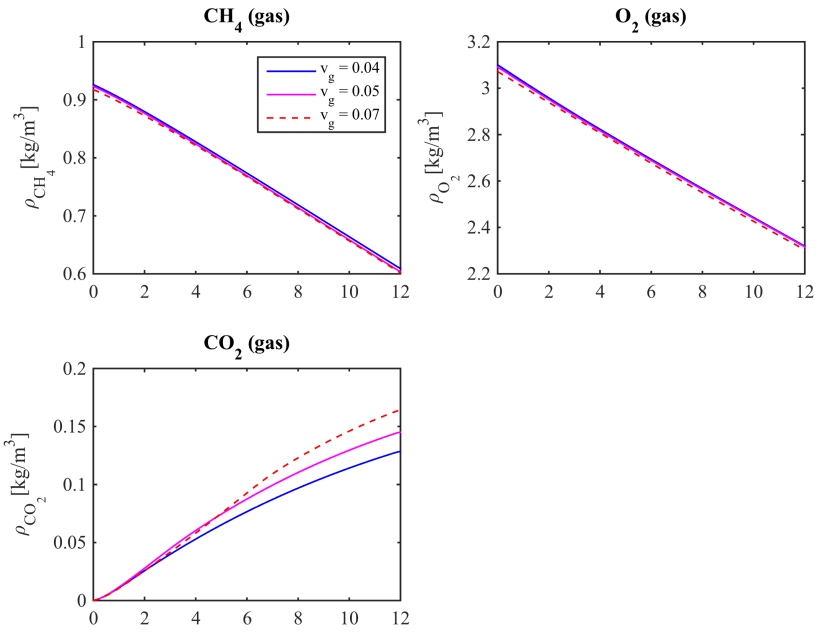

Figure 4.1.4: Component gas densities with varying superficial gas velocity, $v_g = 0.04$, $v_g = 0.07$, $v_g = 0.1$.

The liquid- and gas hold-up is given by equation (3.1.7). When increasing the superficial gas velocity more gas will be introduced to the system, resulting in a larger driving force, thus it is expected that more gas is dissolved over the reactor length. Figure 4.1.4 shows that an increase in the gas velocity from $v_g^s = 0.04$ to $v_g^s = 0.07$ will give a slight increase in the transferred reactants. This is shown in the density of carbon dioxide in Figure 4.1.4, where the density is the highest when $v_g^s = 0.07$.

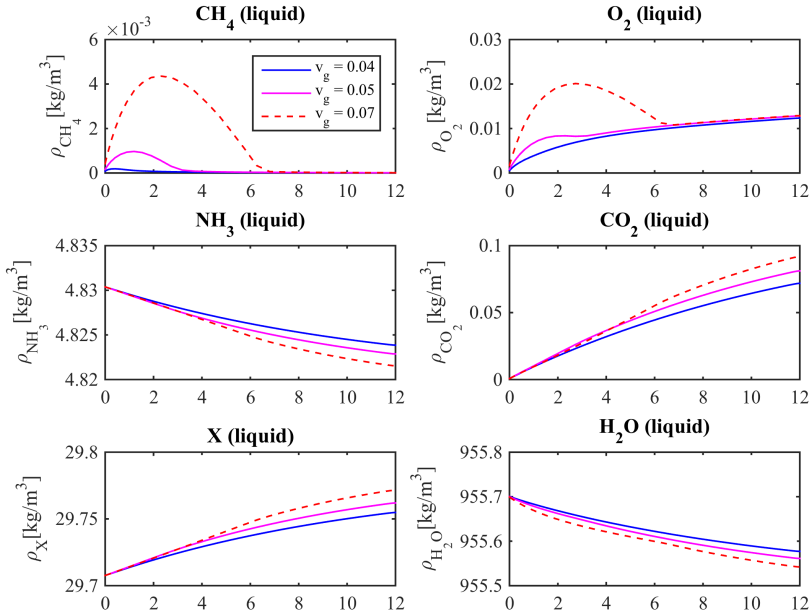

Figure 4.1.5: Component liquid density with varying superficial gas velocity, $v_g = 0.04$, $v_g = 0.07$, $v_g = 0.1$.

With more gas dissolved, the methane and oxygen densities in liquid phase is increased. Over the reactor, approximately all the methane is consumed by the bacteria and the methane density approaches zero. With methane being the limiting substrate the oxygen concentration approaches the same value for all the gas velocities when the methane concentration is approximately zero. The effect of changing the superficial gas velocity on the biomass reaction rate is shown in Figure 4.1.6.

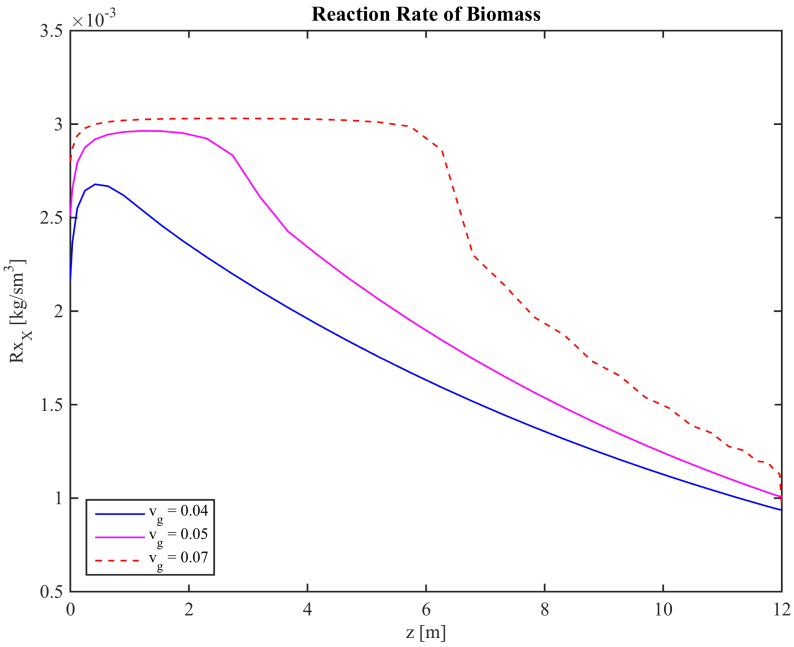

Figure 4.1.6: Reaction rate of biomass with varying superficial gas velocity, v_g = 0.04, v_g = 0.07, v_g = 0.1.

For higher superficial gas velocities, the reaction rate will stay high further up in the column. With $v_g^s = 0.07$ initially, the superficial gas velocity profile seems to be divided into two regions, seen from Figure 4.1.6. In the first part of the column, 0-6 m, the reaction rate is approximately constant. This means that between 0-6 m, the reaction is limited by the cell loading. After 6 m, the reaction rate decreases. From Figure 4.1.5 the methane density approaches zero at this position. Limited access to methane results in the reaction rate dropping, and the reaction is said to be limited by the mass transfer. When $v_g^s = 0.04$ the low concentration of dissolved methane gives a decrease in the biomass reaction rate after approximately 1 m.

In table 4.1.2 the percentage biomass increase and the biomass production flow are given, where it is seen that the superficial gas velocity giving the highest

outlet biomass flow is $v_g^s = 0.07$.

Table 4.1.2: Change in biomass production, and gas- and liquid hold-up with varying superficial gas velocity, $v_g = 0.04$, $v_g = 0.07$, $v_g = 0.1$.

Parameter	Fraction [−]	$w_{L,X}$ [kg_X/h]	ϵ_l [−]	ϵ_g [−]
v_g^s	0.03	1.40	0.93	0.07
v_g^s	0.05	1.98	0.89	0.11
v_g^s	0.07	2.44	0.85	0.15
v_g^s	0.08	3.02	0.83	0.17

Even though it is desired to increase the superficial gas velocity, there are physical factor that needs to be taken into account. When increasing the gas velocity larger bubbles will be formed due to coalescence. It is difficult to avoid coalescence in a system with higher velocities. An increase in the bubble size is undesirable as larger bubbles will give a lower contact area. If increasing inlet superficial gas velocity, undesirable challenges that may arise, such as slugging, needs to be taken into consideration.

4.1.3 Superficial Liquid Velocity

Varying the superficial liquid velocity will affect the gas hold-up.

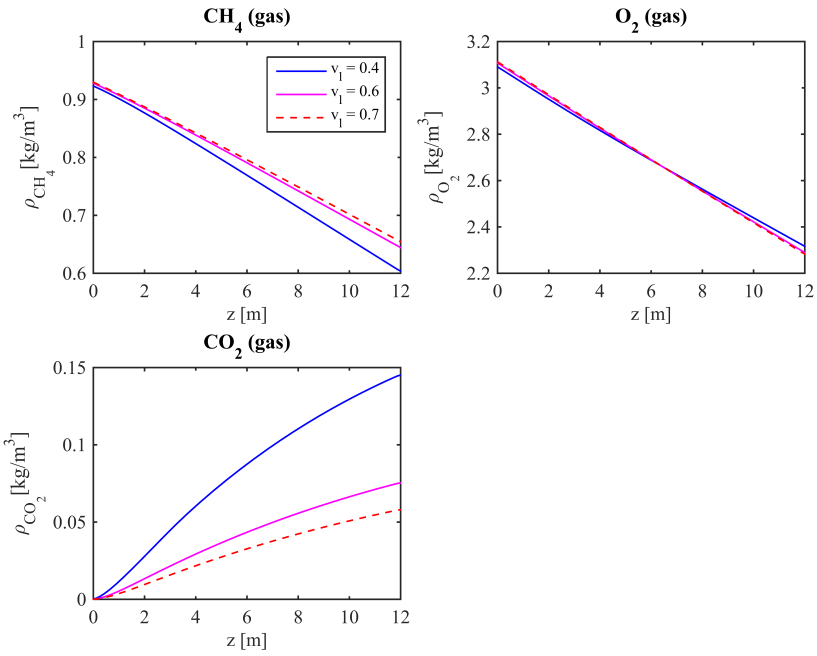

Figure 4.1.7: Component gas densities over the tube with varying liquid velocity, $v_l = 0.4$, $v_l = 0.6$, $v_l = 0.7$

It is expected that the mass transfer of methane and oxygen will be higher for lower superficial liquid velocities, as this will result in a higher gas hold-up. From Figure 4.1.7 it can be seen that for lower superficial liquid velocities the transfer of methane is increased. The gas density profile for oxygen shows the opposite trend compared to that of methane. For the oxygen in gas phase the profile shows that more of the component is transferred for higher superficial liquid velocities. The explanation is that the mass fraction of oxygen is calculated as $1 - \sum_k w_{g,k}$, where $k \neq O_2$. When the oxygen component is calculated out of the other component, the small errors from the equations are gathered in the

mass fraction of oxygen.

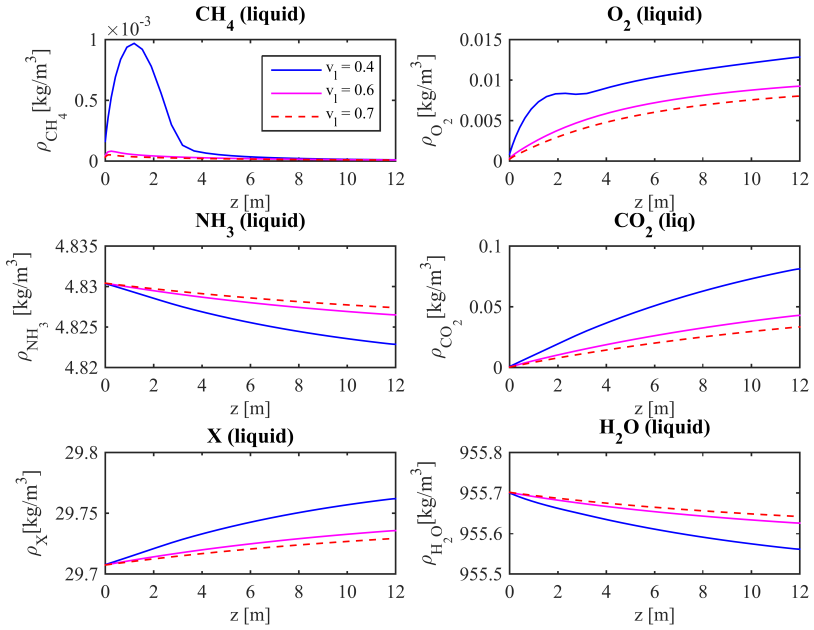

Figure 4.1.8: Component liquid densities with varying liquid velocity, $v_l = 0.4$, $v_l = 0.6$, $v_l = 0.7$

With more substrates present it is expected that more ammonia is consumed, and that the biomass and carbon dioxide concentration is increased. From the component liquid densities shown in Figure 4.1.8, it can be seen that more methane and oxygen is dissolved for the lowest velocities. In the liquid phase the small errors are gathered in the water component, as described earlier. The expected effect of the increased gas hold-up is shown for the liquid oxygen concentration, which is higher for lower liquid velocities.

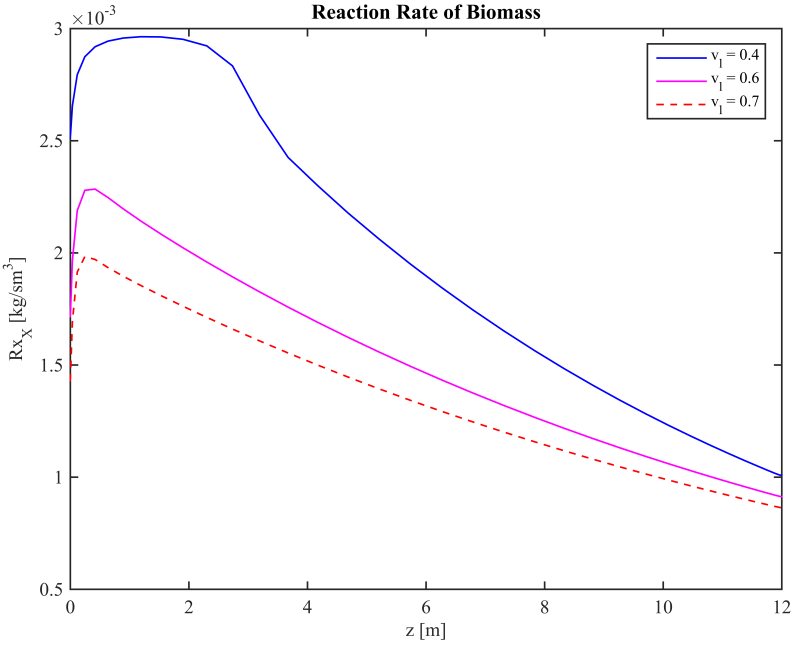

Figure 4.1.9: Reaction rate of biomass with varying liquid velocity, $v_l = 0.4$, $v_l = 0.6$, $v_l = 0.7$

More methane and oxygen is available for lower liquid velocities, and the biomass production is the highest for $v_L = 0.4$, as seen in Figure 4.1.8. The temperature and pressure is approximately independent for different superficial liquid velocities and is approximately equal to the temperature and pressure profiles given in Figure 4.0.5 and Figure 4.0.4, respectively. These profiles have therefore not been included.

In table 4.1.3 the effect on the biomass production, the gas- and liquid hold-up, and the Reynolds number is given, where it is given that the biomass production on an hourly basis is increased with decreasing superficial liquid velocity.

Table 4.1.3: Change in biomass production, gas- and liquid hold-up, and Reynolds number with varying liquid velocity, $v_l = 0.4$, $v_l = 0.6$, $v_l = 0.7$

Parameter	Fraction [−]	$w_{L,X}$ [kg_X/h]	ϵ_l [−]	ϵ_g [−]	$Re \cdot 10^{-5}$ [−]
v_l	0.4	2.45	0.889	0.111	1.33
v_l	0.6	1.28	0.923	0.077	1.99
v_l	0.7	0.98	0.933	0.067	2.33

Based on the simulations, the superficial liquid velocity giving the highest biomass flow in the outlet is $v_l^s = 0.4$.

There are additional restrictions that needs to be taken into account when changing the liquid velocity. In order to sustain a turbulent flow the Reynolds number needs to be high enough. From table 4.1.3 it can be seen that the Reynolds numbers are in an acceptable interval for all the superficial liquid.

4.1.4 Inlet Values Biomass

It is by now found that SCP production is mass transfer limited. However, it is of interest to investigate the effect on the biomass production when increasing the concentration of bacteria present.

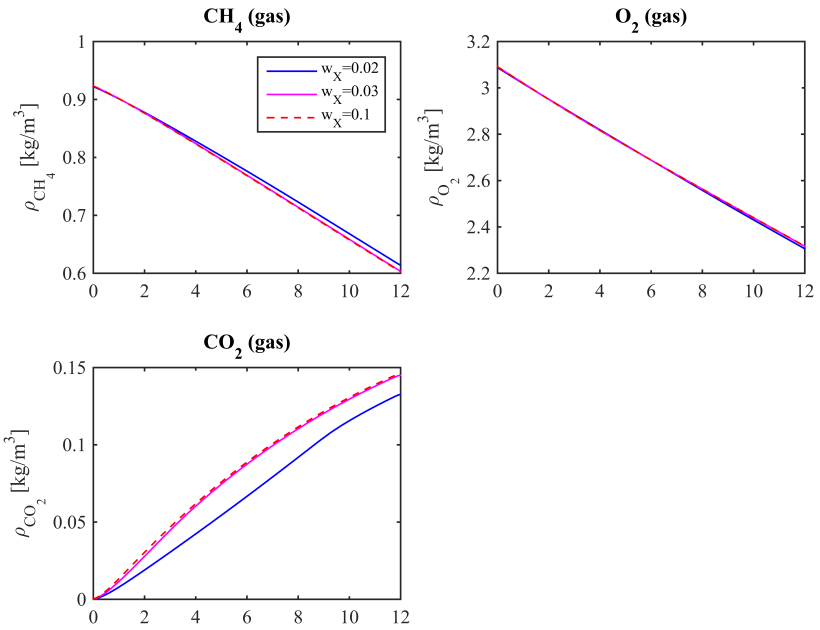

Figure 4.1.10: Component gas densities with various inlet biomass, $w_X = 0.02$, $w_X = 0.04$, $w_X = 0.1$

It is expected that the increased inlet biomass will not affect the reactants in gas phase, as the bacteria are only present in the liquid phase. Figure 4.1.10 shows that the mass transfer from gas to liquid phase is not affected by the increased initial biomass density. A hypothesis was that when the cell concentration is increased the dissolved gas is consumed faster, thus the driving force will increase due to the low methane and oxygen concentration in liquid phase. However, based on Figure 4.1.10 this seems not to be the case.

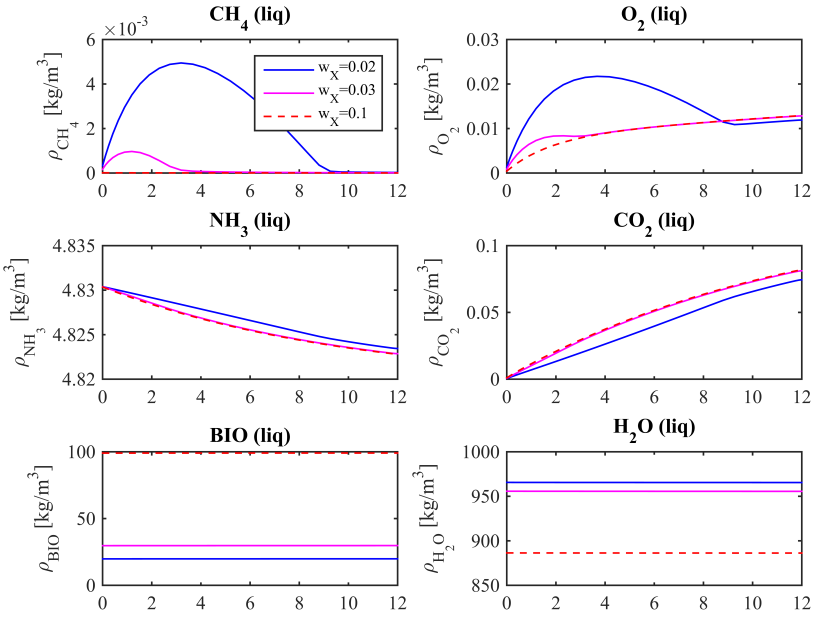

Figure 4.1.11: Liquid component densities with various inlet biomass, $w_X = 0.02$, $w_X = 0.04$, $w_X = 0.1$

Increasing the cell loading will result in more bacteria present to utilize the substrate. From the previous liquid density profiles it has been seen that in the beginning of the column, the reaction kinetics limited the production. Increasing the initial biomass density, it is expected that this increase in the methane density in the beginning of the column will diminish. From Figure 4.1.11 it can be seen that when increasing the initial cell loading to $w_X = 0.1$, the methane is utilized very rapidly. When the cell loading is decreased to $w_X = 0.02$, the kinetics is limiting the biomass production, and the methane concentration is high. Correspondingly, the oxygen concentration is the highest for $w_X = 0.02$.

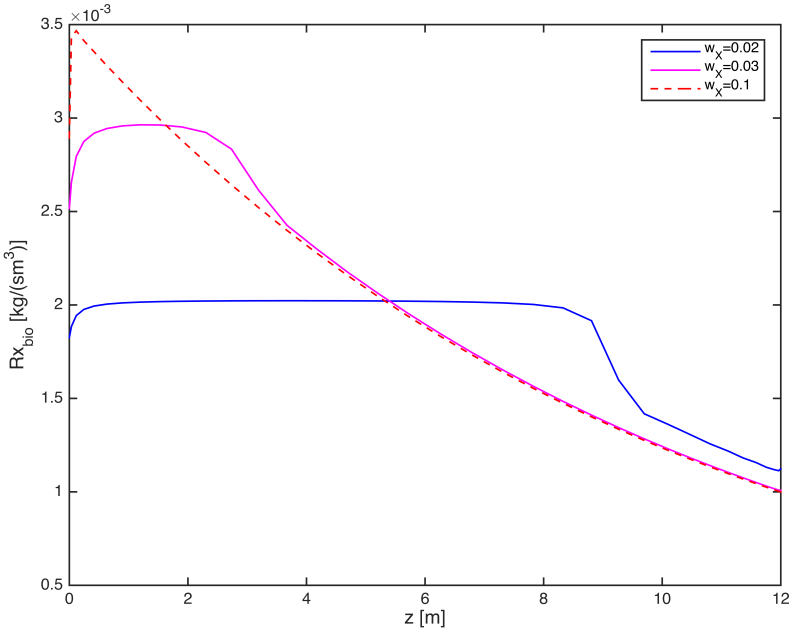

Figure 4.1.12: Reaction rate of biomass with various inlet biomass, $w_X = 0.02$, $w_X = 0.04$, $w_X = 0.1$

Figure 4.1.12 shows that when increasing the initial biomass there is an increase in the reaction rate. Figure 4.1.11 showing the biomass concentration is misleading as there seems to be no increase in biomass over the reactor length. This is only due to the scaling of the axis in the figure. The biomass reaction rate when $w_X = 0.02$ is approximately constant over the first 9 m. This is due to the kinetics limiting the production, as described above. After 9 m the production is limited by mass transfer, and the reaction rate drops. The biomass flow out of the tube for various initial biomass concentrations is presented in table 4.1.4. Table 4.1.4 shows that for an increase in the initial biomass, the overall production is approximately equal. This can be explained by the mass transfer limitations in the system.

Table 4.1.4: Change in biomass production with various inlet biomass, $w_X = 0.02$, $w_X = 0.04$, $w_X = 0.1$

Parameter	Fraction	$w_{L,bio}$ [kg_X/h]
$w_{l,BIO}$	0.02	2.45
$w_{l,BIO}$	0.04	2.46
$w_{l,BIO}$	0.10	2.46

If the concentration of bacteria is too high the bacteria might start to flocculate and hindering mass transfer, as discussed in section 2.1.1. This is an additional factor that needs to be taken into account before considering increasing the cell loading.

4.1.5 Reduced Bubble Size

The bubble size is one of the variables affecting the mass transfer. With the process being limited by mass transfer, it is desired to investigate the effect on the biomass production when changing the bubble size.

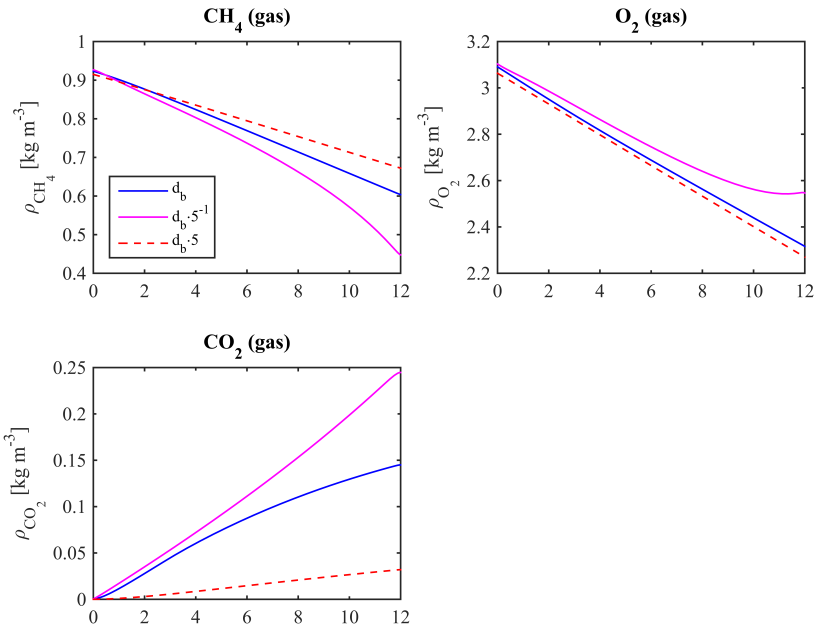

Figure 4.1.13: Component gas densities with different average bubble diameter, $d_b = 2$, $d_b = 2/5$, $d_b = 2\dot{5}$

It is expected that more methane and oxygen is transferred with reduced bubble size due to increased contact area and thus increased mass flux. From Figure 4.1.13 the methane transferred is the highest with the reduced bubble size. The oxygen gas density profile shows the opposite trend as that for methane. As described when discussion Figure 4.1.7, this trend is due to the error gathered in the oxygen component in gas phase. If not limited by the kinetics, it is to expect that the carbon dioxide concentration in gas phase will increase with increased

transfer of the substrates. This can seen from Figure 4.1.13, where the largest carbon dioxide concentration is obtained for a reduced average bubble size.

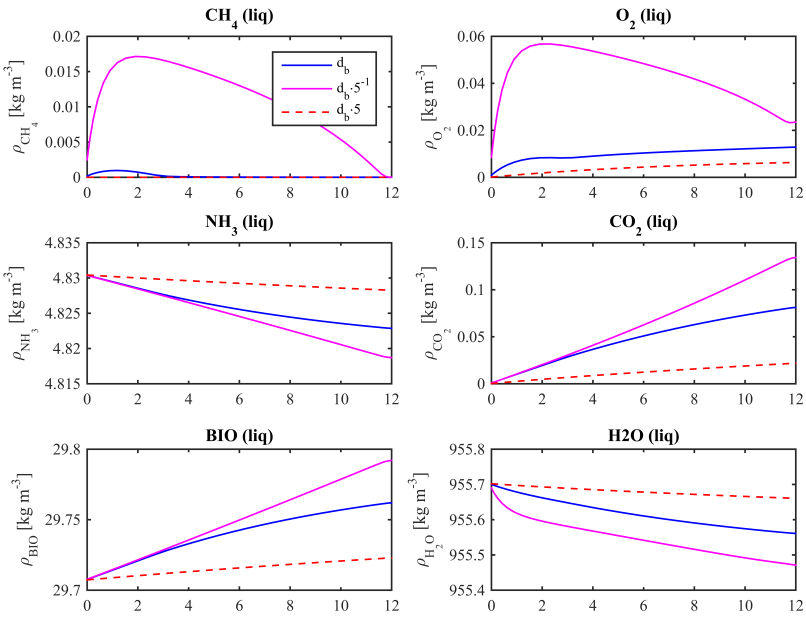

Figure 4.1.14: Change in liquid densities with different average bubble diameter, $d_b = 2$, $d_b = 2/5$, $d_b = 2\dot{5}$

The expected increase in dissolved methane and oxygen for a reduced bubble size is shown in Figure 4.1.14. With an increased mass flux more of the gas is transferred to the liquid phase. As described earlier, the process is limited by the transfer of methane. When increasing the mass flux, the methane is no longer fully utilized over the reactor length, seen from Figure 4.1.14. This means that the process is no longer limited by the mass transfer, but the reaction kinetics. If increasing the bubble size the mass flux is decreased, and the concentration of biomass and carbon dioxide is lowered.

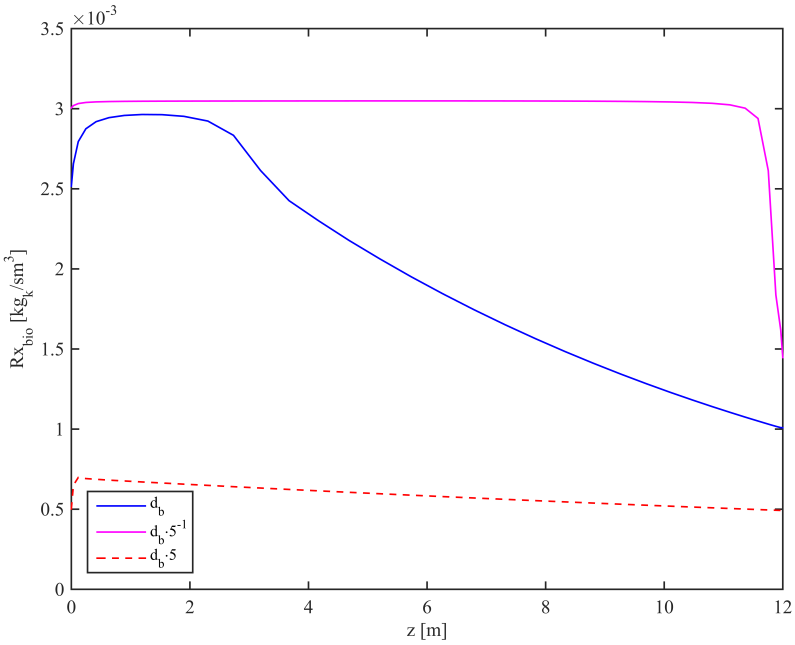

Figure 4.1.15: Change in reaction rate of biomass with different average bubble diameter, $d_b = 2$, $d_b = 2/5$, $d_b = 2\dot{5}$

For a high substrate concentration, the biomass reaction rate stay high over the reactor, seen from Figure 4.1.15, and the process is limited by the kinetics. The low substrate concentration with increased bubble diameter results in the biomass reacting rate staying low. In table 4.1.5 the biomass production with varying bubble size is given, showing that the decrease in bubble size gives a significantly higher biomass production.

Table 4.1.5: Biomass produced with different average bubble diameter, $d_b = 2$, $d_b = 2/5$, $d_b = 2\dot{5}$

Parameter	$w_{L,bio}$ [kg_X/h]
d_b	2.45
$d_b \cdot 5^{-1}$	3.81
$d_b \cdot 5$	0.70

4.2 Mass Transfer Coefficient

In order to obtain an accurate prediction of the mass transfer, it is of interest to investigate the sensitivity to the choice of correlation for the mass transfer coefficient. Depending on the surfactants present, there are three different systems of interest; clean-, partly contaminated-, and contaminated systems. The correlations included are those presented in table 2.1.1 in section 2.1.2.

Clean System

For a clean system four different correlations for the mass transfer coefficient are implemented.

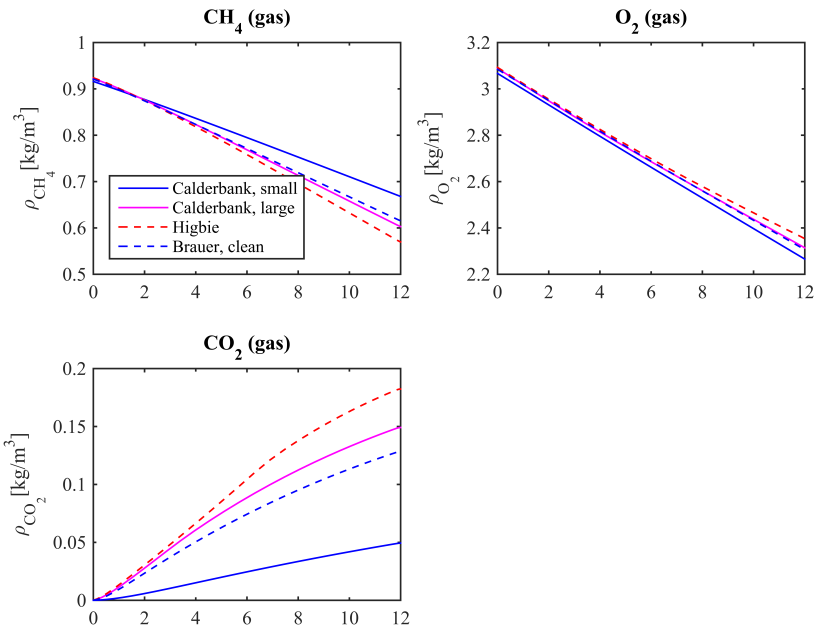

Figure 4.2.1: Gas density for the components for a clean system with use of different mass transfer coefficients.

Figure 4.2.1 shows that there are deviations in the components transferred with use of different correlations. The coefficient proposed by Higbie [20] gives the largest mass transfer, whereas the coefficient by Calderbank et al. [9] for small bubbles gives the lowest. As discussed earlier, the error is gathered in the oxygen component in gas phase. It is assumed that that the shift in trend for the coefficients is caused by this calculation of the oxygen component. With more substrate transferred to the liquid phase the carbon dioxide concentration in gas phase increases.

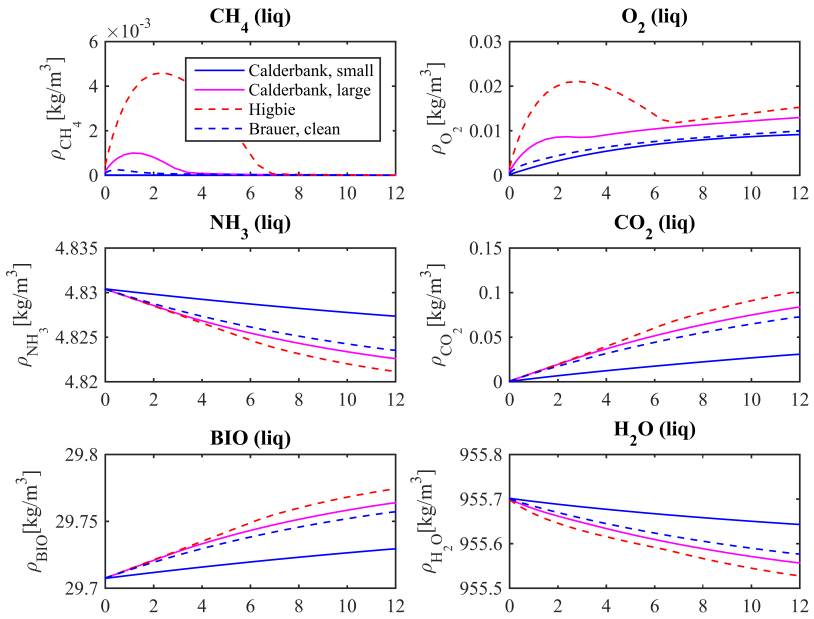

Figure 4.2.2: Liquid density of the components for a clean system with use of different mass transfer coefficients.

From Figure 4.2.2 the small error is gathered in the water component and not in the oxygen, and result in the correlation by Higbie [20] giving the largest mass transfer of oxygen. With use of the coefficient by Higbie [20], the methane concentration is higher in the beginning than what the bacteria can consume.

Coefficients by Brauer [7] and Calderbank et al. [9] for large bubbles gives a low mass flux, thus the mass transfer is limiting the production after approximately 2 and 3 m, respectively. The oxygen concentration can be seen to be approximately equal with the coefficient by Calderbank et al. [9] for small bubbles and Brauer [7]. With small amount of methane dissolved with the coefficient proposed by Calderbank et al. [9] for small bubbles, the biomass production is low. Over the reactor length the methane is approximately fully utilized for all the correlations.

The effect of the different correlations on the reaction rate of biomass is shown in Figure 4.2.3.

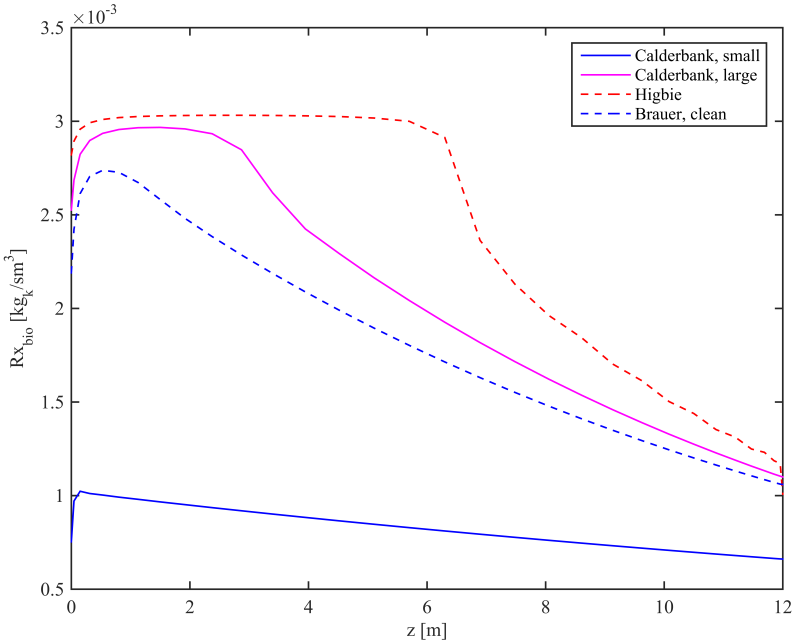

Figure 4.2.3: Reaction rate of biomass for a clean system with use of different mass transfer coefficients.

With the use of correlation by Calderbank et al. [9] on large bubbles and Higbie

[20], the biomass production is limited by kinetics for the first 3 and 6 m respectively, before the mass transfer starts to limit the process. Use of the mass transfer coefficients by Brauer [7] and Calderbank et al. [9] on small bubbles, results in the process being mass transfer limited almost immediately. It should be noted that even though the methane concentration is very low, shown in Figure 4.2.2, there is still production of biomass. In table 6.5.1 the biomass production on an hourly basis is given, and it can be seen that the choice of mass transfer coefficient strongly affects the production.

Table 4.2.1: Biomass production for a clean system with use of different mass transfer coefficients.

System	Mass Transfer Coefficient	$w_{L,X}$ [kg·X/h]
Clean	Calderbank, small	1.00
Clean	Calderbank, large	2.54
Clean	Higbie	3.01
Clean	Brauer	2.24

Partly Contaminated System

In the SCP process the fermentation broth contains salt and minerals. The system will therefore most likely be a partly contaminated or a contaminated system.

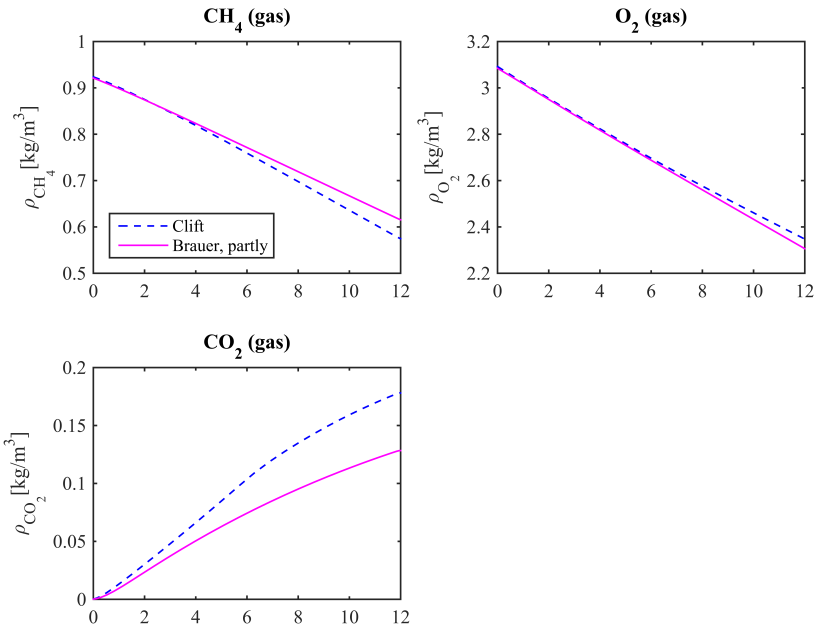

Figure 4.2.4: Component gas densities in gas phase for a partly contaminated system with use of different mass transfer coefficients.

Figure 4.2.4 shows that the mass transfer of methane is highest with the use of the expression by Clift et al. [10]. More carbon dioxide is transferred to the gas phase with use of the coefficient by Clift et al. [10], as more substrate will be available in the liquid phase. The shift in the correlations for the oxygen component is explained earlier.

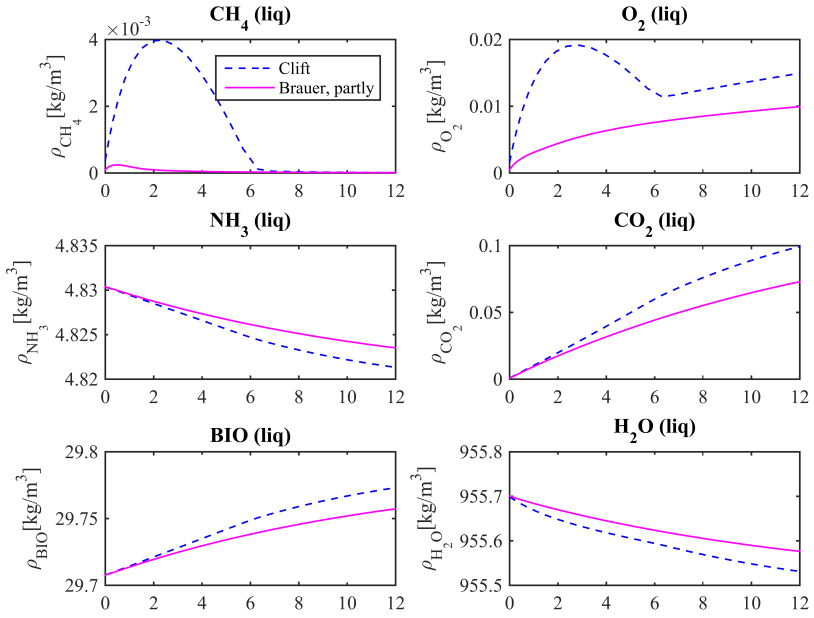

Figure 4.2.5: Liquid component densities for a partly contaminated system with use of different mass transfer coefficients.

The coefficient suggested by Clift et al. [10] gives the highest concentration of methane and oxygen, shown in Figure 4.2.5. Therefore, with the process being limited by methane dissolved, the biomass concentration is the highest with use of this correlation. The difference in biomass concentration for the two coefficients is small, however significant regarding the overall production.

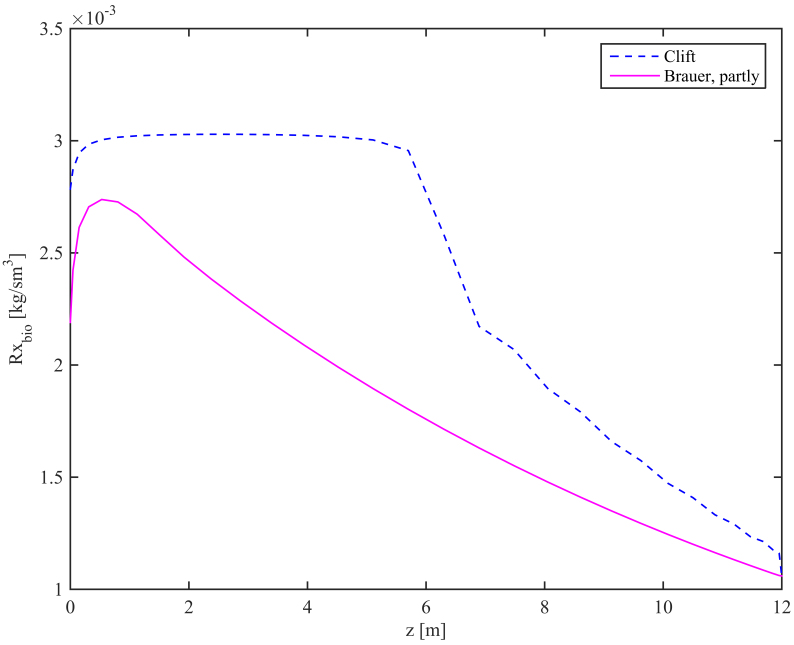

Figure 4.2.6: Reaction rate of biomass for a partly contaminated system with use of different mass transfer coefficients.

The reaction rate of biomass is higher with the expression by Clift et al. [10] compared to that by Brauer [7] due to the substrate concentration in liquid phase. From Figure 4.2.6 it can be seen that the mass transfer limit the production after approximately 7 m, with coefficient by Clift et al. [10]. The biomass flow rates are given in table 4.2.2, showing that choosing one coefficient over the other could potentially under/over estimate the bio-production.

Table 4.2.2: Biomass production in a partly contaminated system with use of different mass transfer coefficients.

System	Mass Transfer Coefficient	$w_{L,X}$ [kg_X/h]
Partly Contaminated	Clift	2.85
Partly Contaminated	Brauer	2.17

Contaminated System

Four different correlations for the mass transfer coefficient for a contaminated system have been included in the simulations.

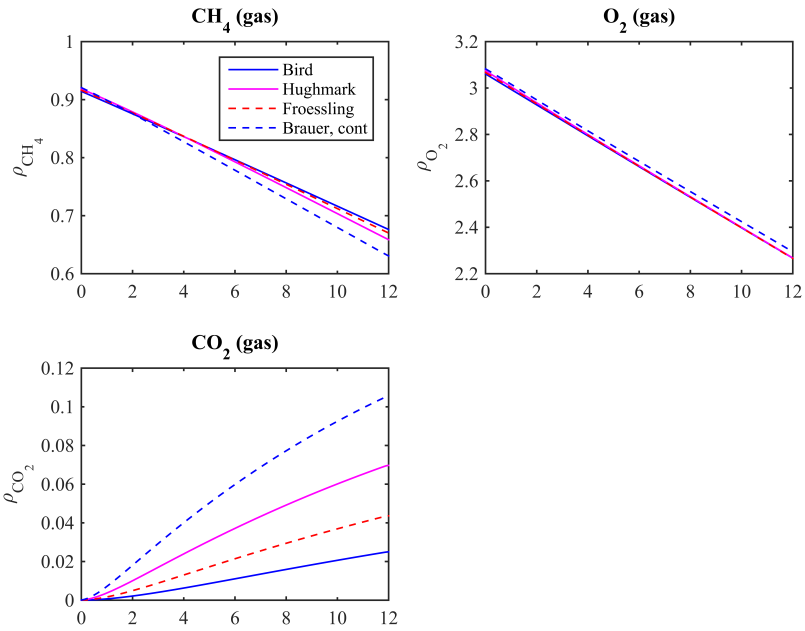

Figure 4.2.7: Component gas densities with different correlations for the mass transfer coefficient for a contaminated system.

It can be seen from Figure 4.2.7 that the methane transfer from gas to liquid phase is highest with use of the correlation by Brauer [7]. The other correlations shows a very similar mass transfer of methane. Regarding the oxygen density profile, it is approximately the same for all the correlations. The carbon dioxide concentration in gas phase is the highest for Brauer [7] due to more methane dissolved.

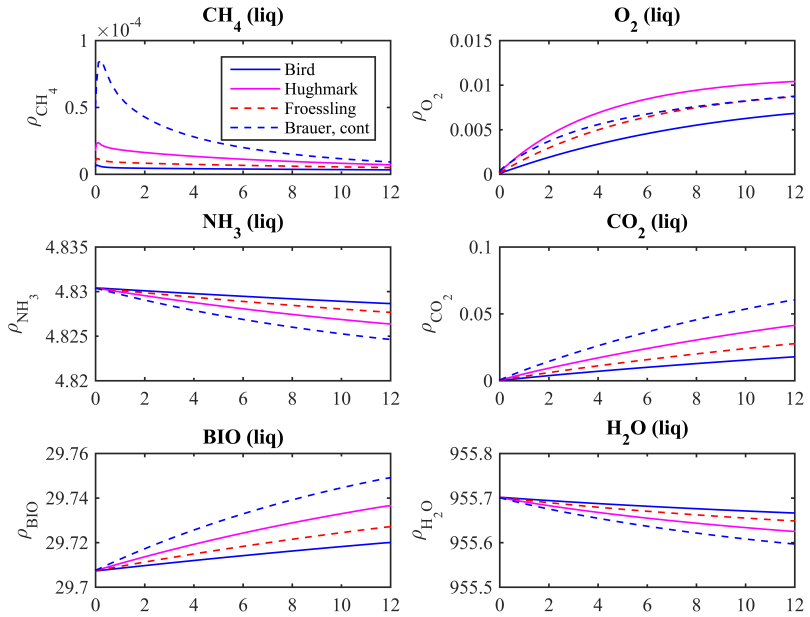

Figure 4.2.8: Component liquid densities with different correlations for the mass transfer coefficient for a contaminated system.

For a contaminated system, the highest concentration of dissolved methane is obtained with used of the coefficient by Brauer [7], seen in Figure 4.2.8. Thus the coefficients by Brauer [7] results in the highest production biomass and carbon dioxide. The methane has not been fully utilized with either of the correlations, however the concentrations are low. Regarding the oxygen component in liquid phase, this shows that Hughmark [21] gives the largest oxygen concentration.

Based on the trends for the clean and contaminated system, where the coefficient giving the highest mass transfer of methane also gives the highest mass transfer of oxygen, this is a deviation.

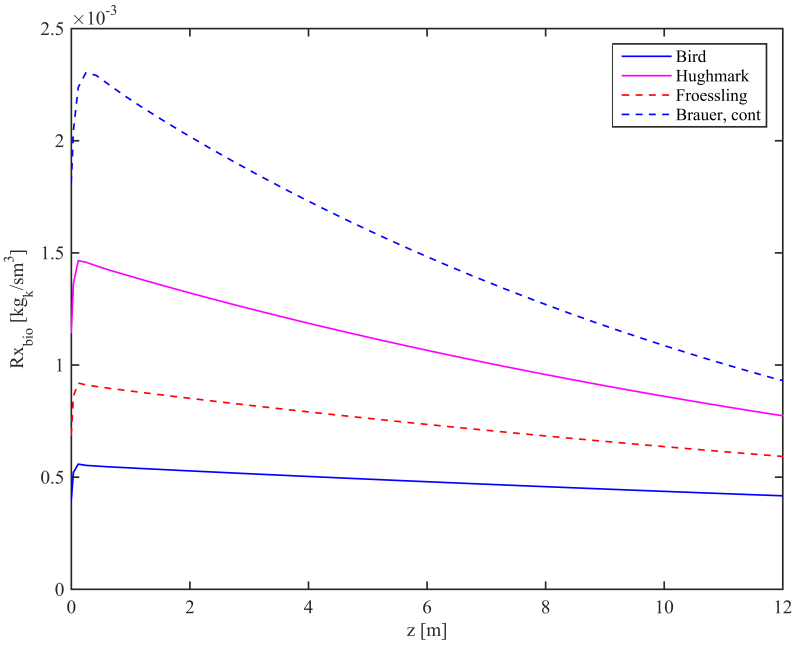

Figure 4.2.9: Reaction rate of biomass with use of different mass transfer coefficients for a contaminated system.

In Figure 4.2.9 there are deviations in the biomass reaction rate due to the varying substrate concentrations. Notice that the highest value for the reaction rate for Bird et al. [3] is lower than the lowest value for the reaction rate by Brauer [7]. This clearly affects the biomass production given in table 4.2.3, where the production is over three times higher with use of the correlation by Brauer [7] as that by Bird et al. [3].

Table 4.2.3: Biomass production with use of different mass transfer coefficients for a contaminated system.

System	Mass Transfer Coefficient	$w_{L,X}$ [kg_X/h]
Contaminated	Bird	0.58
Contaminated	Hughmark	1.31
Contaminated	Fröessling	0.89
Contaminated	Brauer	1.88

Coefficient for Turbulent Flow

Mass transfer coefficients for turbulent flow have been implemented in the SCP reactor model, when it has been assumed that the turbulence is caused by wall friction. The profiles for the gas- and liquid densities, and the biomass reaction rate are given in appendix A.2.

From the reactor simulations it was found that the mass transfer with use of the coefficient when small eddies dominates the surface renewal, gave significantly higher mass transfer. With much higher substrate concentrations available for the bacteria, the coefficient for the small eddies gave a larger biomass production, given in table **??**.

Table 4.2.4: Biomass production with varying mass transfer coefficients for turbulent flow.

Turbulence by	Mass Transfer Coefficient	$w_{L,X}$ [kg_X/h]
Wall friction	$k_{L,small}$	2.400
Wall friction	$k_{L,large}$	0.560

Based on the large differences in mass transferred for the assumption of the small or large eddy domination, knowledge about the domination is needed in order to choose the most proper coefficient. It should be noted that there are coefficients in the literature that takes into account the surface renewal by both small and large eddies. A correlation when both eddy types are taken into account is proposed by Han et al. [17].

Choice of Mass Transfer Coefficient

For each of the water systems the highest and lowest percentage biomass production for each system is given in table 4.2.5.

Table 4.2.5: Highest and lowest biomass production obtained with use of different mass transfer coefficients for a clean, partly contaminated, and contaminated system.

Production	System	Mass Transfer Coefficient	$w_{L,X}$ [kg_X/h]
High	Clean	Higbie	3.01
High	Partly Contaminated	Clift	2.85
High	Contaminated	Brauer	1.88
Low	Clean	Calderbank, small	0.996
Low	Partly Contaminated	Brauer	2.17
Low	Contaminated	Bird	0.58

Table 4.2.5 shows that the variations in the biomass production are large. From the process simulations the coefficients resulting in the largest biomass production for a clean, partly contaminated, and contaminated system are, respectively; Brauer [7] on a clean system, Clift et al. [10], and Brauer [7] on a contaminated system.

If comparing these three correlations to the measurement data in Figure 2.1.7 and Figure 2.1.8, it can be seen that the coefficient by Brauer [7] on a clean system fits the measurement data by Calderbank et al. [9] relatively well for bubble sizes $0.8 - 2.0$ mm. As the bubbles in this specific process is assumed to have an average value of 2 mm, this correlation is concluded to be suitable for a clean system.

From Figure 2.1.8 it can be seen that the correlation by Clift et al. [10] fits the measurement data by Motarjemi et al. [28] quite well for bubbles of size $0.5 - 1.0$ mm. For a partly contaminated system the correlation by Clift et al. [10] gave the highest biomass production. The coefficient by Brauer [7] used on a partly contaminated system gave a high production, but the coefficient did not fit the experimental data in Figure 2.1.8.

In the case of a contaminated system, the process simulations showed that the coefficient by Brauer [7] used on a contaminated system gave the highest biomass production. However, as can be seen from Figure 2.1.8 this correlation

deviates from the experimental values. In the article by Olsen et al. [29] it was found that for a contaminated system the correlation by Hughmark [21] did fit the measurement data by Olsen et al. [29] well. Table 4.2.5 shows that the production rate of biomass is relatively high with the use of the coefficient by Hughmark [21]. The experimental data are found in laminar flow, thus the coefficients for turbulent flow is not compared to the measurement data. As described above, choosing one of the coefficients for turbulent flow used in the reactor simulations, demand knowledge about the eddy domination of the surface renewal. In addition, in this work the coefficients for turbulent flow are based on the turbulence being caused by wall friction.

4.3 Conclusion SCP

Based on the SCP reactor simulations it is found that the process is strongly mass transfer limited. Keeping the contact area high by ensuring small bubbles in the reactor, will give an increased mass transfer. Optimization of variables such as the inlet gas and liquid superficial velocities will increase the mass transferred as the bubbles will stay in the solution for a longer period of time. Investing time on optimizing the operating parameters can therefore be beneficial.

In order to have an accurate model for SCP production the mass transfer coefficient and the bubble size should be well represented. It is found that there are larger variations in the mass transferred with various choices of the mass transfer coefficient. Many of the correlations implemented in the SCP model in this work is dependent on the bubble diameter. Assuming constant bubble size therefore introduces a potentially large weakness in the model. A precise representation of the bubble size distribution in the reactor should be included. With the sensitivity to the choice of the mass transfer coefficient in SCP simulations, experimental data for the specific process is necessary in order to find a representative coefficient.

Chapter 5

Modeling of a Single Bubble

The SCP reactor simulations showed that the process is limited by mass transfer. This means that the mass transfer is the most critical part of the bio-reactor model. To improve the accuracy of the mass transfer model it is necessary to develop a model that takes into account the time rate of change in the bubble size and the mass transfer coefficient. In this part the mass transfer in a single bubble rising in a column containing water of different qualities, will be modeled. By different water qualities means water with different concentration of surfactants. The aim is to develop a model that can be used as a basis when choosing or developing mass transfer coefficients based on experimental data.

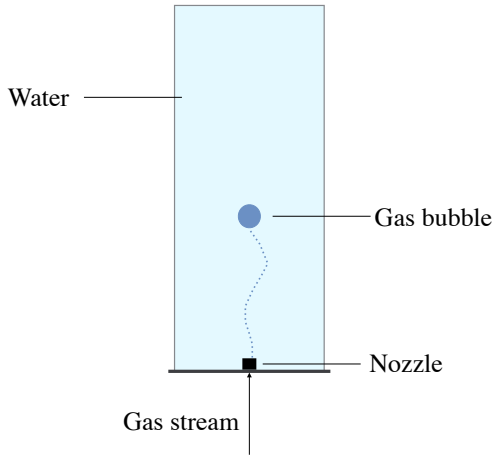

Figure 5.0.1: Single gas bubble rising in a vertical tube containing water. The water types used will vary from being clean, partly contaminated and contaminated

Figure 5.0.1 shows a schematic of a single gas bubble rising in a vertical column filled with water. The column has a length of 2 mm and an inner diameter of 0.14 m. In the beginning of the tube there is a nozzle which inserts the single bubble. The temperature is assumed to be constant at 25° C, and the outlet pressure is 1 bar. As the bubble rises the bubble size will change due to components transferring between the phases. Additionally, there will be a pressure drop over the column affecting the bubble size. It is assumed that a low bubble rise velocity will result in the bubble not breaking up into smaller bubbles.

The bubble will be introduced to three different water systems; clean, partly contaminated and contaminated. Four different gases will be used; CH_4, O_2, CO_2, and N_2. The choice of mass transfer coefficient for the clean, partly contaminated and contaminated system, is based on the results from the SCP

reactor simulations. Several of the correlations for the mass transfer coefficient is dependent on the bubble size and is therefore varying with time. The mass transfer coefficients used in the simulations are given in table 5.0.1.

Table 5.0.1: Correlations for the mass transfer coefficients used in the single bubble simulations.

System	Mass Transfer Coefficient
Clean	$k_L = 2 + 0.015 Re^{0.89} Sc^{0.7} \left(\frac{D_l}{d_b}\right)$
Partly Contaminated	$k_L = \frac{2}{\pi^{1/2}} Re^{1/2} Sc^{1/2} \left(\frac{D_l}{d_b}\right) \left(1 - \frac{2.89}{(max(2.89,(Re^{1/2})))}\right)^{1/2}$
Contaminated	$k_L = 2 + 0.95 Re^{1/2} Sc^{1/3} \left(\frac{D_l}{d_b}\right)$

In addition, to investigate the sensitivity of the system to the time dependent mass transfer coefficients, the correlations for the coefficient presented in section 2.1.2 table 2.1.1 for a laminar system, are going to be simulated for an air bubble.

The following four cases will be investigated:

- CH_4 (g) and N_2 (g)
- O_2 (g) and N_2 (g)
- CO_2 (g) and N_2 (g)
- N_2 (g), CO_2 (l) and H_2O (l)

5.1 Mathematical Model

In the SCP simulations an Eulerian model description was used where only a fixed control volume in a given point was studied. For the rising single bubble a Lagrangian model description is used where the control volume follows the bubble as it rises. Mass balances are formulated for the gas- and the liquid phase, and the time dependent bubble velocity is described by the momentum balance. The liquid phase will only be included in the model when there is dissolved gas in the liquid initially. It is assumed that the liquid velocity is zero,

the liquid density is constant, and the liquid pressure can be expressed by the static pressure, where the pressure will only vary with the height of the column. The gas inserted into the system is assumed to be ideal. As the bubble rises in the axial direction, the r- and θ coordinates are neglected. With a low rising velocity it is assumed that the single bubble does not break up into smaller bubbles.

Initial values for the rising bubble is given in table 5.1.1:

Table 5.1.1: Initial values used for a gas bubble rising in a column.

Parameter	Value Inlet	Unit
w_{in}	0.0	m/s
d_b, in	10^{-3}	m
$V_{g,in}$	$5.24 \cdot 10^{-10}$	m^3
$p_{l,out}$	10^5	Pa

5.1.1 Pressure

The liquid pressure in the column does only change with the column height, z. To express the liquid pressure, p_L, the static pressure equation is used:

$$\frac{dp_L}{dz} = -\varepsilon_L \rho_L g \tag{5.1.1}$$

It is assumed that the liquid velocity is approximately zero, thus $\varepsilon_L \approx 1$. Integrating equation (5.1.1) over the column length where the pressure at the top of the tube, $p_{out} = 1$ bar results in the following expression for the liquid pressure:

$$p_L(z) = p_{out} + \rho_L g z \tag{5.1.2}$$

The liquid and gas pressure can be related through the Young-Laplace equation [22]:

$$\Delta p = \frac{-2\sigma}{r} \tag{5.1.3}$$

where Δp is the difference between the gas and the liquid pressure, σ is the surface tension, and r is the bubble radius. Solving for the gas pressure in

equation (5.1.3) gives:

$$p_g - p_l = -\frac{4\sigma}{d_b} \tag{5.1.4}$$

where d_b is the bubble diameter.

For the bubble size range used in the simulations, the right hand side of equation 5.1.4 is very small compared to the liquid pressure, and it is assumed that the gas pressure equals the liquid pressure:

$$p_g = p_l \tag{5.1.5}$$

5.1.2 Total Mass

To express the change in total mass, the following equation can be used:

$$\frac{d}{dt}\left(\rho_b V\right) = -\dot{m}_b A \tag{5.1.6}$$

Here it has been assumed that the density inside the bubble is uniform, that there is mass transfer out of the bubble, and that there are no concentration gradients along the surface. These assumptions are also made for the species mass balance and the momentum balance. The mass flux can be expressed as:

$$\dot{m}_b = \sum_k k_{L,k}(\rho^*_{k,l} - \rho_{k,l}) = \sum_k \left(\frac{k_{L,k} w_{k,g} p_g \bar{M}_g}{H_k} - \rho_l w_{k,l} \right) \tag{5.1.7}$$

If it is assumed that the concentration of component k in the liquid phase is negligible the total mass flux becomes:

$$\dot{m}_b = \sum_k k_{L,k} \rho^*_{k,l} = \sum_k \frac{k_{L,k} w_{k,g} p_g \bar{M}_g}{H_k} \tag{5.1.8}$$

Assume ideal gas results in the following equation for the volume:

$$\frac{dV}{dt} = \frac{-\dot{m}_b A}{\rho_g} - \frac{V}{\rho_g}\left[\frac{\bar{M}_g}{RT}\frac{dp_g}{dt} + \frac{p_g}{RT}\frac{d\bar{M}_g}{dt} \right] \tag{5.1.9}$$

The complete derivation of the total mass is given in Appendix A.9.1.

5.1.3 Species Mass Balance

The species mass balance is formulated for the gas- and liquid phase.

Gas Phase

The change in mass of component A can be given by the following equation:

$$\frac{d}{dt}\left(\rho_{A,g}V\right) = -\dot{m}_A A \tag{5.1.10}$$

$$V\rho_g \frac{dw_{A,g}}{dt} + Vw_{A,g}\frac{d\rho_g}{dt} + \rho_{A,g}\frac{dV}{dt} = -\dot{m}_A A \tag{5.1.11}$$

The mass flux of component A can be expressed as:

$$\dot{m}_A = k_{L,A}(\rho^*_{A,l} - \rho_{A,l}) \tag{5.1.12}$$

An assumption of negligible concentration of component A in liquid phase, reduces 5.1.13 to:

$$\dot{m}_A = k_{L,A}\rho^*_{A,l} = \frac{k_{L,A}w_{A,g}p_g\bar{M}_g}{H_A} \tag{5.1.13}$$

Solving for the species mass the following equation is obtained for the rate of change of specie A in gas phase:

$$\frac{dw_{A,g}}{dt} = \frac{-\dot{m}_A A}{V\rho_g} + \frac{w_A\dot{m}_b A}{V\rho_g} \tag{5.1.14}$$

where the total mass flux is given by equation (A.9.45).

For the full derivation of the species mass balance for the gas phase see appendix A.9.2.

Liquid Phase

The change in mass of component A in the liquid phase can be written as:

$$\frac{d}{dt}\left(\rho_{A,l}V\right) = \dot{m}_A A \tag{5.1.15}$$

where the gas is transported from the gas phase to the liquid phase, thus the positive mass flux given by equation 5.1.13. The derivation of the mass change

in liquid phase is the same as for the gas phase, only that the liquid density and the liquid volume is assumed constant, in addition to the positive mass flux. Thus the change of mass in liquid phase can be expressed as:

$$V_l \rho_l \frac{dw_{A,l}}{dt} = \dot{m}_A A \tag{5.1.16}$$

with the liquid volume, V_l, given by the volume of the column:

$$V_l = \frac{\pi}{4} d_c^2 l \tag{5.1.17}$$

where d_c is the diameter and l is the length of the tube.

5.1.4 Momentum Balance

An assumption of uniform density inside the bubble and no concentration gradients along the surface, gives the following equation for the momentum balance:

$$\frac{d(m_g w_g)}{dt} = -m_g g - \dot{m}_g \underline{\mathrm{v}}_g A + (F_D + F_B) A \tag{5.1.18}$$

where $m_g g$ express the gravity force, F_D is the drag forces, F_B is the buoyancy forces, $\underline{\mathrm{v}}_g = w_g$, and the gas mass flux is out of the bubble.

The drag forces are given by:

$$F_D = \frac{1}{2} C_D \rho_l |w_r| w_r A \tag{5.1.19}$$

where the relative velocity, w_r, is given by:

$$w_r = w_g - w_l \tag{5.1.20}$$

As the liquid velocity is assumed to be zero, the relative velocity is equal to the gas velocity.

The bouyancy forces are given by:

$$F_B = V \rho_l g \tag{5.1.21}$$

With the expressions for the drag force and bouyancy forces from equation A.9.35 and 5.1.21, respectively, the expression for the change in velocity becomes:

$$\frac{d\mathrm{w}_g}{dt} = -g + \frac{\rho_l}{\rho_g}g - \frac{1}{2}\frac{C_D\rho_l\mathrm{w}_g^2 A}{V\rho_g} \tag{5.1.22}$$

From equation 5.1.22 it can be seen that when the forces are in equilibrium there is no change in the velocity. The total derivation of the momentum balance is given in appendix A.9.3.

5.1.5 Bubble Diameter

When deriving the equation for the change in bubble diameter, the same assumptions regarding the density inside the bubble and the concentration gradients can be done as for the total mass, component mass and the velocity. This gives the following equation for the change in bubble diameter:

$$\frac{d(d_b)}{dt} = \frac{-2\dot{m}_b A}{\pi d_b^2 \rho_g} - \frac{d_b}{3\rho_g}\frac{d\rho_g}{dt} \tag{5.1.23}$$

Inserting for the change in gas density, equation (A.9.14), found when deriving the change in volume in appendix A.9.1, gives:

$$\frac{d(d_b)}{dt} = \frac{-2\dot{m}_b}{\rho_g} - \frac{d_b}{3\rho_g}\left(\frac{p_g}{RT}\frac{d\bar{M}_g}{dt} + \frac{\bar{M}_g}{RT}\frac{dp_g}{dt}\right) \tag{5.1.24}$$

where the gas pressure is expressed by equation (5.1.5).

It should be noted that equation (5.1.24) is not an independent equation. As an alternative the bubble size could be found by using the volume obtained from the total mass balance and inserted into the following equation for the bubble volume:

$$V = \frac{\pi}{6}d_b^3 \tag{5.1.25}$$

5.1.6 Implementation

The solution method used in the simulations of a single bubble is the same as for the SCP production, the orthogonal collocation method. In this section

the placement of the terms in the equations presented above will be given. In addition the experienced implementation difficulties will be discussed.

Momentum Balance

The time derivative and the drag coefficient were placed in the **A**-matrix. The gravitational forces and the buoyancy forces were placed in the **F**-vector. This was found to give the most diagonally dominant **A**-matrix. In order to place the drag force in the **A**-matrix it had to be linearized, where the last iteration value for the velocity was used.

Species Mass Balance

Species mass balances for the components were solved separately. The change in the mass fraction and the component mass flux were placed in the **A**-matrix. The total mass flux was placed in the **F**-vector.

Total Mass

In the total mass balance the time derivative of the volume and the change in gas density were placed in the **A**-matrix. The total mass flux was placed in **F**-vector.

Maximum Time

The time it takes the bubble use to move from the bottom to the top of the column varied for the different systems. The length traveled was compared to the time used, and the the maximum time was adjusted if needed such that the time corresponded to the bubble traveling 2 m.

Implementation Difficulties

There were initially some problems when solving for the velocity. This was found to be due to the initial guess being equal to the inlet value, $w_{in} = 0$. As the bubble accelerates very fast in the beginning of the column, the solution was far away from the guessed value. Numerically the solution reaches a local minimum and gives the wrong solution value. To solve this, the guesses should be different from the initial value for the internal solution points.

In the simulation of the carbon dioxide and nitrogen bubble, the initial mass fractions was first chosen to be $w_{CO_2} = 0.4$ and $w_{N_2} = 0.6$. With these initial values the mass fractions did not sum to one. The initial mass fractions were changed to be $w_{CO_2} = 0.1$ and $w_{N_2} = 0.9$. This gave solutions where $\sum_k w_{k,g} = 1$. The reason for the mass not being conserved can be explained by the solubility

of carbon dioxide in water. With the carbon dioxide dissolving very fast in the liquid, approximately all the gas transfers from the bubble over the column. This means that when using the initial value of $w_{CO_2} = 0.4$ as guess for all the solution points, the solution value will be far away from the guess. If it is desired to increase the initial mass fraction of carbon dioxide, it is necessary to guess solution values with care. This was done for the carbon saturated water-case, where the change in mass fraction of carbon dioxide in gas phase was large.

Chapter 6

Results Single Bubble

In this section, the results of the single bubble model will be presented. The section will start out by noting an error with the implementation.

When the single bubble model was implemented in MATLAB, a mistake were made in the expression for the area of a bubble. The area was written as $A = \pi d_b^2/4$, instead of $A = \pi d_b^2$. It should be noted that the model equations themselves given in section 5.1 are not wrong. Thus the contact area used in the reactor simulations included a mis-scaling by a factor of 4. It is expected that this will not affect the comparison between the water systems, as all the systems will be affected by the same mis-scaling. Due to the detection of the bug at a late stage, the single bubble model is not simulated with the correct implementation. However, to show the effect of using the correct bubble area, a bubble containing 20% methane and 80% nitrogen was simulated by use of the correct and incorrect bubble area.

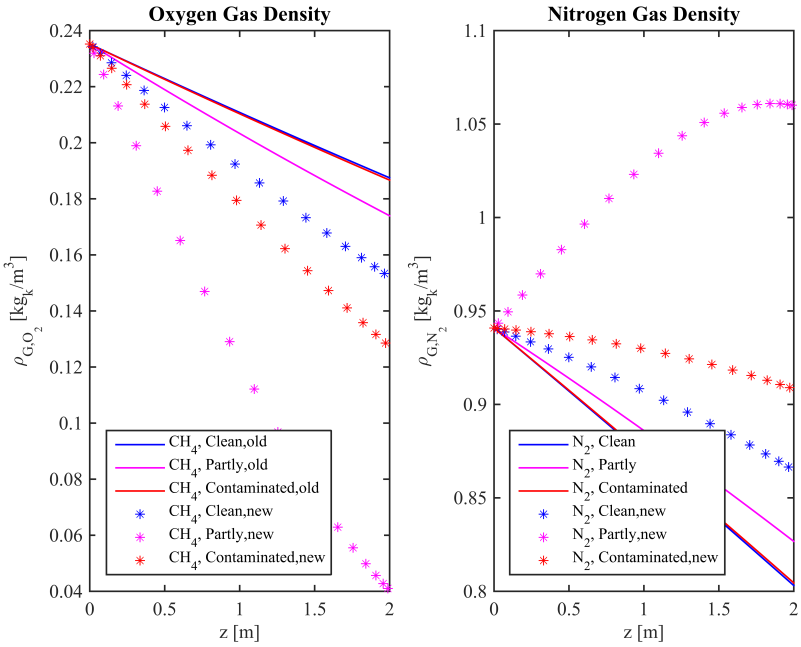

Figure 6.0.1: Oxygen and nitrogen gas densities with use of the correct and incorrect bubble area. The profiles with the correct bubble area are denoted as CH_4,system,new, where system = clean, partly contaminated and contaminated. The profiles with the incorrect bubble area are denoted as CH_4,system,old, where system = clean, partly contaminated and contaminated.

With an increase in the contact area with a factor of 4, it is expected that more of the gas is dissolved. From Figure 6.0.1 it can be seen that with the correct expression for the bubble area, more of the oxygen is transferred for all the systems. The nitrogen component for all the systems regardless of the right or wrong bubble area, shows the opposite trend regarding the mass transfer as that of oxygen. Figure 6.0.1 shows that especially the partly contaminated system is affected by the new scaling.

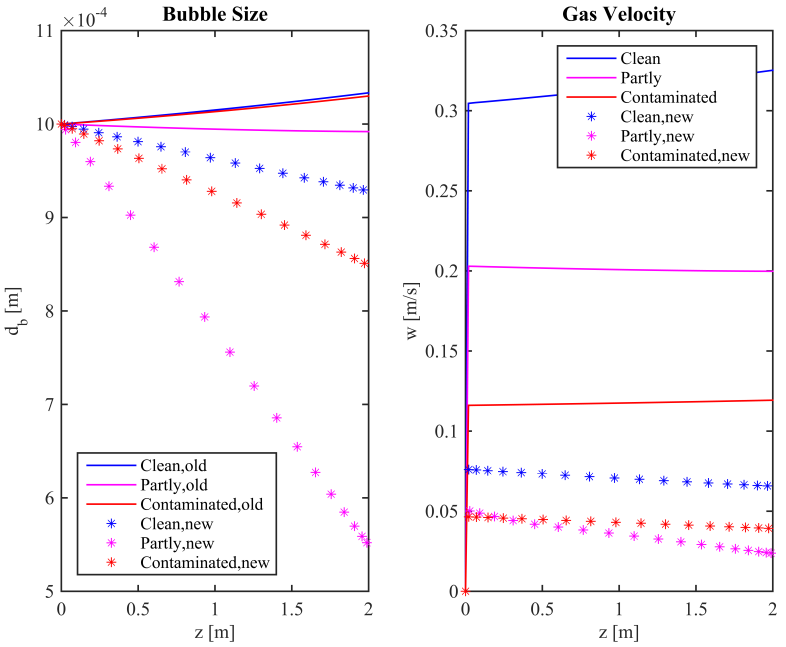

Figure 6.0.2: Bubble diameter and terminal velocities with use of correct and incorrect bubble area. The profiles with the correct bubble area are denoted as clean,new, partly contaminated,new and contaminated,new. The profiles with the incorrect bubble area are denoted as clean,old, partly contaminated,old and contaminated,old.

With more of the gas transferred for the correct bubble area, the bubble size decreases, as shown in Figure 6.0.2. For the wrong bubble area, the mass transfer is smaller than the change in in pressure and composition, thus the diameter increases, seen from equation (5.1.24). For the partly contaminated system the mass transfer is approximately equal to the pressure and composition change, thus the bubble diameter is approximately constant. From Figure 6.0.1 it can be seen that the mass transfer is much larger than for the old bubble area. With the bubble diameter decreasing for the new bubble area, this means that the mass transfer is larger than the change in pressure and composition. The change in bubble size affects the drag coefficient, thus affecting the velocity. With the

decrease in bubble size seen in Figure 6.0.2, the velocity is decreased.

From Figure 6.0.1 and Figure 6.0.2 it is seen that the correct implementation of the bubble area affects the result. Thus new simulations with the new bubble area should be performed. Nevertheless, it is expected that the overall trends of the presented results is still valid.

6.1 Oxygen and Nitrogen

Initially the column is filled with water of different qualities and an air bubble containing $w_{O_2,g} = 0.21$ and $w_{N_2,g} = 0.79$ is introduced.

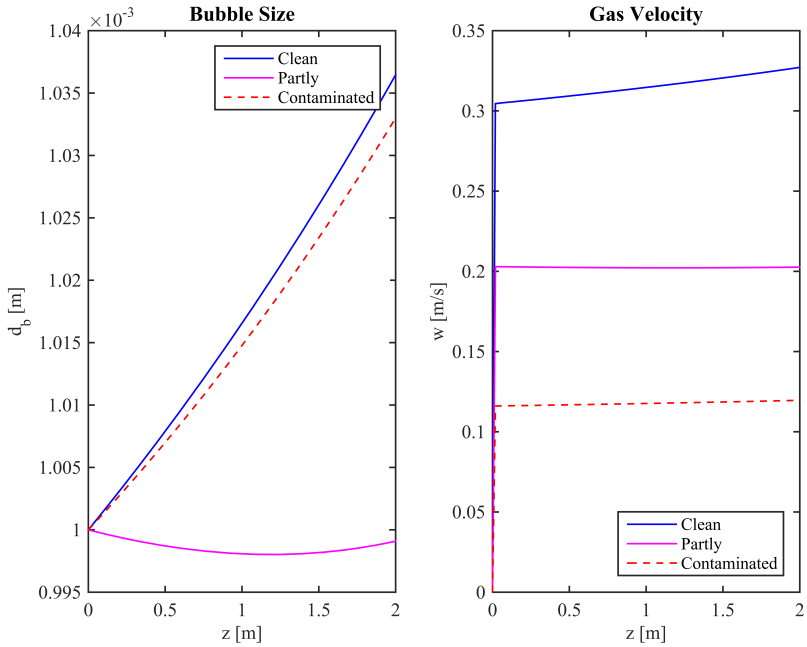

Figure 6.1.1: Change in gas velocity and bubble size over the tube for a bubble containing initially 21% oxygen and 79% nitrogen.

The bubble size is expected to decrease as the gas is transported out of the bubble. However, as the bubble rises there will be a pressure drop over the column resulting in the bubble expanding. The change in bubble size can be seen from Figure 6.1.1. With the net increase in bubble size this indicates that the the pressure loss and change in composition is larger than the mass flux, seen from equation (5.1.24). From Figure 6.1.1 the bubble diameter for the partly contaminated system is approximately constant, which can be explained by the same principle as above.

It is expected that the velocity for a rising bubble in water will decrease with increasing concentration of surfactants. In figure 6.1.1 the bubble accelerates fast in the beginning of the column. This is due to the forces not being in equilibrium in the first part. When the drag force and the gravitational force, which is working in a downwards direction, and the buoyancy forces lifting the bubble, are in equilibrium, a terminal bubble velocity is reached. If the bubble size changes the system adjust and a new terminal velocity may be reached. The volume change in the clean system causes the terminal velocity to increase slightly. As expected, the velocity in the contaminated system, with the highest concentration of surfactants, is the lowest. For the partly contaminated system the bubble velocity is increased compared to the contaminated one, due to less surfactants present. With no surfactants present in the clean system, the velocity is the highest.

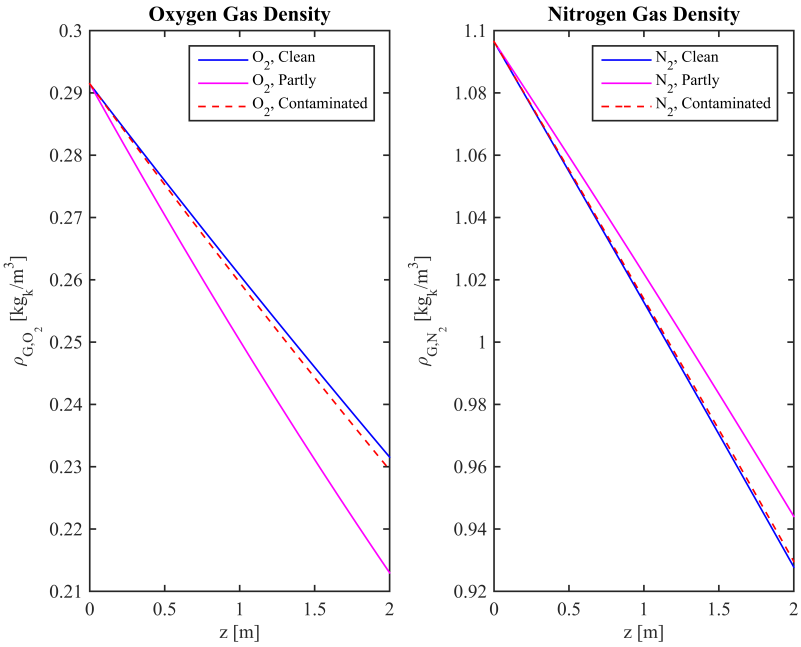

Figure 6.1.2: Component gas densities for a bubble containing initially 21% oxygen and 79% nitrogen.

In a partly contaminated and a contaminated system, the surfactants can accumulate near the bubble and by this hinder mass transferring. It is therefore to be expected that more of the gas will dissolve for a clean system compared to the contaminated systems.

As seen in Figure 6.1.2, the mass transfer of oxygen is the highest for the partly contaminated system. For the clean and contaminated system the difference in oxygen transfer is relatively small. The hypothesis was that the clean system would give the highest mass transfer rates. However, when surfactants are present in the solution this will reduce the bubble velocity, as shown in Figure 6.1.1. This results in the bubbles staying in the column for a longer period of time and there will be more time for the gas to dissolve. By this explanation the contaminated system should have a larger mass transfer than the clean

system and the partly contaminated one. In a contaminated system there will be more surfactants present than in a partly contaminated one. Even though this will result in a lower rise velocity this will also result in more surfactants surrounding the bubble. By these physical explanations, the result of the partly contaminated system giving the highest mass transfer of oxygen seems to be a valid result.

For the nitrogen component in Figure 6.1.2 it can be seen that the partly contaminated gives the lowest mass transfer of the three systems. This was not expected, as the largest mass transfer of oxygen was obtained in the partly contaminated system. Figure 6.1.3 shows that the coefficient for nitrogen is slightly smaller than for oxygen. However, the coefficient is larger than for the clean and contaminated system, thus the transfer of nitrogen for the partly contaminated system is expected to be the largest. Seen from Figure 6.1.2, this is not the case. A possible explanation to this trend is that the mass transfer coefficients used for the clean and contaminated systems are relatively similar, when $Re \to 0$, $\mathrm{k}_L \to 2$. The mass transfer coefficient used for a partly contaminated system, proposed by Clift et al. [10], is deviating from those by Brauer [7] and Hughmark [21], where an additional part is included in the correlation. There could be that when using the coefficient by Clift et al. [10] in this specific model, the coefficient is not physical. Further investigation of the coefficient for a partly contaminated system is therefore needed.

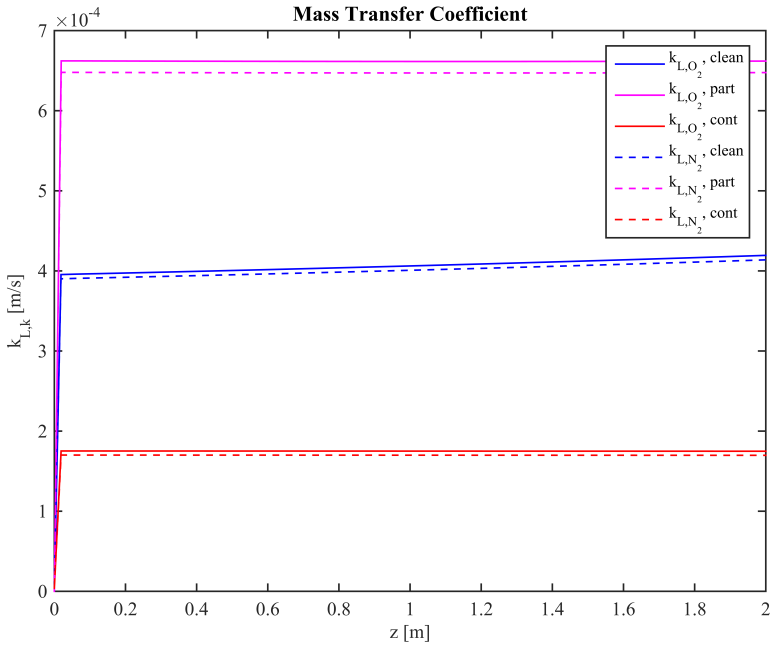

Figure 6.1.3: Mass transfer coefficients for a bubble containing initially 21% oxygen and 79% nitrogen.

From Figure 6.1.3 the mass transfer coefficient for the partly contaminated system is found the be significantly larger than those for the clean and contaminated system.

Table 6.1.1: Oxygen and nitrogen transferred from an air bubble containing 21% oxygen and 79% nitrogen for different water systems.

System	Oxygen transferred [%]	Nitrogen transferred [%]	Volume change [%]
Clean	20.7	15.5	11.4
Partly Contaminated	27.0	14.0	0.03
Contaminated	21.3	15.2	10.0

Table 6.1.1 shows that the percentage transfer of the oxygen is affected by the system, whereas the transfer of nitrogen is very similar. Note that this is the percentage transfer of the 21% oxygen and 79% nitrogen in the bubble.

As described above, the trend of the partly contaminated system could be due to use of the mass transfer coefficient by Clift et al. [10]. To investigate the effect of using the same correlation on all systems, the coefficient proposed by Brauer [7] has been used on all the systems. The systems will deviate from each other through the expressions for the drag coefficient.

It was found that the gas transferred is approximately equal for all the systems with use of the same correlation, for both the components. Profiles for the component gas densities, velocity, and bubble diameter with use of the same coefficient are given in appendix A.3.

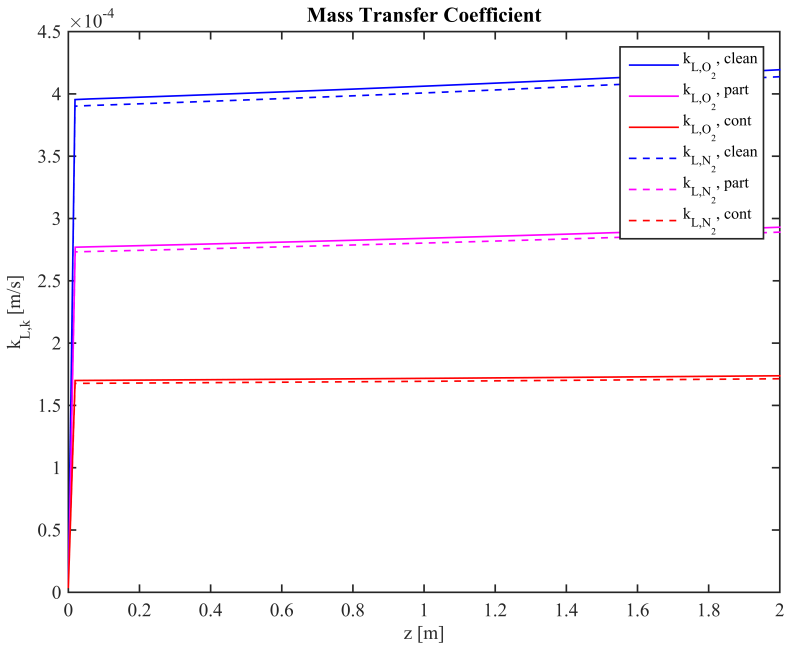

Figure 6.1.4: Mass transfer coefficients with use of the correlation by Brauer [7].

Using the correlation proposed by Brauer [7] for a partly contaminated system result in a reduced value for the coefficient compared to that by Clift et al. [10]. The component densities is found to be approximately equal for all the systems, which deviates from the results obtained by use of the coefficient proposed by Clift et al. [10]. This shows the importance of using an accurate correlation for the specific process in order to obtain a precise representation of the mass transfer. Additional figures for the gas volume, pressure and mass fractions for the air bubble are given in appendix A.3.

6.1.1 Constant and Varying Volume

From table 6.1.1 it was found that the change in the volume was relatively small for the systems. In the article by Bishof et al. [4], where the oxygen transfer of a single bubble for different water systems was investigated, it was assumed that the gas volume is constant over the column. Assuming constant volume means that the mass transfer coefficients dependent on the bubble size, will lose this representation.

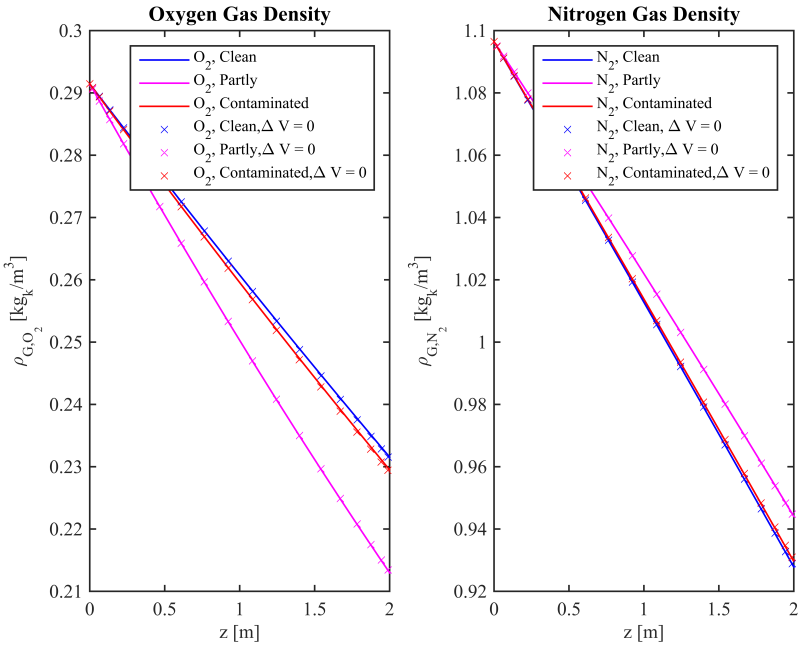

Figure 6.1.5: Component gas densities for a bubble containing initially 21% oxygen and 79% nitrogen, for both constant and varying bubble volume.

From Figure 6.1.5 the change in the component gas density is seen to be independent of the bubble volume. This means that the volume changes for the clean and contaminated systems, given in table 6.1.1 are insignificant, and does not affect the mass transfer. It should be noted that this conclusion is made for bubbles in the size range as the one in this work, for other bubble sizes this is not necessarily the case.

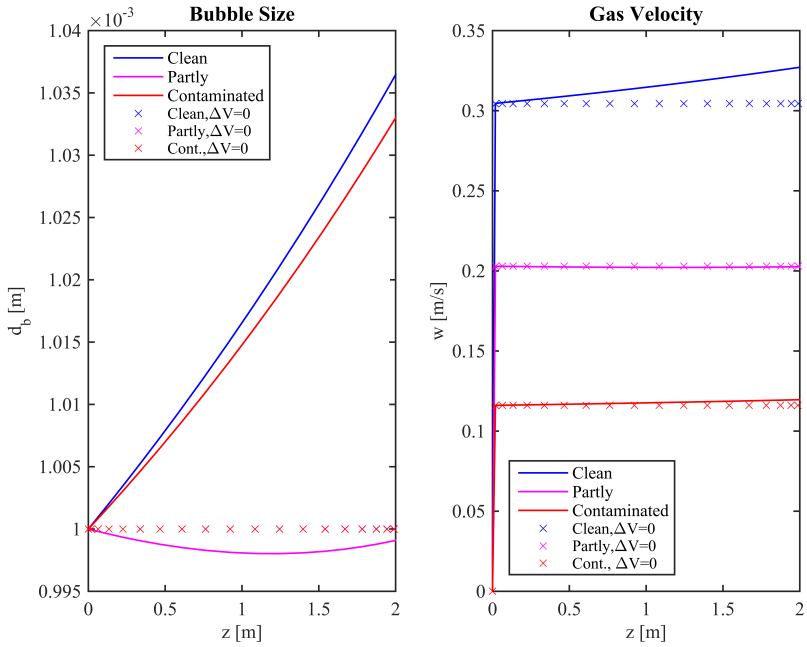

Figure 6.1.6: Bubble velocity and diameter for a bubble containing initially 21% oxygen and 79% nitrogen, for both constant and varying bubble volume.

It should be noted that the points for the clean and partly contaminated system does not show in Figure A.3.2, as they lie under the profile for the contaminated system. With the component gas densities being equal, it is the change in volume that causes the variations between the systems for the terminal velocity. For a clean system the terminal velocities are deviating, due to the increase in volume being of a significant value. A slight increase is also seen for the contaminated system. In the discussion of Figure 6.1.1 it was stated that the change in velocity of the air bubble was due to the change in both gas density and volume. By Figure A.3.2 it seems that for this specific system, the increase in terminal velocity is due to the change in volume.

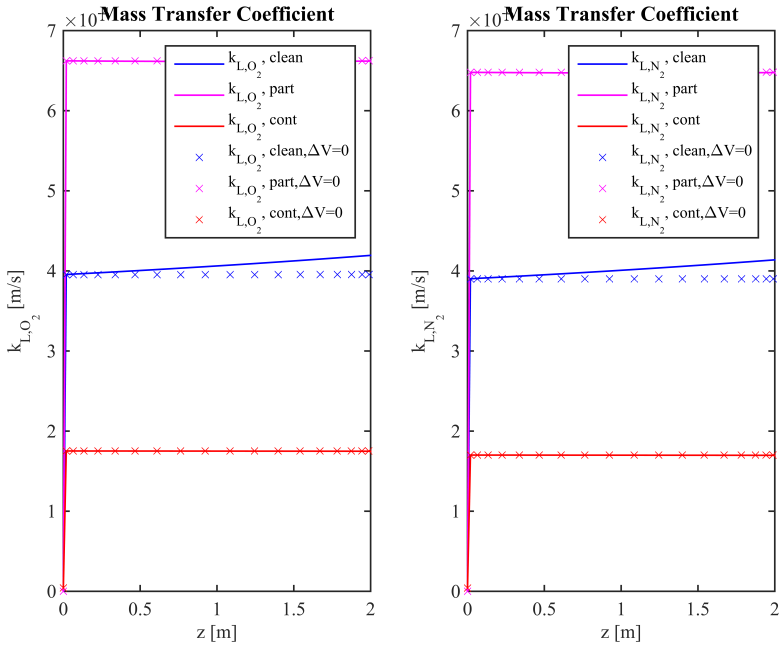

Figure 6.1.7: Mass transfer coefficients for a bubble containing initially 21% oxygen and 79% nitrogen, for both constant and varying bubble volume.

With the mass transfer coefficient being dependent on the terminal velocity and the bubble size, it is to be expected that the variation in bubble size and velocities will cause deviations for the constant and varying volume assumptions. Figure 6.1.7 shows that there are only deviations in the coefficient for the clean system. This can be explained by the terminal velocity, seen in Figure A.3.2.

Table 6.1.2: Oxygen and nitrogen transferred from a bubble containing initially 21% oxygen and 79% nitrogen, for both constant and varying bubble volume.

System	Oxygen transferred [%]	Nitrogen transferred [%]
Clean	20.7	15.5
Partly Contaminated	27.0	14.0
Contaminated	21.3	15.2
Clean, $\Delta V = 0$	20.8	15.5
Partly Contaminated, $\Delta V = 0$	27.0	14.0
Contaminated, $\Delta V = 0$	21.5	15.2

Seen from table 6.1.2, the percentage oxygen transferred is not affected significantly with the assumption of constant gas volume. Based on these findings, for the bubble size range used in this work, the assumption of constant gas volume is a good assumption. However, it should be noted that the change in bubble size will only be caused by mass transfer, pressure variations and change in composition, as only one bubble is modeled. In a multi-bubble system additional mechanisms like coalescence and breakage can cause the bubbles to change size. This means that the bubble sizes can be much larger and smaller than the size range in this work. Assuming a constant gas volume could therefore potentially induce weaknesses in the model. The mass fractions, pressure and volume profiles are given in appendix A.3.

6.2 Methane and Nitrogen

A rising bubble containing methane (40%) and nitrogen (60%) has been simulated. The mass transfer of methane and nitrogen was found to result in the same trends as the air bubble in section 6.1, and the profiles are therefore given in appendix A.3. The solubility of oxygen is higher than that of methane, and it is expected that less methane dissolve compared to oxygen. However, as the inlet methane density in the bubble is higher than for oxygen in the O_2-N_2-case, the driving force will be larger. The nitrogen component shows the same trend as the air bubble, however, less nitrogen is dissolved due to lower initial component density.

In the clean and contaminated system the bubble diameter increases. The bubble size in the partly contaminated system decreases over the column, as the mass flux is larger than the pressure loss and change in composition, given by equation 5.1.24.

The decrease in the bubble diameter is of a size that cause the terminal velocity to decrease. In addition the gas density could affect the terminal velocity, even though this was not the case for the air-bubble. The increase in bubble diameter for the clean and contaminated system results in the terminal velocity increasing.

Table 6.2.1: Methane and nitrogen transferred from a bubble containing 40% methane and 60% nitrogen.

System	Methane transferred [%]	Nitrogen transferred [%]
Clean	19.2	13.4
Partly Contaminated	23.2	8.5
Contaminated	19.4	13.1

Table 6.2.1 shows the percentage methane and nitrogen transferred. Note that this is the percentage transfer out of the initial 40% methane and 60% nitrogen. The component gas densities, mass fractions, the pressure, and volume profiles are given in appendix A.3.

6.3 Carbon dioxide and Nitrogen

A bubble containing 10% carbon dioxide and 90% nitrogen has been simulated. Carbon dioxide has a much larger solubility in water than methane and oxygen. It is therefore expected that more of the component dissolves during the time in the column. The simulation results showed that carbon dioxide dissolves very rapidly, and after 2 m there is little carbon dioxide left in the bubble. For a partly contaminated system, approximately all the carbon dioxide is transferred. The carbon dioxide containing bubble shows the same trends as the O_2-N_2 and CH_4-N_2 bubble. However, in the beginning of the column the nitrogen density for the partly contaminated system shows a jump before it starts to decrease. An explanation to this could be the unphysicality discussed in section 6.1, and

as stated the coefficient for a partly contaminated system needs to be given extra concern in future modeling work. Examples on further investigation is to look at the effect of the Reynolds number. Investigating individual effects of the terms in the correlations could reveal underlying causes.

Table 6.3.1: Carbon dioxide and nitrogen transferred from a bubble containing 40% carbon dioxide and 60% nitrogen.

System	Carbon dioxide transferred [%]	Nitrogen transferred [%]
Clean	84.0	4.1
Partly Contaminated	99.1	3.0
Contaminated	87.4	3.7

Table 6.3.1 shows that approximately all the CO_2 dissolves in the water for the partly contaminated system. The profiles for the bubble containing carbon dioxide and nitrogen are given in appendix A.3.

6.4 Nitrogen Bubble in Carbon dioxide Saturated Water

Initially the column contains water saturated with carbon dioxide, $w_{CO_2,l} = 0.0015$. A bubble containing nitrogen is then introduced. As the carbon dioxide will transport between the phases, both phases are taken into consideration in the simulations.

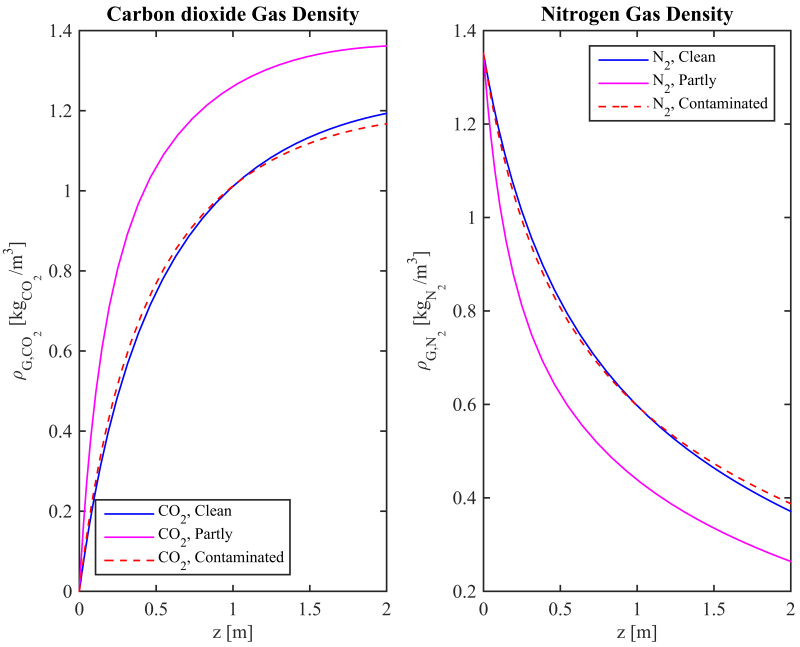

Figure 6.4.1: Component gas densities for a bubble containing initially 100% nitrogen rising in a tube with carbon saturated water.

With the initial concentration of carbon dioxide in the gas being zero, the driving force will be very large. This results in the carbon dioxide transferring from the liquid to the gas phase rapidly. Figure 6.4.1 shows that the largest transfer of carbon dioxide and nitrogen is obtained in the partly contaminated system. With the water only staying in the liquid phase at 25° C, the evaporation is neglected.

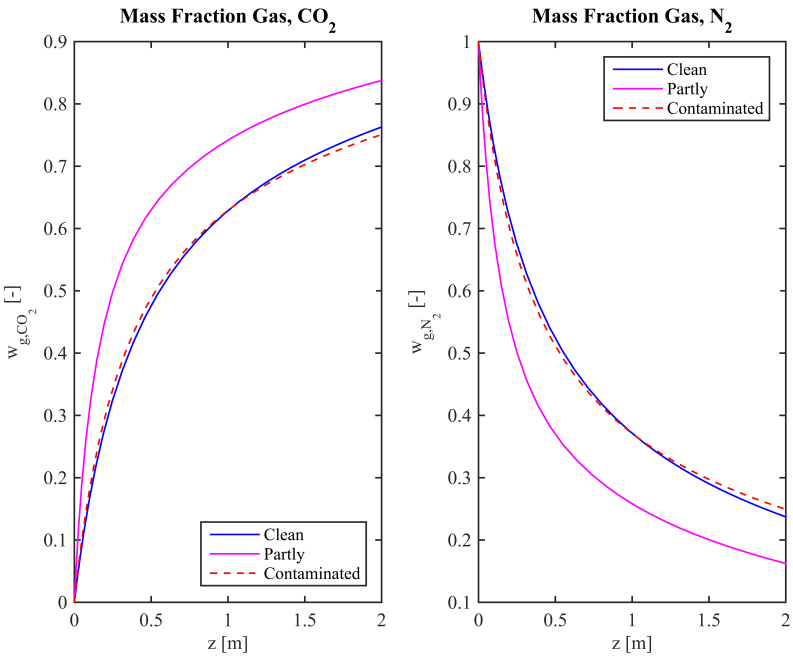

Figure 6.4.2: Component gas densities for a bubble containing initially 100% nitrogen rising in a tube with carbon saturated water.

As the carbon dioxide transfer to the gas phase, the mass fraction of carbon dioxide increases. The mass fractions in the clean and the contaminated system are approximately equal. With higher mass transfer of the carbon dioxide and nitrogen for a partly contaminated system, the mass fractions increases and decreases the most for this system, shown in Figure 6.4.2.

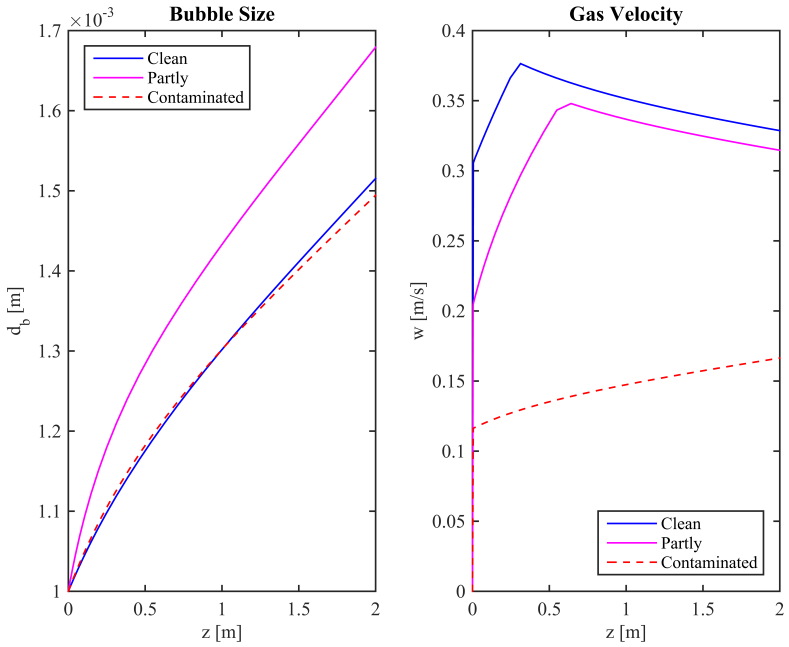

Figure 6.4.3: Bubble diameter and velocity profiles for a bubble containing initially 100% nitrogen rising in a tube with carbon saturated water.

The carbon dioxide transferring into the gas phase results in the bubble size increasing. Compared to the cases with oxygen, methane and carbon dioxide in the gas phase initially, the bubble diameter is increased largely due to carbon dioxide transferring from the liquid to the gas phase.

In section 2.1.2 the reproduced profiles by Olsen et al. [29], Figure 2.1.6, shows the variation in the terminal velocity and the drag coefficient with varying bubble size. With the increase in the bubble diameter being relatively large for the N_2-CO_2(l)-H_2O-case, compared to the O_2-N_2, CH_4-N_2, and CO_2-N_2-cases, this will cause a larger effect on the velocity. The terminal velocities in Figure 6.4.3 shows the same trends for a clean and partly contaminated system as the terminal velocity in Figure 2.1.6. Note that Figure 6.4.3 shows the velocity over the column length, whereas Figure 2.1.6 shows the the velocity as a function

of bubble size. Comparing the bubble size at 0.5 m to the velocity in Figure 6.4.3 for the clean system, it can be seen that the bubble diameter being approximately 1.3 mm matches the bubble diameter for the shift in Figure 2.1.6. The shift in the terminal velocity is due to the bubbles transforming from a spherical to a non-spherical shape. For a contaminated system there is no shift. Regarding Figure 2.1.6, the shift from spherical to non-spherical bubbles for a contaminated system found by Olsen et al. [29], occurs for $d_b > 3$ mm. The bubble size for the contaminated system is 1.5 mm in the end of the column, thus the bubbles will not exhibit this transformation.

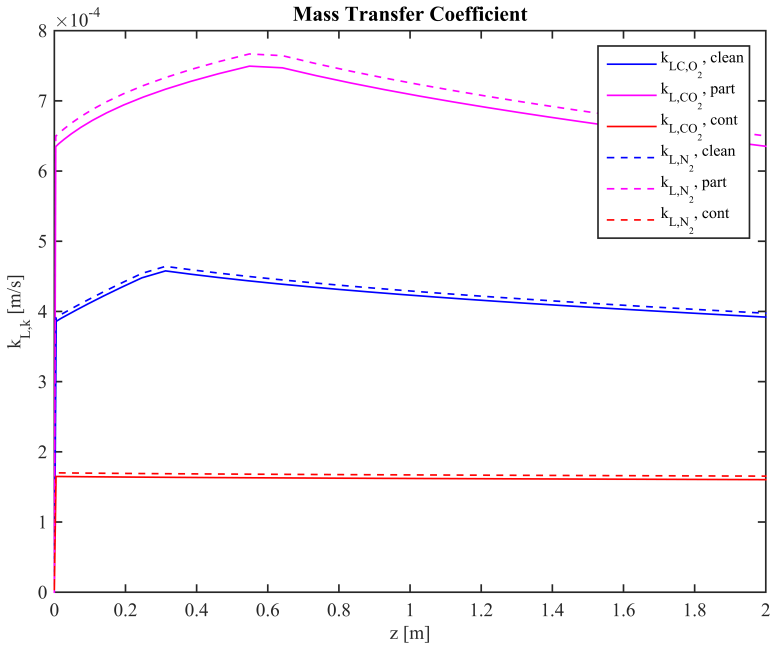

Figure 6.4.4: Mass transfer coefficients for carbon dioxide and nitrogen initially 100% nitrogen rising in a tube with carbon saturated water.

The effect of the change in terminal velocity is shown in the mass transfer coefficients in Figure 6.4.4. With a shift in the terminal velocity there will be a shift in the mass transfer coefficient. Additional profiles for the liquid mass

fractions, velocity and pressure are given in appendix A.3.

6.5 Various Mass Transfer Coefficients

With the sensitivity to the choice of correlation for the mass transfer coefficient in section 6.1, it is of interest to simulate the air bubble with various expressions. The correlations for laminar flow from table 2.1.1 will be used.

Clean System

The profiles for various mass transfer coefficients shown in Figure 6.5.1 can be seen to give significantly different mass transfer of oxygen. Comparing the highest mass transfer obtained by use of coefficient proposed by Higbie [20] to the coefficient giving the lowest transfer proposed by Calderbank et al. [9] for small bubbles, the percentage oxygen transferred is 26.1% and 17.7%, respectively. The nitrogen density profile shows the opposite trend as that of oxygen, as described in section 6.1.

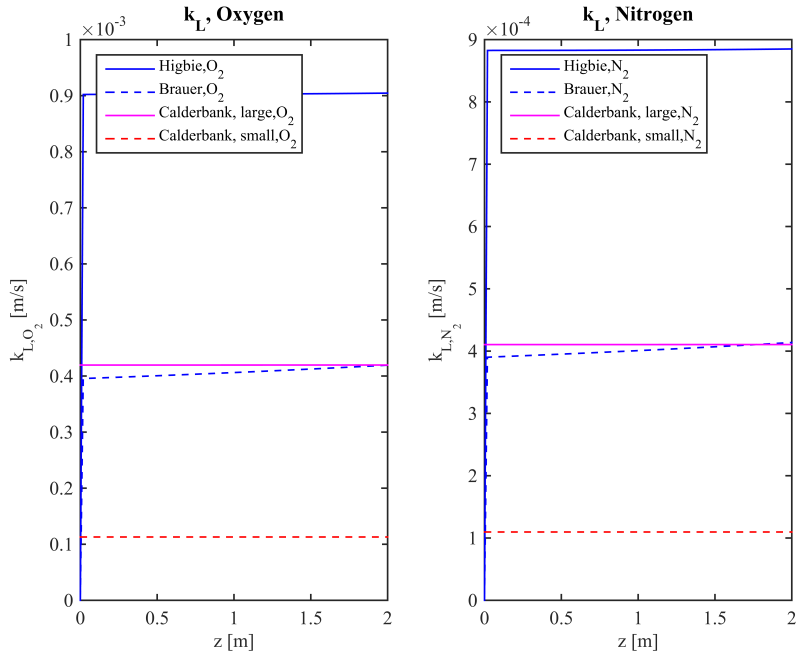

Figure 6.5.1: Mass transfer coefficients for oxygen and nitrogen for a clean system.

With approximately the same value for the coefficient by Brauer [7] and Calderbank et al. [9] for large bubbles, the driving force is equal and thus the component densities in Figure 6.5.1 are equal. As the mass transfer coefficient only occurs in the mass flux, the variations in the bubble diameter, volume and velocity is expected to be the same for the two correlations. The coefficient by Higbie [20] is significantly larger than the other correlations, which explain the larger oxygen transfer.

With the relatively constant bubble size for Higbie [20], the bubble reaches a constant terminal velocity. For the other relations, where the volume is varying, the velocity increases. There are relatively large deviations in the gas transferred for the correlations, as seen in table 6.5.1, where the coefficient by Higbie [20] gives a much higher mass transfer than that by Calderbank et al. [9] for small bubbles. This means that choosing the wrong correlation could result

in misleading information regarding the mass transfer.

Table 6.5.1: Oxygen and nitrogen transfer with various correlations for the mass transfer coefficient for a clean system.

System	Mass Transfer Coefficient	Oxygen transferred [%]	Nitrogen transferred [%]
Clean	Calderbank, small	17.7	16.2
Clean	Calderbank, large	21.0	15.6
Clean	Higbie	26.1	14.2
Clean	Brauer	20.7	15.5

Partly Contaminated System

Two correlations for the partly contaminated system have been simulated, one proposed by Clift et al. [10] and one by Brauer [7] used on a partly contaminated system.

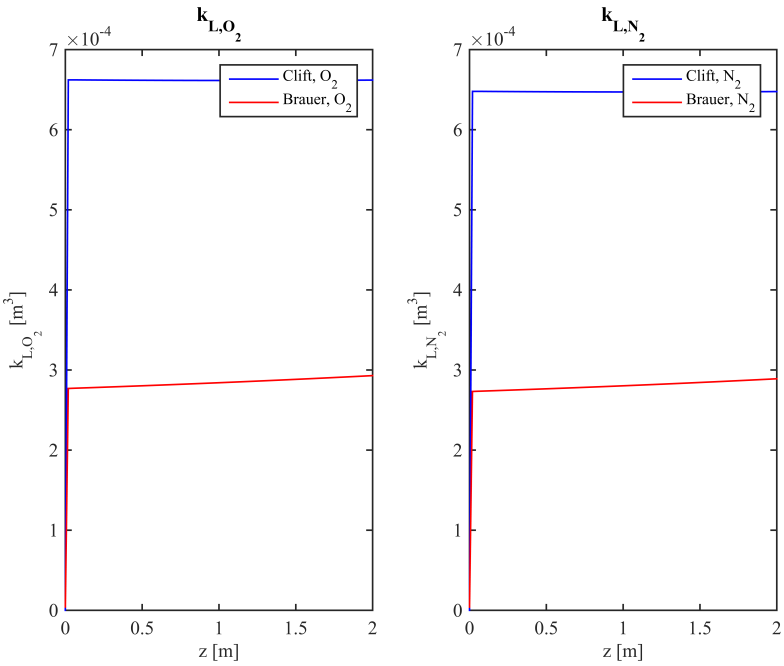

Figure 6.5.2: Mass transfer coefficients for oxygen and nitrogen for a partly contaminated system.

With the use of the correlation by Clift et al. [10] the largest mass transfer of oxygen is obtained. The coefficient proposed by Clift et al. [10] has the largest value for the coefficient. This will give the largest mass flux and following the largest oxygen transfer, as shown in Figure A.3.23. The correlation by Clift et al. [10] gives an approximately constant bubble size, seen in Figure 6.1.1. With the increasing bubble diameter for the coefficient by Brauer [7], the velocity increases over the column. The differences in bubble diameter result in different contact areas. Followingly the mass flux will not only differ due to different values for the mass transfer coefficient, but also due to different contact areas. Table 6.5.2 shows that the modeled mass transfer with use of coefficient by Clift et al. [10] is much higher than with the coefficient by Brauer [7].

Table 6.5.2: Oxygen and nitrogen transfer with various correlations for the mass transfer coefficient in a partly contaminated system.

System	Mass Transfer Coefficient	Oxygen transferred [%]	Nitrogen transferred [%]
Partly Contaminated	Brauer	21.3	15.8
Partly Contaminated	Clift	27.1	14.0

Contaminated System

Four different correlations for the mass transfer coefficient have been used in the simulations.

The oxygen transfer is approximately the same for the correlations by Brauer [7] and Hughmark [21]. The expressions for the coefficient by Bird et al. [3] and Fröessling [16] give approximately the same oxygen transfer. Nitrogen shows the oposite trend regarding mass transferred compared to the oxygen, as explained earlier.

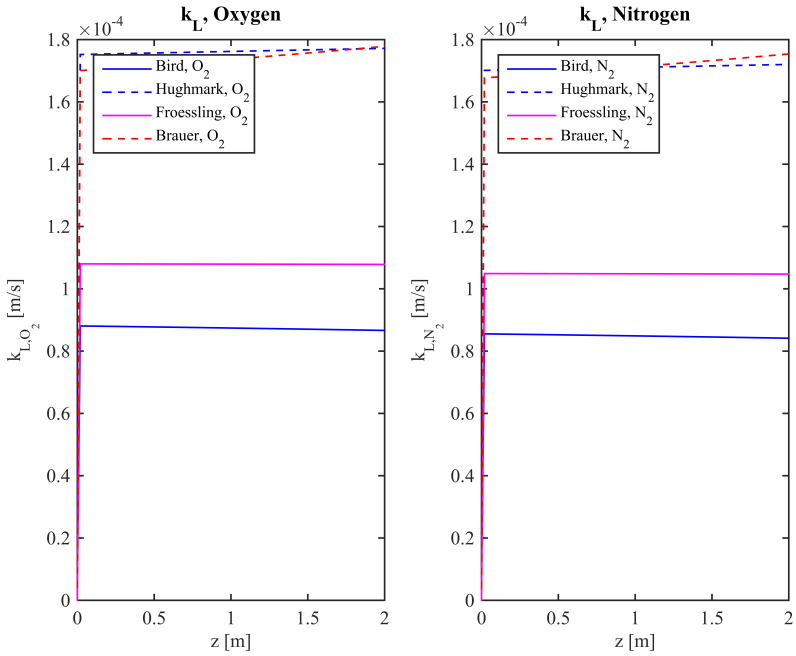

Figure 6.5.3: Mass transfer coefficients for oxygen and nitrogen for a contaminated system.

From Figure 6.5.3 it can be seen that the coefficient by Brauer [7] and Hughmark [21] are very similar. This explains the approximately equal mass transfer of oxygen. The deviations between the coefficient by Bird et al. [3] and that of Fröessling [16] explains the difference in mass transferred. It should be noted that the oxygen density profiles for Bird et al. [3] and Fröessling [16] are very similar.

The percentage transfer of oxygen and nitrogen for a contaminated system is given in table 6.5.3, where it can be seen that the oxygen mass transfer is very similar for the different coefficients.

Table 6.5.3: Oxygen and nitrogen transfer with various correlations for the mass transfer coefficient for a contaminated system.

System	Mass Transfer Coefficient	Oxygen transferred [%]	Nitrogen transferred [%]
Contaminated	Bird	18.9	15.9
Contaminated	Hughmark	21.3	15.2
Contaminated	Fröessling	19.5	15.7
Contaminated	Brauer	21.1	15.3

Additional profiles for the mass fractions, volume, and pressure for the clean, partly contaminated, and contaminated system are given in appendix A.3.

6.6 Conclusion Single Bubble

The rising bubble simulation results showed that the choice of mass transfer coefficient has a large significance on the behavior of the bubble. Especially for the clean and partly contaminated systems, the correlations gave large differences in the modeled mass transfer. It was found that for a contaminated system, the correlations implemented in the simulations gave very similar mass transfer. Using the same correlation as Brauer [7], resulted in the mass transfer being approximately equal, regardless of the system. This shows that choosing an improper mass transfer coefficient for a specific process can give very misleading information regarding the mass transfer. For the mass transfer coefficient in SCP production, experiments should be performed in order to find or derive a suitable correlation to be used for further modeling.

The mass transfer for varying and constant volume was found to be a approximately equal. Assuming constant volume can therefore be concluded to be a good approximation. It needs to be clarified that this is only stated to be a valid assumption in this specific bubble size range. For smaller or larger bubbles this may not be the case.

Based on the simulations with different correlations for the water systems, it is clear that a bad choice of mass transfer coefficient can give very misleading information of the mass transfer in a specific system. In section 6.1 it was stated that the mass transfer coefficient by Clift et al. [10] should be further investigated due to the opposite trend for the mass transfer of oxygen and nitrogen. From simulating the rising bubble with various correlations for the mass transfer coefficient, it was found that the coefficient giving the highest transfer of oxygen, gives the lowest transfer of nitrogen. There is no evident explanation to this trend, thus this should be prioritized for the investigation of the mass transfer coefficients.

The calculated values for mass transfer in the simulation results cannot be used in further work, due to the bubble area being implemented wrongly in MATLAB. However, the model itself is correct, and could be used as a basis when developing a correlation for the mass transfer coefficient for SCP production based on experimental data.

Chapter 7

Suggested Improvements

In this chapter possible further improvements of the bio-reactor and the model of single bubble rising in a column will be given.

Prediction of the Mass Transfer

To be able to model the mass transfer in the SCP production in more precise way, the accuracy in the mass transfer coefficient needs to be improved. Experiments should be performed of a single bubble rising in a column. The model of the single bubble in this work could be used as a basis when simulating the mass transfer. By measuring the concentration of the gas in the bubble at several points in the column, the mass transferred could be calculated. The simulation values should be compared to the experimental data. Several mass transfer correlations from the literature should be used in the model simulations. The choice of mass transfer coefficient will be based on the best fit between the simulation results and the experimental data. If none of the coefficients give representative simulation results compared to the experimental data, a new mass transfer coefficient needs to be derived. The experiment should be performed with different water qualities, mimicking that of a bio-reactor, such that the most proper mass transfer coefficient for SCP production is found.

Bubble size

In order to overcome the mass transfer limitations in the reactor it is necessary to keep the bubble size low. A relatively new method for ensuring small bubbles is to cut the bubbles by use of wire meshes. In the numerical study by **deen**, wire meshes in a micro-structured bubble column (MSBC) have been found to cut the bubbles into smaller ones and enhance surface renewal by deforming the bubbles. The wire-bubble interactions will enhance the interface dynamics and by the increased surface renewal rates give higher mass transfer coefficients. By introducing wire meshes in the reactor for SCP production the bubble sizes can be kept low and the mass transfer rates kept high over the column.

Distribution of Gas

The methane and oxygen concentration should be kept at a desired level at all times in order to obtain high biomass production. In the process plant at Tjeldbergodden and in the U-loop by UniBio, the gas is fed directly into the reactor at certain points in the reactor. Another suggested way of inserting methane is by using thin membrane tubes incorporated in the reactor column. This ensures that whenever the methane concentration decreases to an undesirable value, the concentration differences over the semipermeable membrane will cause the methane inside the tubes to transfer over to the reactor. In addition to obtaining sufficient amounts of methane in the reactor, this reduces the risks of explosion as the methane and oxygen is not inserted at the same points.

Model Improvements SCP

The present model for SCP production in this work contains various errors due to simplifications. In order to make the model more reliable the largest errors should be detected and reduced. In the present model the oxygen in gas phase and the water in liquid phase, is calculated by the other components. Further models should calculate the components independently.

To achieve a more accurate representation of the change in bubble size, the population balance taking into account the bubble breakage and coalescence, should be included in the SCP model. The change in the pressure dependent variables should be included, as the pressure changes from $4 - 3$ bar over the column

Bibliography

[1] Arild Johannessen, BioProtein AS by (2011). *Innspill til KD sin prosess for bioteknologistrategi*. City: Stavanger, Norway. [Norwegian][pdf][accessed 17-Nov-2016]. URL: https://www.regjeringen.no/globalassets/upload/kd/vedlegg/forskning/biotekkonferanse/iris_og_bioprotein_as.pdf.

[2] Bank, The World (2016). *New Data Reveals Uptick in Global Gas Flaring*. [accessed 14-June-2017]. URL: $http://www.worldbank.org/en/news/press-release/2016/12/12/new-data-reveals-uptick-in-global-gas-flaring$.

[3] Bird, R. B., Stewart, W. E., and Lightfoot, E.N. (2002). *Transport Phenomena, Second Edition*. John Wiley and Sons, Inc. ISBN: 0-471-41077-2.

[4] Bishof, F., Sommerfeld, M., and Durst, F. (1991). "The Determination of Mass Transfer Rates From Individual Small Bubbles". In: *Chemical Engineering Science* 46.12, pp. 3113–3121.

[5] Box, Engineering Tool. *Surface tension of water*. [accessed 14-Apr-2017]. URL: $http://www.engineeringtoolbox.com/surface-tension-d_962.html$.

[6] — *Thermal properties of water*. [accessed 14-Apr-2017]. URL: $http://www.engineeringtoolbox.com/water-thermal-properties-d_162.html$.

[7] Brauer, H. (1981). "Particle/fluid transport processes". In: *Prog. Chemical Engineering* 19, pp. 81–111.

[8] Cadogan, S. P., Maitland, G. C., and Trusler, J. P. Martin (2014). "Diffusion Coefficients of CO2 and N2 in Water at Temperatures between 298.15 K and 423.15 K at Pressures up to 45 MPa". In: *Journal of Chemical and Engineering Data* 59, pp. 519–525.

[9] Calderbank, P. H. and Moo-Young, M. B. (1960). "The continuous phase heat and mass-transfer properties of dispersion". In: *Chemical Engineering Science* 16, pp. 39–54.

[10] Clift, R., Grace, J.R., and Weber, M.E. (1978). *Bubbles, Drops and Particles*. Academic Press, Inc. ISBN: 0-12-176950-X.

[11] Cornell University, Department of MicrobiologyBinary (2016). *Fission and other Forms of Reproduction in Bacteria*. [accessed 11-Nov-2016]. URL: https://micro.cornell.edu/research/epulopiscium/binary-fission-and-other-forms-reproduction-bacteria.

[12] Doran, P. M. (2013). *Bioprocess Engineering Principles*. (2nd Edition). Elsevier Ltd.

[13] Eriksen, H., Strand, K., and Jørgensen, L. (2009). *Method of fermentation.* US Patent 7,579,163. URL: $http://www.google.com/patents/US7579163$.
[14] Ferrell, R. T. and Himmelblau, D. M. (1967). "Diffusion Coefficients of Nitrogen and Oxygen in Water". In: *Journal of Chemical and Engineering Data* 12, pp. 111–115.
[15] Fortescue, G. E. and Pearson, J. R. A. (1967). "On gas absorption into a turbulent liquid". In: *Chemical Engineering Science* 22, pp. 1163–1176.
[16] Fröessling, N. (1938). "Über die Verdunstung falender Tropfen". In: *Beitr Geophys* 52, pp. 170–216.
[17] Han, L., Fu, J., M.Li, S.Gong, Gao, N., C-Zhang, and H.Luo (2016). "A Theoretical Unsteady-State Model for kL of Bubbles Based on the Framework of Wide Energy Spectrum". In: *AIChE Journal* 62.4, 1007–1022. DOI: 10.1002/aic.15092.
[18] Han, P. and Bartels, D. M. (1996). "Temperature Dependence of Oxygen Diffusion in H2O and D2O†". In: *Journal of Physical Chemistry* 100, pp. 5597–5602.
[19] Heijnen, J.J. and Riet, K. Van'T (1984). "Mass Transfer, Mixing and Heat Transfer Phenomena in Low Viscosity Bubble Volumn Reactors". In: *The Chemical Engineering Journal* 28, B21–B42.
[20] Higbie, R. (1935). "The rate of absorption of a pure gas into a still liquid during short periods of exposure". In: *Trans AIChE* 31, 365–389.
[21] Hughmark, G.A. (1967). "Liquid-liquid Stray Column Drop Size, Holdup, and Continuous Phase Mass Transfer". In: *Ind. Eng. Chem. Fundamen* 6(3), pp. 408–413.
[22] Jakobsen, H.A. (2013). *Chemical Reactor Modeling, Second Edition.* Springer. ISBN: 978-3-319-05091-1. DOI: 10.1007/978-3-319-05092-8.
[23] Kestin, J, Sokolov, M, and Wakeham, W A (1978). "Viscosity of Liquid Water in the Range -8°C to 150°C". In: *J. Phys. Chem. Ref. Data* 7.3. DOI: 0047-2689/78/3121-0941.
[24] Larsen, E. B. (2011). *U-Shape And/or Nozzle U-Loop Fermenter And Method Of Fermentation.* US Patent App. 13/139,501. URL: http://www.google.com/patents/US20110244543.
[25] Lydersen, A. L. (1983). *Mass Transfer in Engineering Practice.* Wiley.
[26] Maier, R.M., Pepper, I.L., and Gerba, C.P. (2009). *Environmental Microbiology.* (2nd Edition). Elsevier Ltd.
[27] Morel, Christophe (2015). *Mathematical Modeling of Disperse Two-Phase Flows.* Springer. ISBN: 978-3-319-20103-0.

[28] Motarjemi, M. and Jameson, G.J (1978). "Mass Transfer From Very Small Bubbles - The Optimum Bubble Size for Aeration". In: *Chemical Engineering Science* 33, pp. 1415–1423.

[29] Olsen, D. F., Jørgensen, J. B., Villadsen, J., and Jørgensen, S. B. (2010). "Optimal Operating Points for SCP Production in the U-Loop Reactor". In: *Proceedings of the 9th International Symposium on Dynamics and Control of Process Systems (DYCOPS 2010)*.

[30] Prado-Rubio, O. A., Jørgensen, J. B., and Jørgensen, S. B. (2016). "Systematic Model Analysis for Single Cell Protein (SCP) Production in a U-Loop Reactor". In: *20^{th} European Symposium on Computer Aided Process Engineering - ESCAPE20, Elsevier B. V.*

[31] Rohatgi, A. URL: $http://arohatgi.info/WebPlotDigitizer/$.

[32] Rzehak, R. (2016). "Moldeling of mass-transfer in bubbly flows encompassing different mechanisms". In: *Chemical Engineering Science* 151, pp. 139–143.

[33] Sander, R. URL: $http://www.atmos-chem-phys.net/15/4399/2015/acp-15-4399-2015.pdf$.

[34] Sehabiague, L. and Morsi, B. (2013). "Modeling and Simulation of a Fischer–Tropsch Slurry Bubble Column Reactor Using Different Kinetic Rate Expressions for Iron and Cobalt Catalysts". In: *International Journal of Chemical Reactor Engineering* 11, 309–330. DOI: 10.1515/ijcre-2012-0017.

[35] Solsvik, J., Tangen, S., and Jakobsen, H. A. (2013). "Evaluation of weighted residual methods for the solution of the pellet equations: The orthogonal collocation, Galerkin, tau and least-squares methods". In: *Computers and Chemical Engineering* 58, pp. 223–259.

[36] Standards, NIST Chemistry WebBook (2016). [Chemical data online] National Institute of and Technology. [accessed 19-Jan-2017]. URL: $http://webbook.nist.gov/cgi/cbook.cgi?ID=C74828&Mask=1$.

[37] — [accessed 19-Jan-2017]. URL: $http://webbook.nist.gov/cgi/cbook.cgi?ID=C7782447&Mask=1$.

[38] — [accessed 19-Jan-2017]. URL: $http://webbook.nist.gov/cgi/cbook.cgi?ID=C7664417&Mask=1$.

[39] — [accessed 19-Jan-2017]. URL: $http://webbook.nist.gov/cgi/cbook.cgi?ID=C124389&Mask=1$.

[40] — [accessed 19-Jan-2017]. URL: $http://webbook.nist.gov/cgi/cbook.cgi?ID=C7732185&Type=JANAFL&Plot=on$.

[41] Swarnendu, R. and Jyeshtharaj, J. B. (2006). "Effect of Liquid Velocity on Axial Mixing in Gas-Liquid Dispersions: A CFD Simulation". In: *Journal*

of Chemical Technology and Biotechnology 29, pp. 1034–1041. DOI: 10.1002/ceat.200600154.

[42] Taweel, A. M. Al., Shah, Q., and Aufderheide, B. (2012). "Effect of Mixing on Microorganism Growth in Loop Bioreactors". In: *International Journal of Chemical Engineering*.

[43] UCLA. *http* : *//www.math.ucla.edu/ jteran/*270*b*.1.14*w/stability*$_a$*nd*$_c$*onditioning.pdf*.

[44] Vargaftik, N. B., Filippov, L. P., Tarzimanov, A. A., and Totskii, E. E. (1994). *Handbook of Thermal Conductivity of Liquids and Gases*. ISBN: 0849393450.

[45] Villadsen, J. (2002). "Bioprotein". In: *Dansk Kemi* 83.

[46] Witherspoon, P. A. and Saraf, D. N. (1965). "Diffusion of Methane, Ethane, Propane, and n-Butane in Water from 25 to 43°C". In: *The Journal of Physical Chemistry* 69.11, p. 3752.

[47] Wu, M., Huusom, J. K., Gernaey, K. V., and Krühne, U. (2016). "Modelling and Simulation of a U-loop Reactor for Single Cell Protein Production". In: *Proceedings of the 26th European Symposium on Computer Aided Process Engineering - ESCAPE 26, Elsevier B. V.*

Appendix A

Appendix

A.1 Contact Time and Turbulent Dissipation Energy

In this section the contact time for the different flow regimes and the turbulent dissipation energy will be outlined when surface renewal is dominated by small- and large eddies. The mass transfer coefficient is varying inversely of the root of the time of exposure and it is therefore common to refer to the inverse contact time. The contact times will be outlined, and the mass transfer coefficients for these regimes are found by inserting into the correlation for mass transfer obtained by Higbie [20]:

$$k_L \ \alpha \ \frac{2}{\pi^{1/2}}(D_A \tau_c^{-1})^{1/2} \tag{A.1.1}$$

where D_A denotes the diffusion coefficient of component A.

Inverse Contact time for Turbulent flow

For a turbulent flow the surface renewal will occur due to both small and/or large eddies. When modelling the mass transfer it is common to assume that either the small or the large eddies dominate the surface renewal. Depending on the assumptions there will be different expressions for the exposure time. It should be noted that there exist models where both the eddy-types are included, such a correlation is proposed by Han et al. [17].

Large Eddy Domination

Fortescue et al. [15] suggested based on dimension analysis that the largest eddies dominate the surface renewal with the following expression for the inverse contact time:

$$\tau_c^{-1} \ \alpha \ \frac{\epsilon}{\kappa} \tag{A.1.2}$$

where ϵ is the turbulent dissipation- and κ is the turbulent kinetic energy.

The turbulent dissipation energy can be related to the integral length scale, Λ, and the kinetic energy, where the integral length scale is given by:

$$\Lambda = \frac{\kappa^{3/2}}{\epsilon} \tag{A.1.3}$$

Solving for the dissipation energy the following relation is obtained:

$$\epsilon = \frac{\kappa^{3/2}}{\Lambda} \tag{A.1.4}$$

Inserting the relation for the dissipation energy (A.1.4) into equation (A.1.2) gives:

$$\tau_c^{-1} \; \alpha \; \frac{\kappa\kappa^{1/2}}{\kappa\Lambda} \; \alpha \; \frac{\kappa^{1/2}}{\Lambda} \tag{A.1.5}$$

It is necessary to find an expression for the turbulent kinetic energy. By dimension analysis the kinetic energy can be related to the second order velocity structure function, proposed by Kolmogorov [22]:

$$< [\delta v]^2 >= C_1(\epsilon\Lambda)^{2/3} = 2\epsilon^{2/3}\Lambda^{2/3} \tag{A.1.6}$$

where $C_1 \approx 2.0$ is the Kolmogorov parameter value.

In the book by Jakobsen [22], the second order velocity structure function is defined as the covariance of different velocities between two points in space.

By dimension analysis the following relation for the kinetic energy is obstained:

$$\kappa^{1/2} \approx< [\delta v]^2 >^{1/2} \approx 2^{1/2}\epsilon^{1/3}\Lambda^{1/3} \tag{A.1.7}$$

Inserting for equation (A.1.7) into equation (A.1.5) the inverse contact time for a large eddy dominated surface renewal can be expressed as:

$$\tau_c^{-1} \; \alpha \; \frac{\epsilon}{\kappa} \sim \frac{\kappa^{1/2}}{\Lambda} \sim \frac{2^{1/2}\epsilon^{1/3}}{\Lambda^{2/3}} \tag{A.1.8}$$

where ϵ is the turbulent dissipation energy, κ is the turbulent kinetic energy, and Λ is the integral length scale given in equation (A.1.3).

Small Eddy Domination

For small eddies dominating the surface renewal, the following correlation is used for the inverse time:

$$\tau_c^{-1} \ \alpha \ \left(\frac{\epsilon}{\nu}\right)^{1/2} \tag{A.1.9}$$

where ν is the kinematic viscosity of the liquid.

The contact time in equation A.1.9 is derived from the Kolmogorov's micro scale which is the smallest scale in turbulent flow.

Turbulent dissipation

In order to apply the surface renewal mass transfer models, an expression for the turbulent dissipation energy, ϵ, is needed in equation (A.1.8) and (A.1.9). Turbulence can be caused by various reasons, and in this case it has been assumed that wall friction is the only contributor to turbulence.

Turbulent Dissipation Energy by Wall Friction

In the following the turbulent dissipation energy will be derived when it has been assumed that wall friction is the only contributor to turbulence.

Jakobsen [22] stated that the global energy dissipation function can be approximated as:

$$\mu\phi_{eff}V \approx v_l A\Delta p \approx v_l \rho_l g \alpha_L H A \tag{A.1.10}$$

where μ is the kinematic viscosity, ϕ_{eff} is the effective global dissipation function, v_l is the liquid superficial velocity, H is the dispersion height, A is the cross sectional area of the column, $V = HA$ is the dispersion volume, and Δp is the pressure drop.

Dividing the dissipation function by the liquid mass results in the global specific energy dissipation rate:

$$\epsilon \approx \frac{\mu\phi_{eff}V}{m_L} \approx \frac{v_l A\Delta p_f}{\rho V} \approx \frac{v_l A(4f_F\rho\frac{L}{D_H}\frac{v_l^2}{2})}{\rho AL} \approx \frac{2v_l^3 f_F}{D_H} \tag{A.1.11}$$

where m_L is the total liquid mass and D_H is the hydraulic diameter.

In equation (A.1.11) the Darcy-Weisbach relation for the pressure has been used, which is given as:

$$\Delta p_f = 4f_F\rho\frac{Lv_l^2}{2D} \tag{A.1.12}$$

where f_F is the Fanning friction factor, L is the length of the tube and D is the column diameter.

f_F in equation (A.1.12) is the Fanning friction factor where Blasius' correlation for Darcy's friction factor, f_D, has been used [22].

The Fanning friction factor is given as:

$$f_F = \frac{f_D}{4} \tag{A.1.13}$$

The Blasius' correlation for the Darcy's friction factor is given by:

$$f_D = \frac{0.316}{Re^{1/4}} \tag{A.1.14}$$

where Re is Reynolds number. The Blasius correlation applies to fully turbulent flows and low gas fractions [32].

It should be noted that the relation for the pressure drop in equation (A.1.12) is valid for duct flows, i.e. the column diameter, D, can be replaced by the hydraulic diameter, D_H, and is valid for both laminar and turbulent flow.

The turbulent dissipation can be further extended:

$$\epsilon \approx \frac{2v_l^3 f_F}{D_H} \approx \frac{2v_l^3 f_F}{Re_c \frac{\nu}{v_l}} \approx \frac{2v_l^4 f_F}{Re_c \nu} \approx \frac{2Re_c^4 \nu^4 f_F}{Re_c \nu D_H^4} \approx \frac{2Re_c^3 \nu^3 f_F}{D_H^4} \approx 0.16 Re_c^{2.75} \left(\frac{\nu^3}{D_H^4}\right) \tag{A.1.15}$$

where Re_c is the column Reynold's number. This relation for the turbulent dissipation energy is based on the wall friction being the only contributor to turbulence.

Now that expressions for both the inverse contact time and the turbulent dissipation energy are known, the mass transfer coefficients for the small and large eddy model can be derived.

Mass Transfer Dominated by Large Eddies

In the following, it is assumed that the large eddies dominate the interfacial renewal and equation (A.1.15) is a proper representation of the dissipation energy. Inserting the dissipation energy in equation (A.1.15) into the expression for the inverse contact time given in (A.1.8) gives:

$$\tau_c^{-1} \; \alpha \; \frac{2^{1/2}\epsilon^{1/3}}{\Lambda^{2/3}} \sim \frac{2^{1/2}}{(0.2d_c)^{2/3}} \left(\frac{0.16 Re_c^{2.75} \nu^3}{d_c^4} \right)^{1/3} \sim \frac{2^{1/2} 0.16^{1/3} Re_c^{2.75/3} \nu}{0.2^{2/3} d_c^2} \tag{A.1.16}$$

Inserting τ_c^{-1} in equation (A.1.16) into equation (A.1.1) gives:

$$k_L \; \alpha \; \frac{2}{\pi^{1/2}} (D_A \tau_c^{-1})^{1/2} \tag{A.1.17}$$

$$\sim \frac{2}{\pi^{1/2}} \left(\frac{D_A 2^{1/2} 0.16^{1/3} Re_c^{2.75/3} \nu}{0.2^{2/3} d_c^2} \right)^{1/2} \tag{A.1.18}$$

$$\sim 1.7 \frac{(D_A \nu)^{1/2}}{d_c} \left(\frac{v_l d_c}{\nu} \right)^{0.46} \tag{A.1.19}$$

Mass Tranfer Dominated by Small Eddies

For the assumption of the small eddies dominating to the interfacial renewal, the dissipation energy (A.1.15) is inserted into (A.1.9):

$$\tau_c^{-1} \; \alpha \; \frac{\epsilon}{\kappa} \sim \left(\frac{0.16 Re_c^{2.75} \nu^3}{d_c^4 \nu} \right)^{1/2} \sim \frac{0.16^{1/2} Re_c^{2.75/2} \nu}{d_c^2} \tag{A.1.20}$$

The mass transfer coefficient for the small eddies assumption is obtained by inserting equation (A.1.20) into (A.1.1):

$$k_L \; \alpha \; \frac{2}{\pi^{1/2}} (D_A \tau_c^{-1})^{1/2} \tag{A.1.21}$$

$$\sim \frac{2}{\pi^{1/2}} \left(\frac{D_A 0.16^{1/2} Re_c^{2.75/2} \nu}{d_c^2} \right)^{1/2} \tag{A.1.22}$$

$$\sim \frac{2}{\pi^{1/2}} (D_A \nu)^{1/2} \frac{0.16^{1/4}}{d_c} \left(\frac{v_l d_c}{\nu} \right)^{2.75/4} \tag{A.1.23}$$

$$\sim 0.71 \frac{(D_A \nu)^{1/2}}{d_c} \left(\frac{v_l d_c}{\nu} \right)^{0.69} \tag{A.1.24}$$

A.2 SCP Production

Original Values

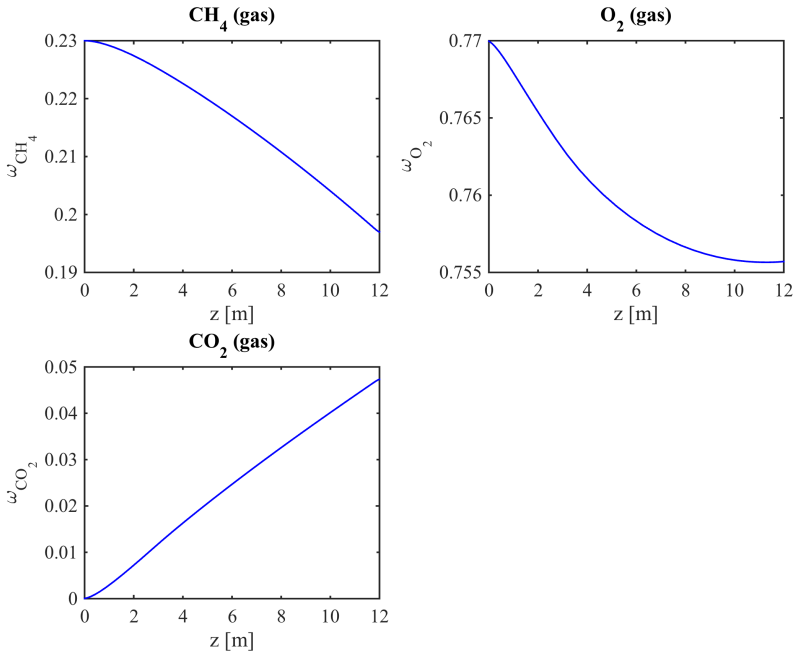

Figure A.2.1: Mass fractions of the components in gas phase with the initial values based on the values by Taweel et al. [42] and Larsen [24].

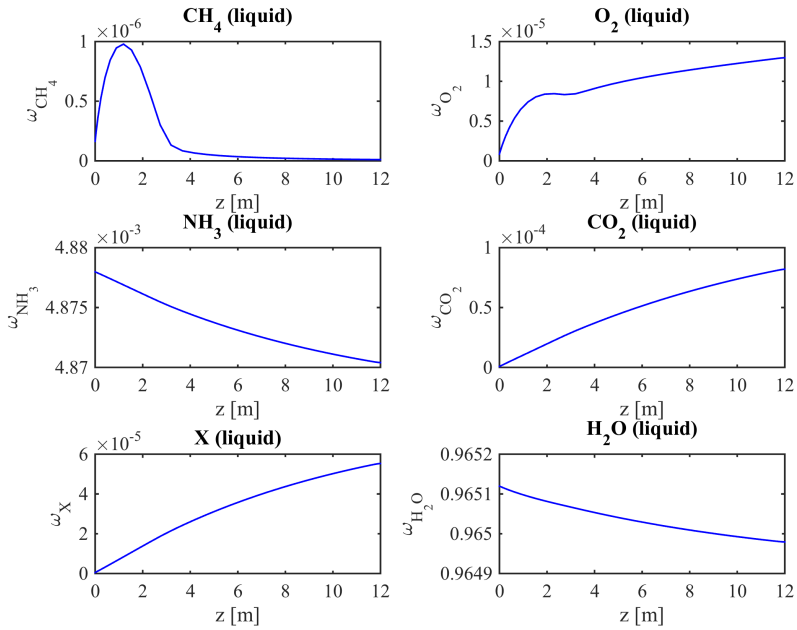

Figure A.2.2: Mass fractions of the components in liquid phase with the initial values based on the values by Taweel et al. [42] and Larsen [24].

Turbulent Flow

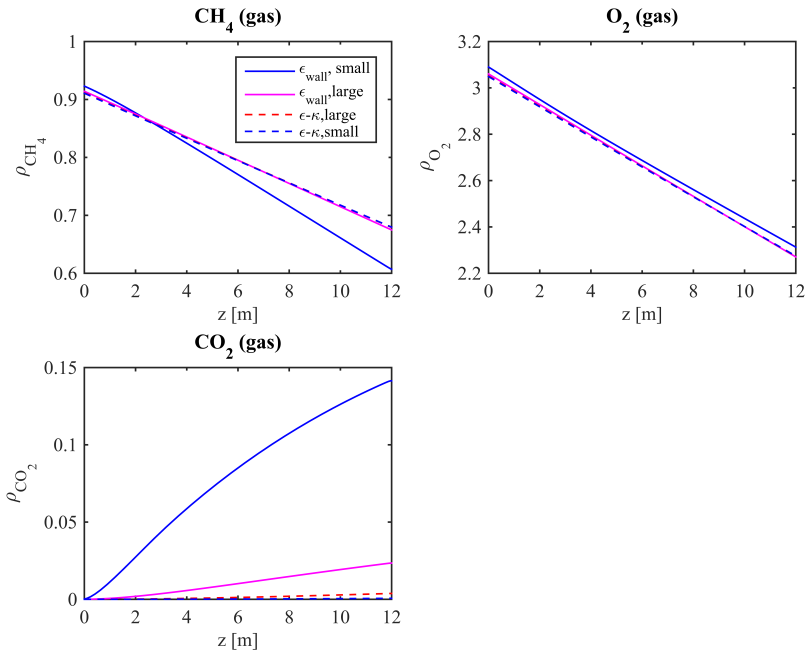

Figure A.2.3: Change in gas density of the components with varying mass transfer coefficient for turbulent flow.

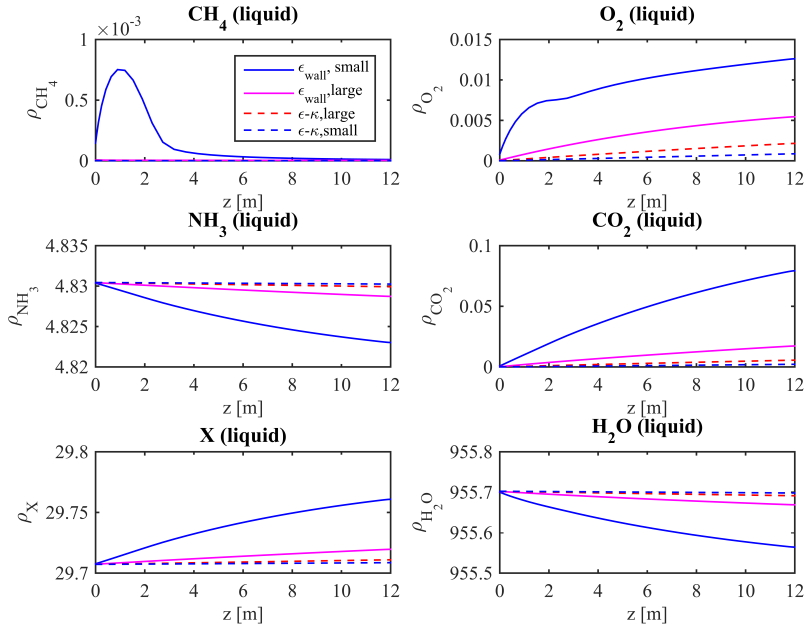

Figure A.2.4: Change in liquid density of the components with varying mass transfer coefficient for turbulent flow

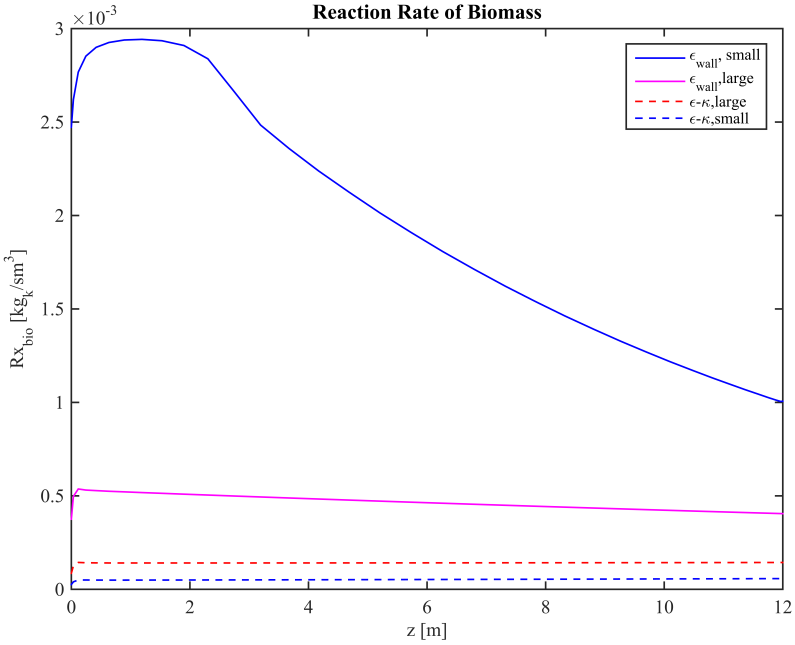

Figure A.2.5: Reaction rate of biomass with varying mass transfer coefficient for turbulent flow

A.3 Additional Figures Single Bubble

Oxygen and Nitrogen

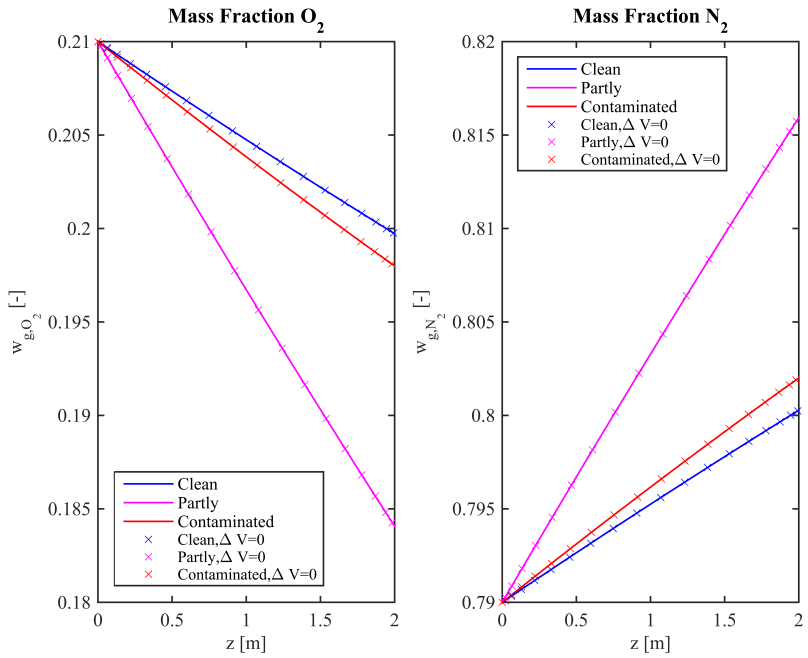

Figure A.3.1: Mass fractions for a bubble containing initially 21% oxygen and 79% nitrogen, for constant and varing volume.

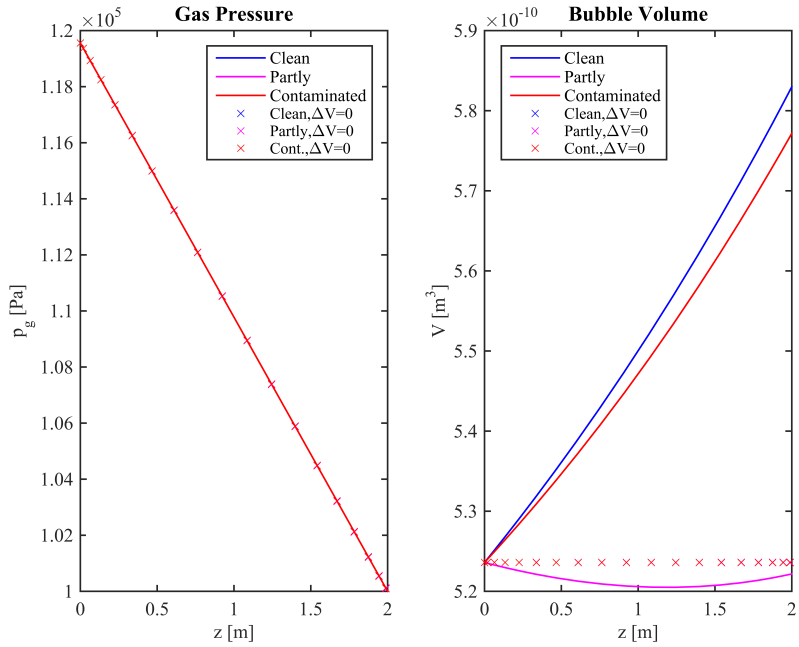

Figure A.3.2: Pressure and volume change over the column for a bubble containing initially 21% oxygen and 79% nitrogen, for constant and varing volume.

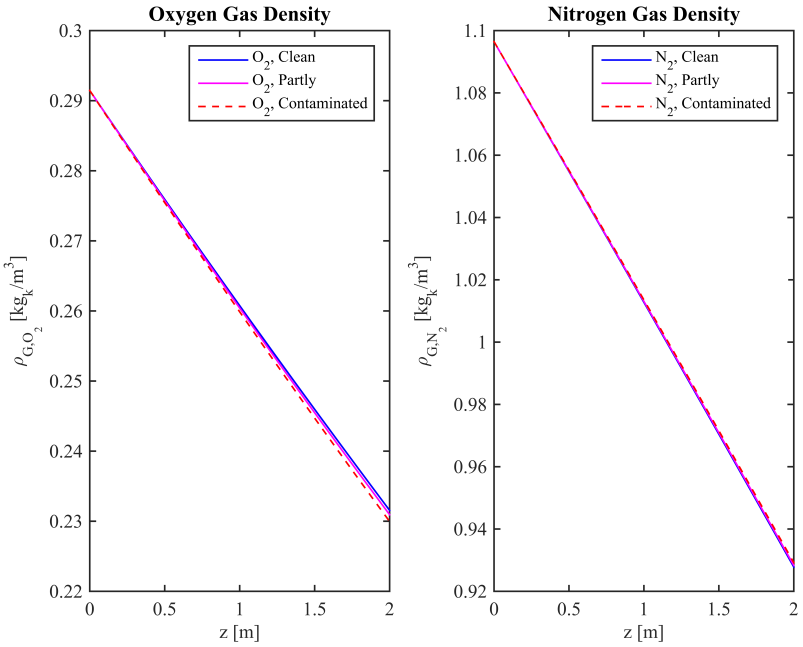

Figure A.3.3: Component densities in gas phase with use of correlation by Brauer [7] for the mass transfer coefficient. The same coefficient is used on all the systems.

Methane and Nitrogen

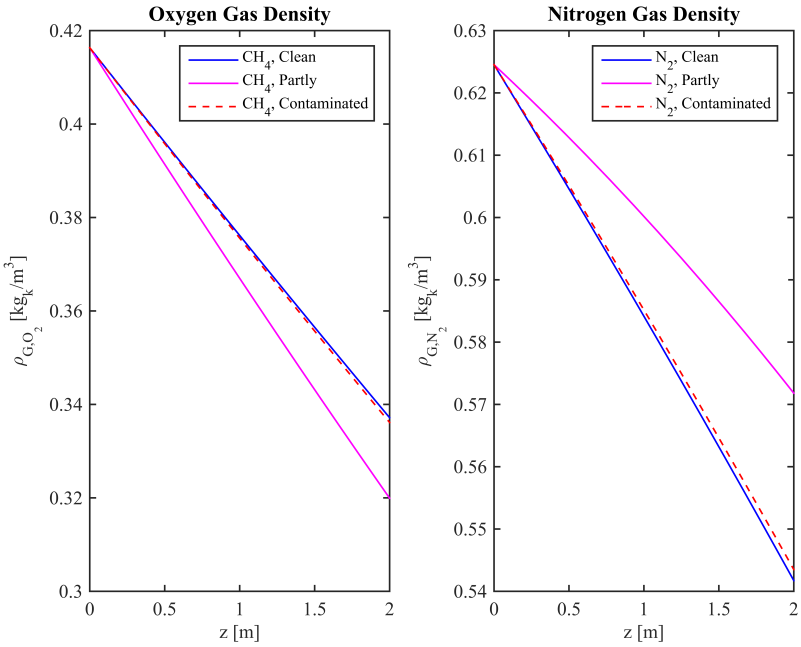

Figure A.3.4: Component gas densities for a bubble containing initially 40% methane and 60% nitrogen for varying water systems.

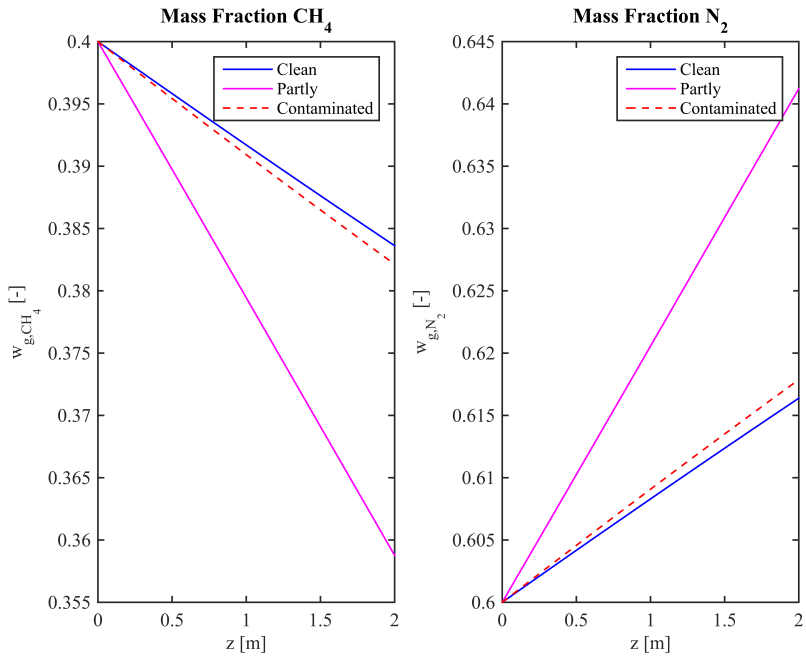

Figure A.3.5: Mass fractions for a bubble containing initially 40% methane and 60% nitrogen for varying water systems.

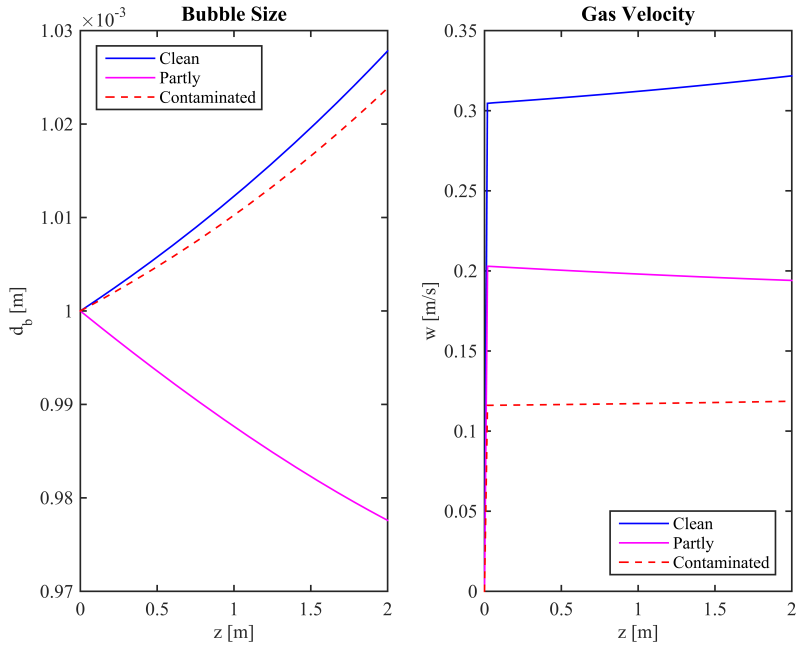

Figure A.3.6: Change in the bubble diameter and velocity for a bubble containing initially 40% methane and 60% nitrogen for varying water systems.

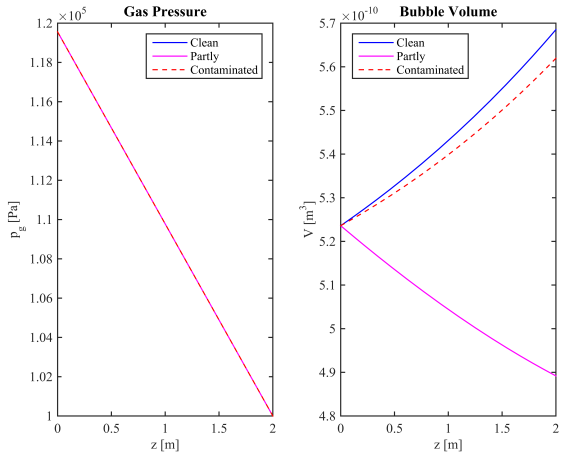

Figure A.3.7: Change in bubble volume and gas pressure over the column for a bubble containing initially 40% methane and 60% nitrogen for varying water systems.

Carbon dioxide and Nitrogen

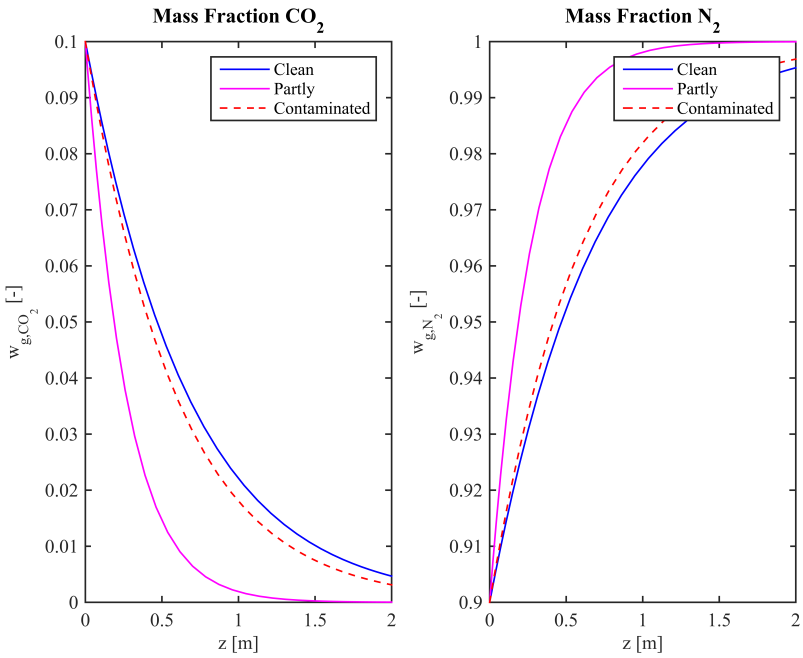

Figure A.3.8: Mass fractions for a bubble containing initially 10% carbon dioxide and 90% nitrogen for varying water systems.

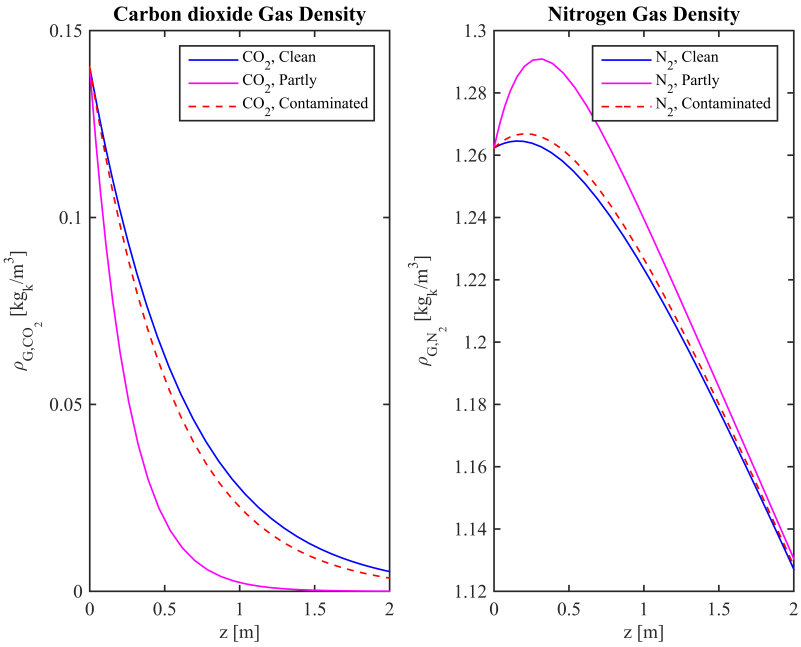

Figure A.3.9: Component gas densities for a bubble containing initially 10% carbon dioxide and 90% nitrogen for varying water systems.

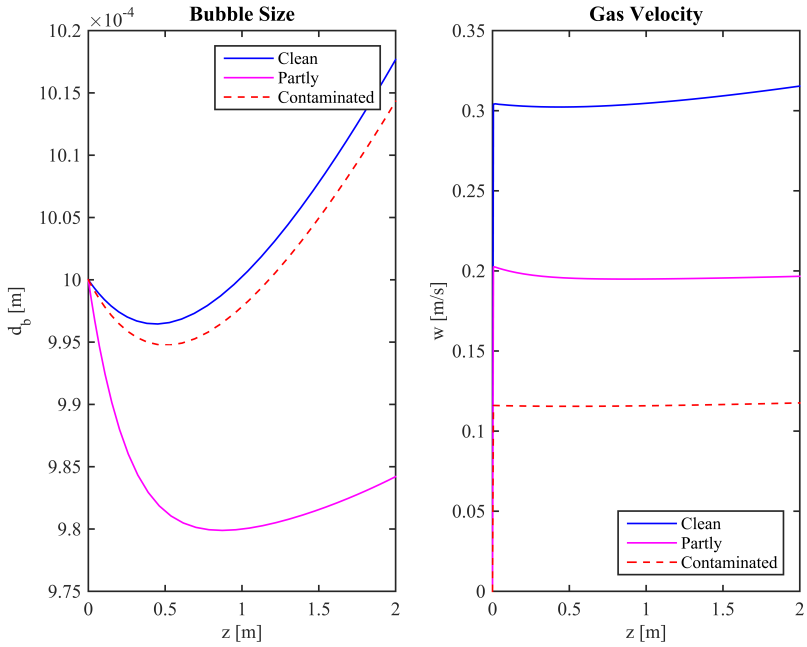

Figure A.3.10: Mass fractions for a bubble containing initially 10% carbon dioxide and 90% nitrogen for varying water systems.

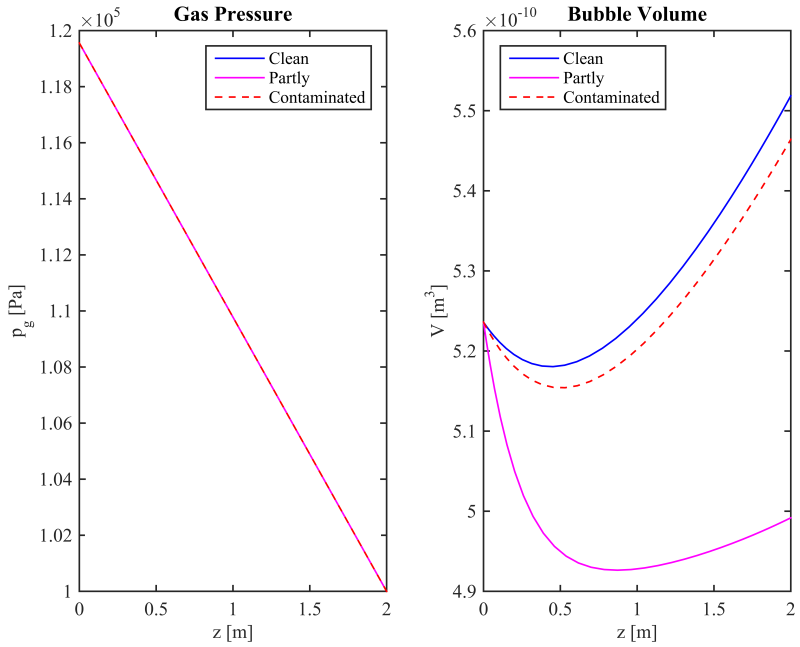

Figure A.3.11: Mass fractions for a bubble containing initially 10% carbon dioxide and 90% nitrogen for varying water systems.

Equal Correlation for $\mathbf{k}_L$

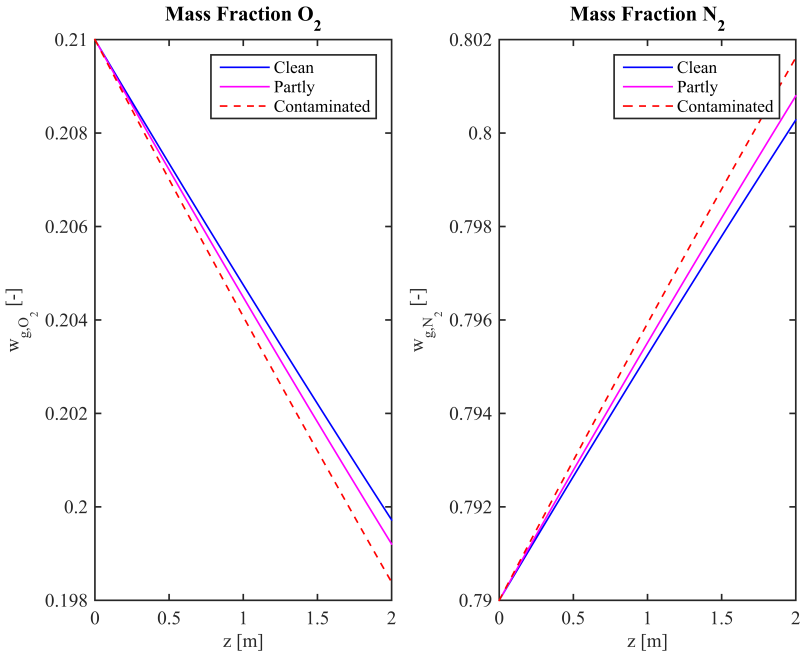

Figure A.3.12: Mass fractions in gas phase with use of the same mass transfer coefficient for all systems.

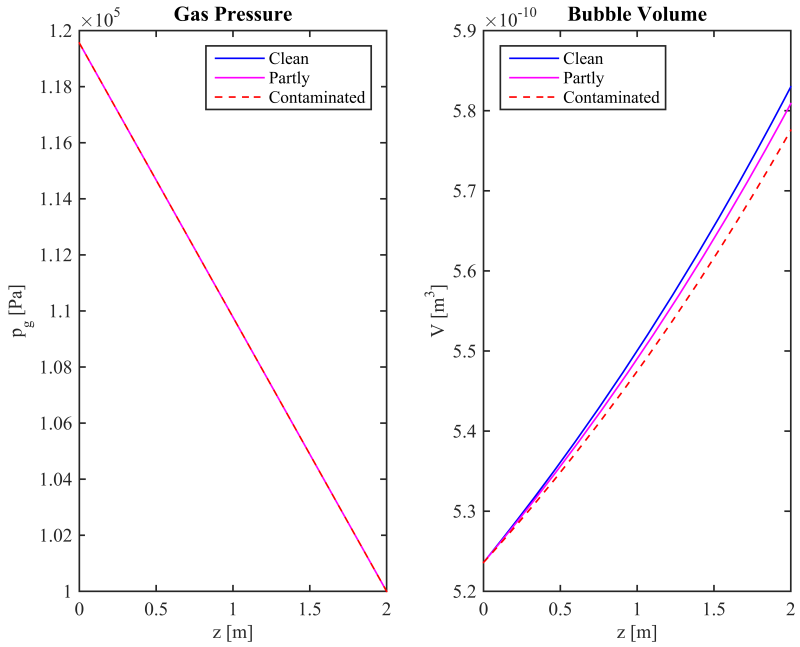

Figure A.3.13: Change in volume and pressure with use of the same mass transfer coefficient for all systems.

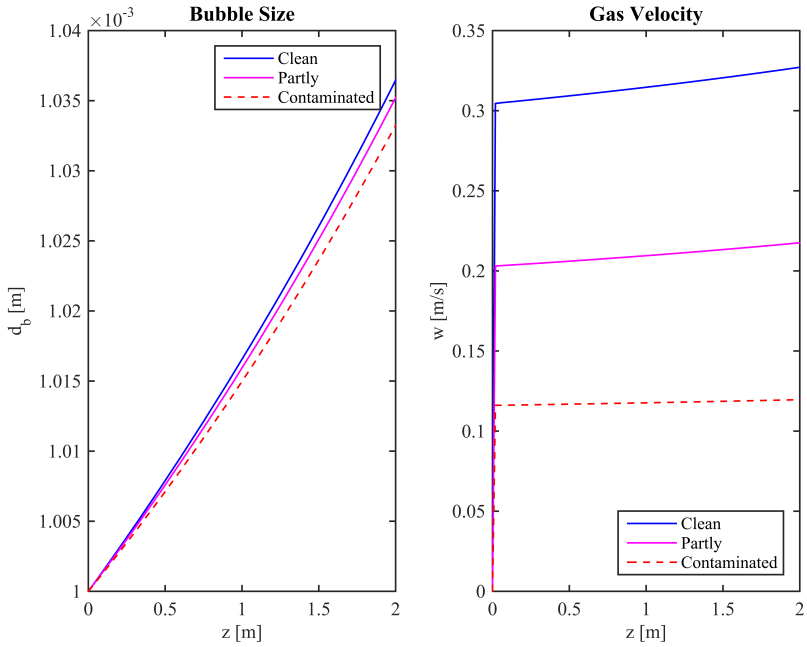

Figure A.3.14: Velocity and bubble diameter with use of the same mass transfer coefficient for all systems.

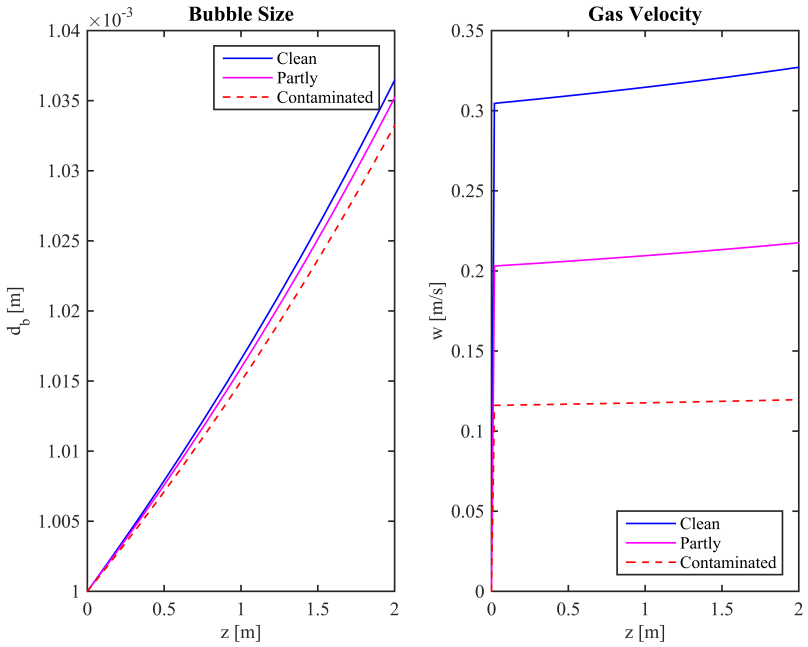

Figure A.3.15: Mass transfer coefficient for oxygen and nitrogen with use of the same mass transfer coefficient for all systems.

Water Saturated with Carbon dioxide

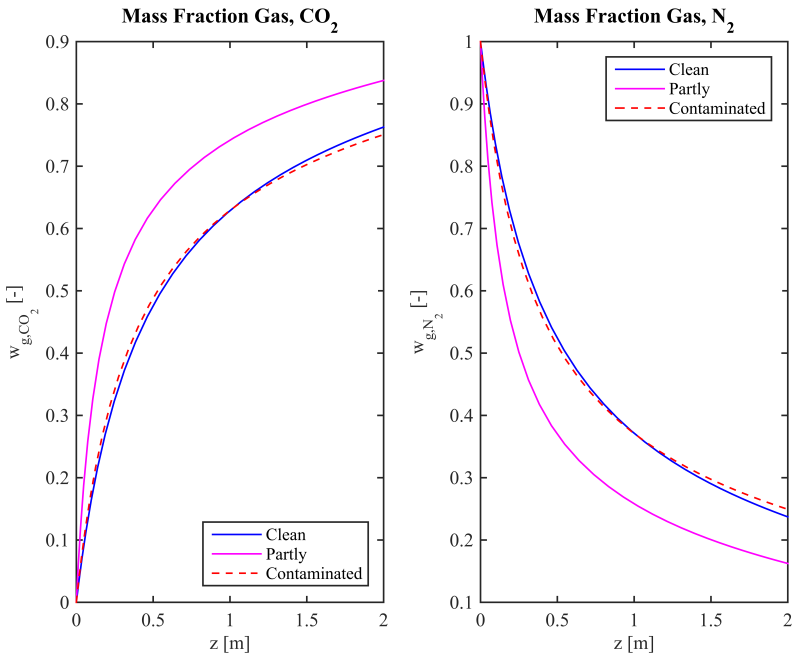

Figure A.3.16: Mass fractions in the gas phase for bubble containing initially 100% nitrogen, rising a carbon dixoxide saturated water.

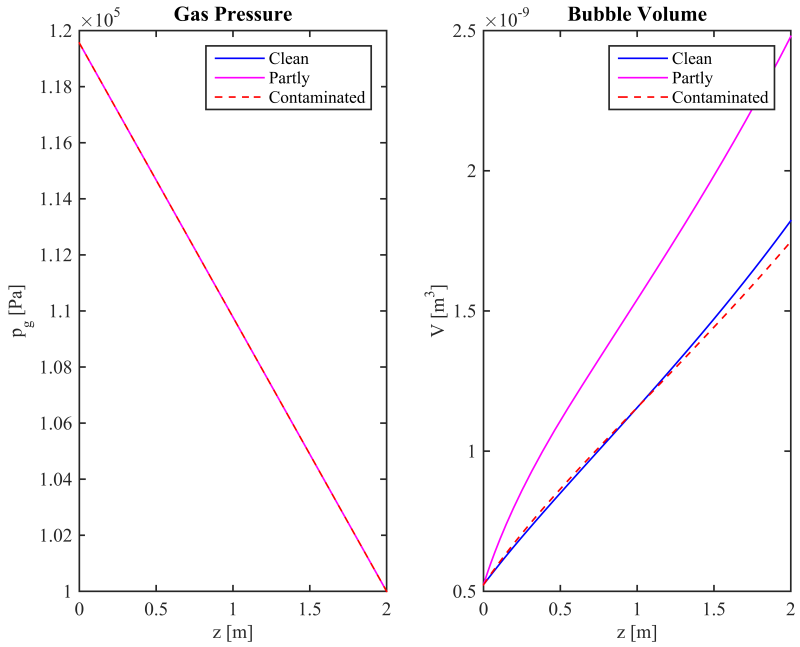

Figure A.3.17: Pressure and volume profiles for bubble containing initially 100% nitrogen, rising a carbon dixoxide saturated water.

Various Mass Transfer Coefficients

Clean

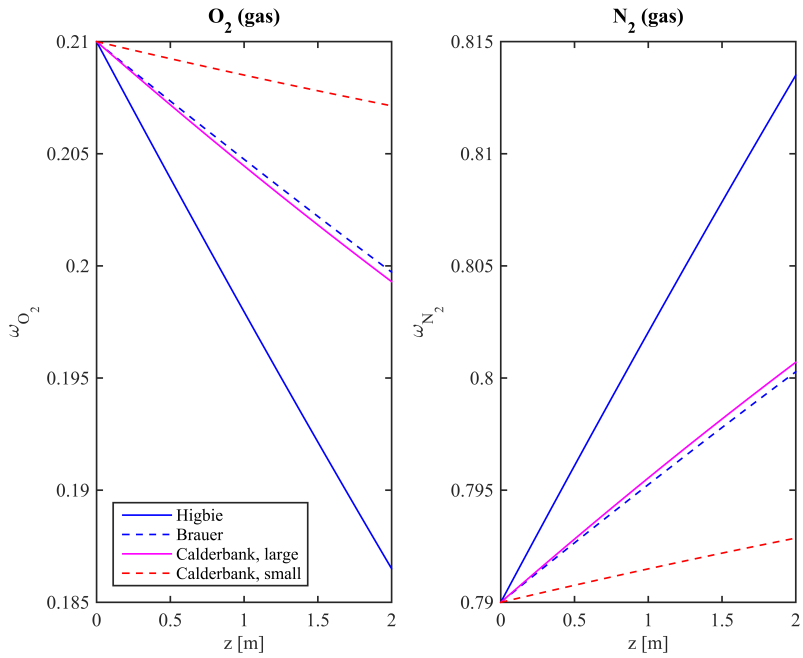

Figure A.3.18: Mass fractions of the gas phase with use of different mass transfer coefficients for a clean system.

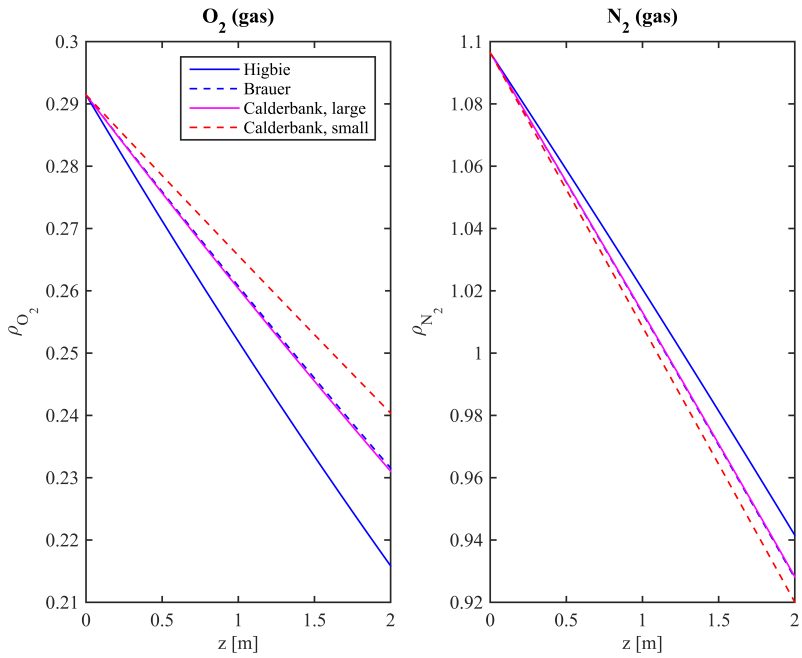

Figure A.3.19: Component gas density with use of different mass transfer coefficients for a clean system.

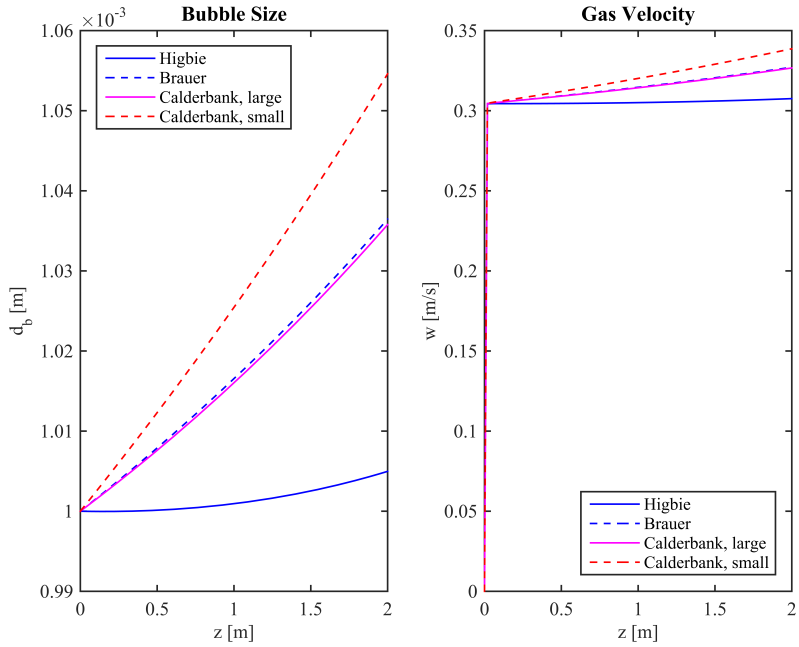

Figure A.3.20: Change in velocity in bubble size with use of different mass transfer coefficients for a clean system..

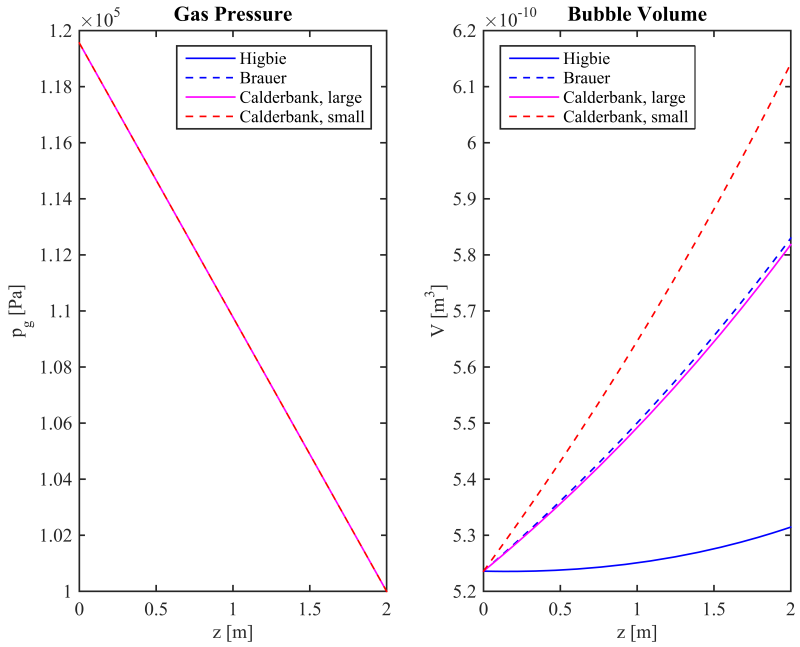

Figure A.3.21: Volume and pressure profiles with use of different mass transfer coefficients for a clean system.

Partly Contaminated

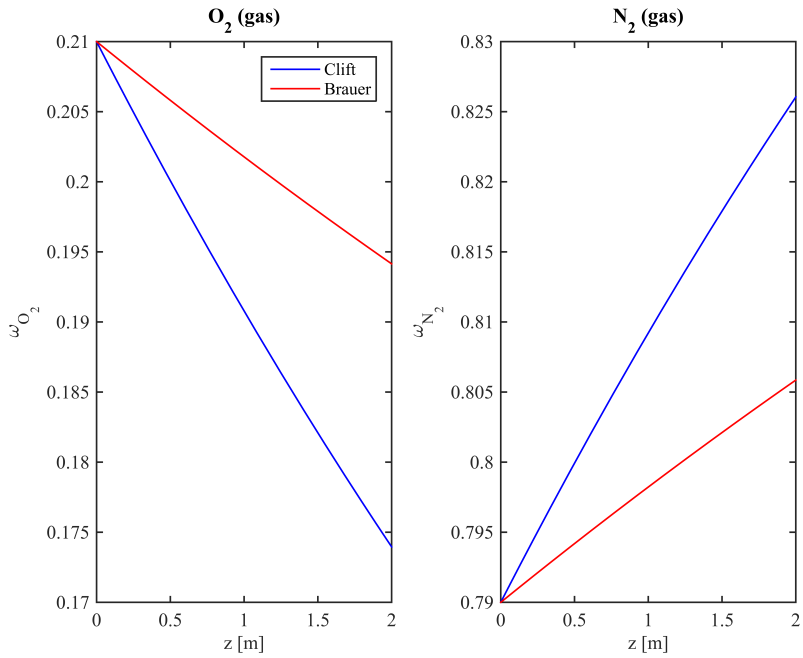

Figure A.3.22: Mass fractions of the gas phase with use of different mass transfer coefficients for a partly contaminated system.

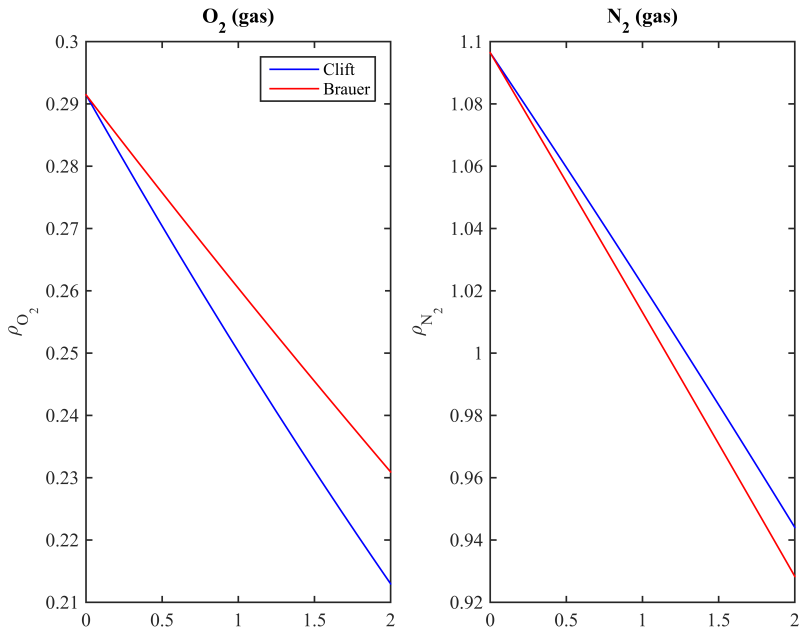

Figure A.3.23: Component gas density with use of different mass transfer coefficients for a partly contaminated system.

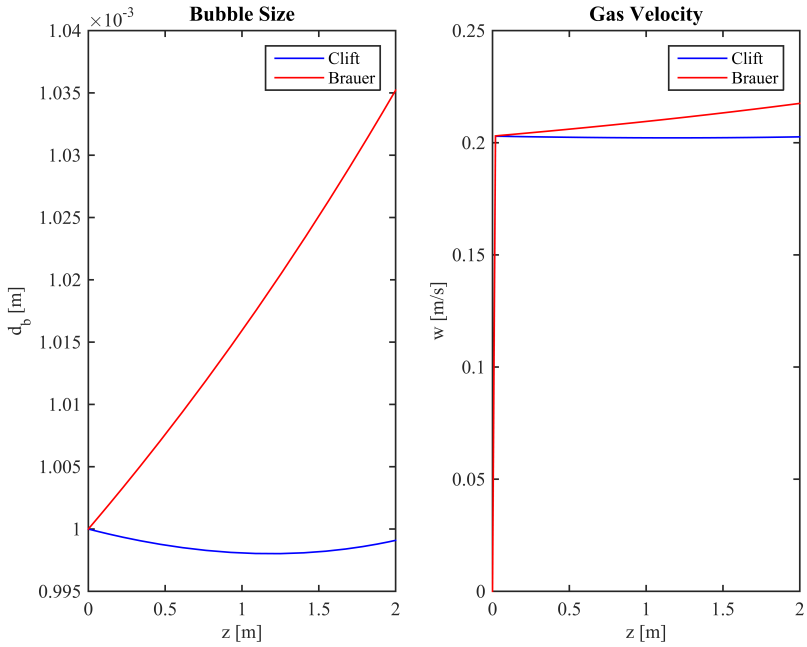

Figure A.3.24: Change in velocity in bubble size with use of different mass transfer coefficients for a partly contaminated system.

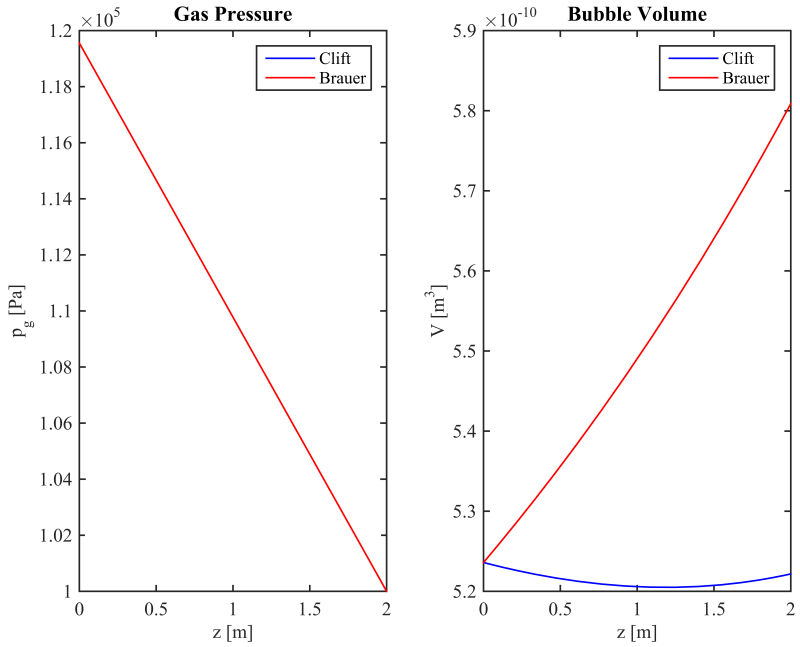

Figure A.3.25: Volume and pressure profiles with use of different mass transfer coefficients for a partly contaminated system.

Contaminated

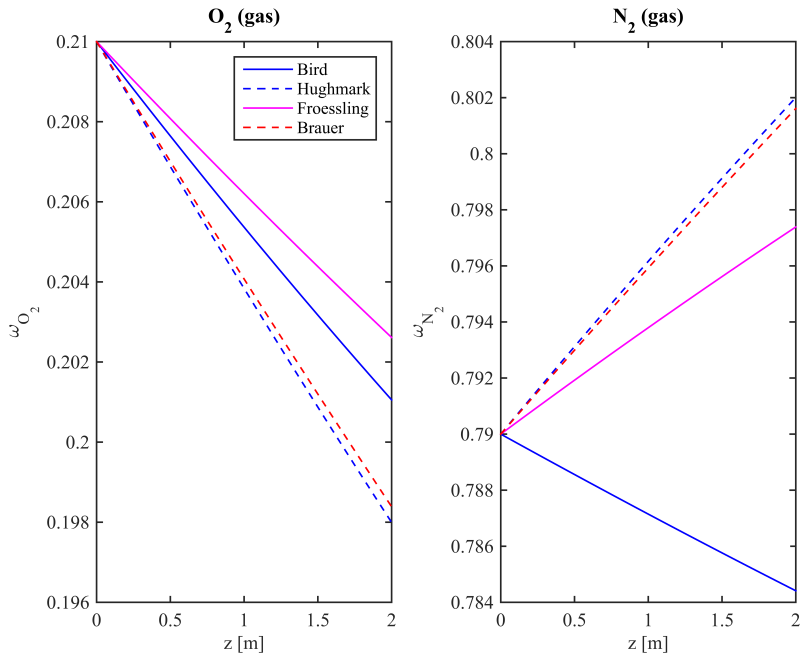

Figure A.3.26: Mass fractions of the gas phase with use of different mass transfer coefficients for a contaminated system.

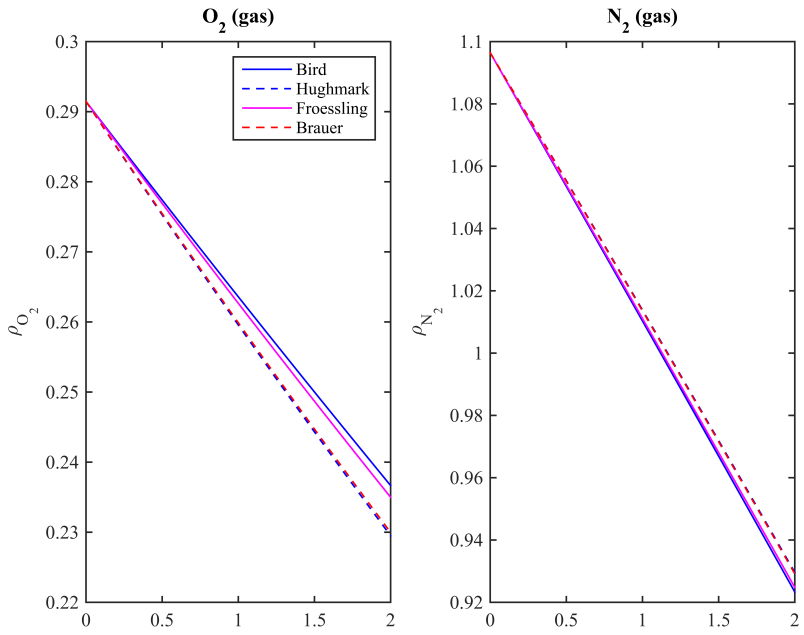

Figure A.3.27: Component gas density with use of different mass transfer coefficients for a contaminated system.

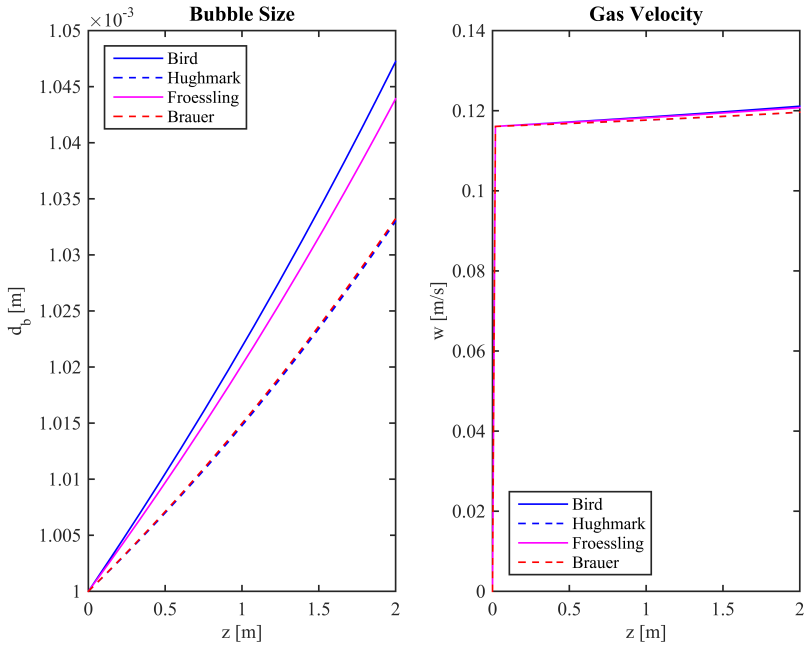

Figure A.3.28: Change in velocity in bubble size with use of different mass transfer coefficients for a contaminated system.

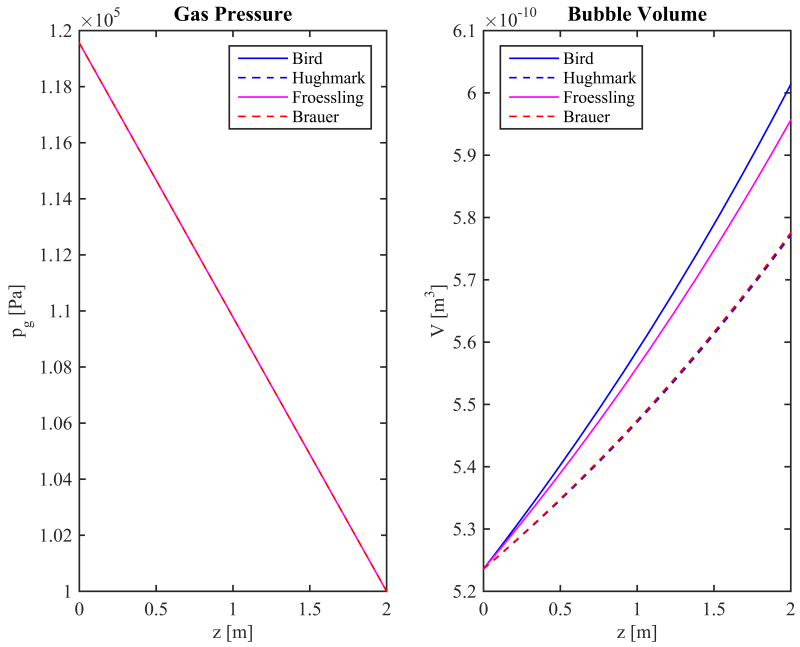

Figure A.3.29: Volume and pressure profiles with use of different mass transfer coefficients for a contaminated system.

A.4 Henry's Law on Mass Basis

On a mass basis the equilibrium can be derived by starting out with the following equation:

$$y_{i,G}p_T = H_i C^*_{i,L} = H_i \frac{n_i}{V} = H_i \frac{m_i}{M_i V} = H_i \frac{\rho^*_{i,L}}{M_i} \tag{A.4.1}$$

The mole fraction can in terms of mass fraction be expressed as:

$$y_{i,G} = \frac{\frac{m_i}{M_i}\frac{1}{m_{tot}}}{\sum_i \frac{m_i}{M_i}\frac{1}{m_{tot}}} \tag{A.4.2}$$

where equation A.4.2 has been multiplied by $1/m_{tot}$ in the numerator and denominator to obtain the mass fraction.

$$y_{i,G} = \frac{\frac{w_i}{M_i}}{\sum_i \frac{w_i}{M_i}} \tag{A.4.3}$$

Insert equation A.4.3 into equation A.4.1 to obtain the equilibrium liquid density of component i:

$$\rho^*_{i,L} = \frac{w_{i,G} p_G \bar{M}}{H_i} \tag{A.4.4}$$

where the mean molar mass $\bar{M}$ is given as:

$$\bar{M} = \frac{1}{\sum_i \frac{w_i}{M_i}} \tag{A.4.5}$$

A.5 Mass Flux

The rate of mass transfer for a component A, N_A, over a gas boundary layer can be given as:

$$N_A = k_g a(C_{A,g} - C_{A,g,i}) \tag{A.5.1}$$

where k_g is the gas-side mass transfer coefficient, a is the gas-liquid interfacial area per unit volume of fluid, $C_{A,g}$ is the concentration of component A in the gas phase, and $C_{A,g,i}$ is the gas concentration at the interface.

For a component A, the rate of mass transfer over a liquid boundary layer can be expressed by:

$$N_A = k_L a(C_{A,L,i} - C_{A,L}) \tag{A.5.2}$$

where k_L is the liquid-side mass transfer coefficient, $C_{A,L}$ is the liquid bulk concentration of component A and $C_{A,L,i}$ is the liquid concentration of A at the interface.

If we assume that the gas and the liquid are in equilibrium at the interface, then we have the following relation:

Assuming the gas and the liquid to be at equilibrium at the interface the following relation between the gas and liquid concentration is valid:

$$C_{A,g,i} = H_A C_{A,L,i} \tag{A.5.3}$$

where H_A is Henry's constant.

Combine equation A.5.1 and A.5.2 and relate the gas and liquid concentrations through equation A.5.3:

$$N_A \left(\frac{1}{k_g a} + \frac{H_A}{k_L a} \right) = C_{A,g} - H_A C_{A,L} \tag{A.5.4}$$

or

$$N_A \left(\frac{1}{H_A k_g a} + \frac{1}{k_L a} \right) = \frac{C_{A,g}}{H_A} - C_{A,L} \tag{A.5.5}$$

The overall gas-phase mass transfer coefficient, K_G, can be expressed as:

$$\frac{1}{K_G a} = \frac{1}{k_g a} + \frac{H_A}{k_L a} \tag{A.5.6}$$

The overall liquid-phase mass transfer coefficient, K_L, can be give as:

$$\frac{1}{K_L a} = \frac{1}{H_A k_g a} + \frac{1}{k_L a} \tag{A.5.7}$$

By this it follows that the rate of mass transfer in gas-liquid systems can be written as:

$$N_A = K_G a(C_{A,g} - H_A C_{A,L}) \tag{A.5.8}$$

or

$$N_A = K_L a\left(\frac{C_{A,g}}{H_A} - C_{A,L}\right) \tag{A.5.9}$$

If the main resistance lies in either the gas-phase or the liquid-phase interfacial film, equation A.5.8 and A.5.9 can be simplified. For a component A that is very soluble in the liquid, there will only be a small resistance over the liquid-phase interfacial film and $k_l a$ in equation A.5.6 becomes large. $K_G a$ is approximately equal to $k_g a$ and the mass flux can be expressed as:

$$N_A = k_g a(C_{A,g} - C^*_{A,g}) \tag{A.5.10}$$

where $C^*_{A,g} = H_A C_{A,L}$ is the hypothetical gas concentration that would be in equilibrium with the liquid bulk. For a component A that is poorly soluble in the liquid, the resistance over the gas-phase interfacial film will be small, and $k_g a$ in equation A.5.6 becomes large. $K_L a$ is then approximately equal to $k_l a$ and the mass flux can be expressed as:

$$N_A = k_L a(C^*_{A,L} - C_{A,L}) \tag{A.5.11}$$

where $C^*_{A,L} = C_{A,g}/H_A$ is the hypothetical liquid concentration that would be in equilibrium with the gas bulk.

A.6 Constants SCP

Table A.6.1: Ammonia mineral salt solution. The table is adapted from Eriksen et al. [13].

Component	Mg per liter
NH_3	10
MgH_3PO_4	75
$MgSO_4 \cdot 7H_2O$	380
$CaCl_2 \cdot 2H_2O$	100
K_2SO_4	200
$FeSO_4 \cdot 7H_2O$	75
$CuSO_4 \cdot 5H_2O$	1
$ZnSO_4 \cdot 7H_2O$	0.96
$CoCl_2 \cdot 6H_2O$	0.12
$MnCl_2 \cdot 4H_2O$	0.048
H_3BO_3	0.036
$NiCl_2 \cdot 6H_2O$	0.024
$NaMoO_4 \cdot 2H_2O$	0.0012

Table A.6.2: Yield coefficients and molar masses of each component.

Component i	Y_{iX} mol(i)mol$(X)^-1$	$M_w \cdot 10^3$ kgmol$^-1$
CH_4	-1.000/0.52	16.04
O_2	-1.454/0.52	32.00
NH_3	-0.104/0.52	17.03
CO_2	0.480/0.52	44.01
H_2O	1.688/0.52	18.02
X	1.000	24.63

Table A.6.3: Specific heat capacities, $c_i = a + bT \cdot 10^{-3} + cT^2 \cdot 10^{-3} + dT^3 \cdot 10^{-3}$, [Jmol^{-1}°K^{-1}]

Component i	a	$b \cdot 10^2$	$c \cdot 10^5$	$d \cdot 10^9$	Source
CH_4	-0.703	108.47	-42.52	5.863	[36]
O_2	31.32	-20.235	57.86	-36.51	[37]
NH_3	19.99	49.771	-15.38	-15.38	[38]
CO_2	24.99	55.187	-33.69	7.945	[39]
H_2O	-203.6	1523.3	-3196	2474	[40]
BIO	-203.6	1523.3	-3196	2474	[40]

Note: The specific heat capacity of biomass is assumed to be that of water.

Table A.6.4: Henry's constant for components interacting in gas-liquid mass transfer [42].

Component i	$H \cdot 10^{-2}$ m^{3}Pa mol^{-1}
CH_4	1000.9
O_2	1199.81
CO_2	47.39

Table A.6.5: Molecular diffusivity of component i in water at $T = 45$°C for components interacting in gas-liquid mass transfer.

Component i	$D_m \cdot 10^9$ m^{2}s^{-1}	Source
CH_4	2.41	Witherspoon et al. [46]
O_2	3.05	Han et al. [18]
CO_2	3.50	Cadogan et al. [8]
N_2	3.47	Han et al. [18]

Table A.6.6: Properties of water at $T = 45°\text{C}$ and $p = 3$ bar.

Property	Value	Unit	Source
ρ_{H_2O}	990.24	kgm^{-3}	Kestin et al. [23]
μ_{H_2O}	$5.96{\cdot}10^{-4}$	Pa·s	Kestin et al. [23]
λ_{H_2O}	0.638	$\text{WK}^{-1}\text{m}^{-1}$	Vargaftik et al. [44]

A.7 Constants Single Bubble

Table A.7.1: Diffusion coefficients for gases in water at 25° C.

Solute	$D_{AB} \cdot 10^9$ [m^2/s]	Source
Carbon dioxide	1.92	Lydersen [25]
Methane	1.89	Witherspoon et al. [46]
Oxygen	2.10	Lydersen [25]
Nitrogen	2.01	Ferrell et al. [14]

Table A.7.2: Henry's constant for components interacting in gas-liquid mass transfer [33].

Component i i	$H \cdot 10^{-2}$ $\text{m}^3\text{Pa mol}^{-1}$
CH_4	714
O_2	769
CO_2	29
N_2	1562.5

Table A.7.3: Properties of water at $T = 25°C$ and $p = 1$ bar.

Property	Value	Unit
ρ_{H_2O}	997.1 [5]	kgm^{-3}
μ_{H_2O}	$8.9{\cdot}10^{-4}$ [5]	Pa·s
σ_{H_2O}	0.072 [6]	Nm^{-1}

A.8 Leibniz Rule and Gauss Theorem for a Volume Integral

The following theorems are found in the book of [27].

The Leibniz theorem of a surface can be given as:

$$\frac{d}{dt}\int_V f dv = \int_V \frac{\partial F}{\partial t} dv + \int_A f \underline{\mathrm{v}}_A \cdot \underline{\mathrm{n}} dA \tag{A.8.1}$$

where $\underline{\mathrm{n}}$ is a unit vector, f is any function, $\underline{\mathrm{v}}_A$ is the speed, V is the volume, and A is the surface.

Gauss theorem on a volume integral can be given by:

$$\int_V \Delta f dv = \int_A f \underline{\mathrm{n}} da \tag{A.8.2}$$

where f is a scalar.

$$\int_V \Delta \underline{\mathrm{u}} dv = \int_A \underline{\mathrm{n}} \cdot \underline{\mathrm{u}} da \tag{A.8.3}$$

where $\underline{\mathrm{u}}$ is a vector.

The continuity is given by the following equation:

$$\frac{d\rho_k}{dt} + \Delta \cdot (\rho_k \underline{\mathrm{v}}_k) = 0 \tag{A.8.4}$$

where k is the phase.

A.9 Modeling Equations Single Bubble

A.9.1 Total Mass

Start out with the total mass:

$$m(t) = \int_V \rho_d dv \tag{A.9.1}$$

where m is the total mass of the gas bubble, ρ_d is the density of the dispersed phase and V is the volume of the dispersed phase.

Using the Leibniz rule A.8.1, the following equation is obtained:

$$\frac{dm}{dt} = \frac{d}{dt}\int_V \rho_b dv = \int_V \frac{d\rho_d}{dt} dv + \oint_S \rho_d \underline{\mathrm{v}}_d \cdot \underline{\mathrm{n}}_d + \oint_S \rho_b (\underline{\mathrm{v}}_I - \underline{\mathrm{v}}_b) \cdot n_b dS \quad \text{(A.9.2)}$$

where v_I is the velocity at the interface, v_b is the velocity of the bubble, n_b is a unit vector normal to the interface, and $\oint_S$ is the surface integral of the bubble. The mass flux can be expressed as:

$$\dot{m}_b = \rho_d (\underline{\mathrm{v}}_I - \underline{\mathrm{v}}_b) \quad \text{(A.9.3)}$$

As the velocity at the interface is unknown (A.9.44) it replaced with:

$$\dot{m}_b = \sum_k k_L (\rho^*_{l,k} - \rho_{l,k}) \quad \text{(A.9.4)}$$

Using Gauss theorem for a scalar A.8.2 on the second term in equation (A.9.44), and the continuity equation A.8.4, equation (A.9.46) reduces to:

$$\frac{dm}{dt} = \oint_S \dot{m}_b dS \quad \text{(A.9.5)}$$

where it has been assumed that there is uniform density inside the bubble. If there is assumed to be no concentration gradients along the surface equation (A.9.47) becomes:

$$\frac{d}{dt}(\rho_b V) = -\dot{m}_b A \quad \text{(A.9.6)}$$

$$V\frac{d\rho_g}{dt} + \rho_g \frac{dV}{dt} = -\dot{m}_b A \quad \text{(A.9.7)}$$

where the relation $m_b = \rho_b V$ has been used, and it has been assumed that the gas leaves the bubble.

Assume ideal gas, $PV = nRT$:

$$V = \frac{mRT}{\bar{M}_g p_g} \quad \text{(A.9.8)}$$

Taking the derivative of the volume in equation (A.9.8) gives:

$$\frac{dV}{dt} = \frac{d}{dt}\left(\frac{mRT}{\bar{M}_g p_g}\right) \tag{A.9.9}$$

$$= RT\left[\frac{1}{\bar{M}_g p_g}\frac{dm_g}{dt} + \frac{m_g}{\bar{M}_g}\left(\frac{-1}{p_g^2}\right)\frac{dp_g}{dt} + \frac{m_g}{p_g}\left(\frac{-1}{\bar{M}_g{}^2}\right)\frac{d\bar{M}_g}{dt}\right] \tag{A.9.10}$$

$$= RT\left[\frac{1}{\bar{M}_g p_g}\left(V\frac{d\rho_g}{dt} + \rho_g\frac{dV}{dt}\right) - \frac{m_g}{\bar{M}_g p_g^2}\frac{dp_g}{dt} - \frac{m_g}{p_g\bar{M}_g{}^2}\right] \tag{A.9.11}$$

$$\frac{dV}{dt}\left(1 - \frac{\rho_g RT}{\bar{M}_g p_g}\right) = \frac{RTV}{\bar{M}_g p_g}\frac{d\rho_g}{dt} - \frac{\rho_g V RT}{\bar{M}_g p_g^2}\frac{dp_g}{dt} - \frac{\rho_g V RT}{p_g\bar{M}_g{}^2}\frac{d\bar{M}_g}{dt} \tag{A.9.12}$$

$$\tag{A.9.13}$$

Insert equation (A.9.8) for the gas density on the left hand side in equation (A.9.12) leaves the left hand side to equal to zero. Solving for the gas density results in the following equation:

$$\frac{d\rho_g}{dt} = \frac{\bar{M}_g}{RT}\frac{dp_g}{dt} + \frac{p_g}{RT}\frac{d\bar{M}_g}{dt} \tag{A.9.14}$$

Inserting equation (A.9.14) into equation (A.9.7) gives the following equation for the change in volume over time:

$$\rho_g\frac{dV}{dt} = -\dot{m}_b A - V\left[\frac{\bar{M}_g}{RT}\frac{dp_g}{dt} + \frac{p_g}{RT}\frac{d\bar{M}_g}{dt}\right] \tag{A.9.15}$$

$$= -\sum_k\left(\frac{k_{L,k}w_{k,g}p_g\bar{M}_g}{H_k} - \rho_l w_{A,l}\right)A - V\left[\frac{\bar{M}_g}{RT}\frac{dp_g}{dt} + \frac{p_g}{RT}\frac{d\bar{M}_g}{dt}\right] \tag{A.9.16}$$

If it is assumed that the concentration of component k in the liquid phase is negligible equation A.9.15 reduces to:

$$\rho_g\frac{dV}{dt} = -\sum_k\frac{k_{L,k}w_{k,g}p_g\bar{M}_g}{H_k}A - V\left[\frac{\bar{M}_g}{RT}\frac{dp_g}{dt} + \frac{p_g}{RT}\frac{d\bar{M}_g}{dt}\right] \tag{A.9.17}$$

where the change in gas pressure over time is given by:

$$\frac{dp_g}{dt} = -\rho_l g \frac{dx}{dt} \tag{A.9.18}$$

The change in length over time is expressed as:

$$\frac{dx}{dt} = v \tag{A.9.19}$$

where x is the length and v is the velocity.

A.9.2 Species Mass Balance

Start out with the mass of component A:

$$m_A(t) = \int_V \rho_{A,d} dv \tag{A.9.20}$$

where m_A is the mass of component A, $\rho_{A,d}$ is the density of component A, and V is the volume of the dispersed phase.

Using the Leibniz rule A.8.1, the following equation is obtained:

$$\frac{dm_A}{dt} = \frac{d}{dt}\int_V \rho_{A,b} dv = \int_V \frac{\rho_{A,b}}{dt} dv + \oint_S \rho_{A,b} \underline{\mathrm{v}}_d \cdot \underline{\mathrm{n}}_d + \oint_S \rho_{A,b}(\underline{\mathrm{v}}_I - \underline{\mathrm{v}}_b) \cdot n_b dS \tag{A.9.21}$$

where v_I is the velocity at the interface, v_b is the velocity of the bubble, n_b is a unit vector normal to the interface, and $\oint_S$ is the surface integral of the bubble.

The mass flux of component A can be expressed as:

$$\dot{m}_A = \rho_{A,b}(\underline{\mathrm{v}}_I - \underline{\mathrm{v}}_b) \tag{A.9.22}$$

As for the total mass the velocity at the interface is unknown. Equation (A.9.22) can be replaced by:

$$\dot{m}_A = k_{L,A}(\rho^*_{A,l} - \rho_{A,l}) \tag{A.9.23}$$

Using Gauss theorem for a scalar A.8.2 on the second term in equation (A.9.44), and the continuity equation A.8.4, equation (A.9.46) reduces to:

$$\frac{dm_A}{dt} = \oint_S \dot{m}_A dS \tag{A.9.24}$$

where it has been assumed that there is uniform density inside the bubble. If there is assumed to be no concentration gradients along the surface equation (A.9.24) becomes:

$$\frac{d}{dt}\left(\rho_{A,g}V\right) = -\dot{m}_A A \tag{A.9.25}$$

$$V\rho_g\frac{dw_{A,g}}{dt} + Vw_{A,g}\frac{d\rho_g}{dt} + \rho_g w_{A,g}\frac{dV}{dt} = -\dot{m}_A A \tag{A.9.26}$$

Inserting equation (A.9.15) into equation (A.9.25):

$$V\rho_g\frac{dw_{A,g}}{dt} + Vw_{A,g}\frac{d\rho_g}{dt} + \rho_g w_{A,g}\left(\frac{-\dot{m}_g A}{\rho_g} - \frac{V}{\rho_g}\frac{d\rho_g}{dt}\right) = -\dot{m}_A A \tag{A.9.27}$$

$$V\rho_g\frac{dw_{A,g}}{dt} + Vw_{A,g}\frac{d\rho_g}{dt} - w_{A,g}\dot{m}_g A - w_{A,g}V\frac{d\rho_g}{dt} = -\dot{m}_A A \tag{A.9.28}$$

$$\tag{A.9.29}$$

Solve for the mass fraction of component A gives:

$$V\rho_g\frac{dw_{A,g}}{dt} = -\left(\frac{k_{L,A}w_{A,g}p_g\bar{M}_g A}{H_k} - \rho_l w_{A,l}\right) + w_{A,g}\dot{m}_b A \tag{A.9.30}$$

For an assumption of negligible concentration of component A in the liquid phase, equation A.9.30 reduces to:

$$V\rho_g\frac{dw_{A,g}}{dt} = -\frac{k_{L,A}w_{A,g}p_g\bar{M}_g A}{H_k} + w_{A,g}\dot{m}_b A \tag{A.9.31}$$

The total mass flux can be given by equation A.9.45

A.9.3 Momentum Balance

The time derivative of the momentum, using the Leibniz rule is given by:

$$\frac{d(m_g w_g)}{dt} = \frac{d}{dt}\int_V \rho_d \underline{\mathrm{v}}_d dv = \int_V \frac{\partial \rho_d \underline{\mathrm{v}}_d}{\partial t}dv + \oint_S \rho_d \underline{\mathrm{v}}_d \underline{\mathrm{v}}_d \cdot n_d dS + \oint_S \rho_d \underline{\mathrm{v}}_d(\underline{\mathrm{v}}_I - \underline{\mathrm{v}}_d)\cdot n_d dS \tag{A.9.32}$$

Using Gauss theorem for a vector A.8.3 on the second term in equation (A.9.44), and the continuity equation A.8.4, equation (A.9.46) reduces to:

$$\frac{d(m_g w_g)}{dt} = -m_g g + \oint_S (\dot{m}_g \underline{\mathrm{v}}_g + \sigma_g \cdot n_g) dS \tag{A.9.33}$$

where σ_g includes all the forces in addition to the gravity, and the positive direction is directed upwards, i.e. negative sign for the gravity.

Assuming uniform density inside the bubble and no concentration gradients along the surface, equation (A.9.33) becomes:

$$\frac{d(m_g w_g)}{dt} = -m_g g - \dot{m}_g \underline{\mathrm{v}}_g A + (F_D + F_B) A \tag{A.9.34}$$

where $m_g g$ express the gravity force, F_D is the drag forces, and F_B the bouyancy forces, $v_g = w_g$, and the gas moves out of the bubble.

The drag forces are given by:

$$F_D = \frac{1}{2} C_D \rho_l |w_r| w_r A \tag{A.9.35}$$

where the relative velocity, w_r, is given by:

$$w_r = w_g - w_l \tag{A.9.36}$$

The bouyancy forces are given by:

$$F_B = V \rho_l g \tag{A.9.37}$$

Inserting the expressions for the drag and bouyancy forces gives:

$$\rho_g V \frac{d\underline{\mathrm{w}}_g}{dt} + V \underline{\mathrm{w}}_g \frac{d\rho_g}{dt} + \rho_g \underline{\mathrm{w}}_g \frac{dV}{dt} = -m_g g - \dot{m}_g \underline{\mathrm{w}}_g A + V \rho_l g - \frac{1}{2} C_D \rho_l \underline{\mathrm{w}}_g |\underline{\mathrm{w}}_r| A \tag{A.9.38}$$

The expression for the time derivative of the volume given by equation (A.9.15) is inserted into equation (A.9.38) to obtain:

$$\frac{d\underline{\mathrm{w}}_g}{dt} = -\frac{\underline{\mathrm{w}}_g}{V}\frac{dV}{dt} - \frac{\underline{\mathrm{w}}_g}{\rho_g}\frac{d\rho_g}{dt} - g - \frac{\dot{m}_g\underline{\mathrm{w}}_g A}{V\rho_g} + \frac{\rho_l}{\rho_g}g - \frac{1}{2}\frac{C_D\rho_l\underline{\mathrm{w}}_g|\underline{\mathrm{w}}_r|A}{V\rho_g} \quad \text{(A.9.39)}$$

$$= -\frac{\underline{\mathrm{w}}_g}{V}\left[\frac{-\dot{m}_g A}{\rho_g} - \frac{V}{\rho_g}\frac{d\rho_g}{dt}\right] - \frac{\underline{\mathrm{w}}_g}{\rho_g}\frac{d\rho_g}{dt} - g - \frac{\dot{m}_g\underline{\mathrm{w}}_g A}{V\rho_g} + \frac{\rho_l}{\rho_g}g - \frac{1}{2}\frac{C_D\rho_l\underline{\mathrm{w}}_g|\underline{\mathrm{w}}_r|A}{V\rho_g} \quad \text{(A.9.40)}$$

$$= \frac{\dot{m}_g\underline{\mathrm{w}}_g A}{V\rho_g} - g - \frac{\dot{m}_g\underline{\mathrm{w}}_g A}{V\rho_g} + \frac{\rho_l}{\rho_g}g - \frac{1}{2}\frac{C_D\rho_l\underline{\mathrm{w}}_g|\underline{\mathrm{w}}_r|A}{V\rho_g} \quad \text{(A.9.41)}$$

$$= -g + \frac{\rho_l}{\rho_g}g - \frac{1}{2}\frac{C_D\rho_l\underline{\mathrm{w}}_g|\underline{\mathrm{w}}_r|A}{V\rho_g} \quad \text{(A.9.42)}$$

A.9.4 Bubble Diameter

It should be noted that the bubble diameter can be found directly from the bubble volum, $V = d_b^3\pi/6$, when the volume is known.

Start out with the total mass:

$$m(t) = \int_V \rho_d dv \quad \text{(A.9.43)}$$

where m is the total mass of the gas bubble, ρ_d is the density of the dispersed phase and V is the volume of the dispersed phase.

The mass flux can be expressed as:

$$\dot{m}_b = \rho_d(\underline{\mathrm{v}}_I - \underline{\mathrm{v}}_b) \quad \text{(A.9.44)}$$

As the velocity at the interface is unknown (A.9.44) it replaced with:

$$\dot{m}_b = \sum_k k_L(\rho^*_{l,k} - \rho_{l,k}) \quad \text{(A.9.45)}$$

Using the Leibniz rule A.8.1, the following equation is obtained:

$$\frac{dm}{dt} = \frac{d}{dt}\int_V \rho_b dv = \int_V \frac{d\rho_d}{dt}dv + \oint_S \rho_d\underline{\mathrm{v}}_d\cdot\underline{\mathrm{n}}_d + \oint_S \rho_b(\underline{\mathrm{v}}_I - \underline{\mathrm{v}}_b)\cdot n_b dS \quad \text{(A.9.46)}$$

where v_I is the velocity at the interface, v_b is the velocity of the bubble, n_b is a unit vector normal to the interface, and $\oint_S$ is the surface integral of the bubble.

Using Gauss theorem for a scalar A.8.2 on the second term in equation (A.9.44), and the continuity equation A.8.4, equation (A.9.46) reduces to:

$$\frac{dm}{dt} = \oint_S \dot{m}_b dS \tag{A.9.47}$$

Insert the following relations $m_b = \rho_g V$ and $V = \pi d_b^3/6\rho_b$ into equation (**??**):

$$\frac{d}{dt}\left(\frac{\pi d_b^3 \rho_g}{6}\right) = -\dot{m}_b A \tag{A.9.48}$$

$$\frac{\pi}{6} 3 d_b^2 \rho_g \frac{d(d_b)}{dt} + \frac{\pi}{6} d_b^3 \frac{d\rho_g}{dt} = -\dot{m}_b A \tag{A.9.49}$$

$$\tag{A.9.50}$$

Divide all the terms by πd_b^2 gives:

$$\frac{\rho_g}{2}\frac{d(d_b)}{dt} = \frac{-\dot{m}_b A}{\pi d_b^2} - \frac{d_b}{6}\frac{d\rho_g}{dt} \tag{A.9.51}$$

$$\frac{d(d_b)}{dt} = \frac{-2\dot{m}_b A}{\pi d_b^2 \rho_g} - \frac{d_b}{3\rho_g}\frac{d\rho_g}{dt} \tag{A.9.52}$$

Insert equation (A.9.14) into equation (A.9.51):

$$\frac{d(d_b)}{dt} = \frac{-2\dot{m}_b \pi d_b^2}{\pi d_b^2 4\rho_g} - \frac{d_b}{3\rho_g}\left(\frac{p_g}{RT}\frac{d\bar{M}_g}{dt} + \frac{\bar{M}_g}{RT}\frac{dp_g}{dt}\right) \tag{A.9.53}$$

$$= \frac{-2\dot{m}_b}{\rho_g} - \frac{d_b}{3\rho_g}\left(\frac{p_g}{RT}\frac{d\bar{M}_g}{dt} + \frac{\bar{M}_g}{RT}\frac{dp_g}{dt}\right) \tag{A.9.54}$$

The total mass flux can be given by equation A.9.45.